

Fundamental Study and Application of Femtosecond Laser Solid Interactions

by

Zhijiang Chen

A thesis submitted in partial fulfillment of the requirements for the degree of

Doctor of Philosophy

in

Photonics and Plasmas

Department of Electrical and Computer Engineering

University of Alberta

© Zhijiang Chen, 2014

Abstract

Femtosecond (fs, $1\text{fs}=10^{-15}\text{s}$) laser pulses are used in a variety of fields from nano-machining to the quest for fusion energy. However, knowledge of quantitative details for femtosecond laser material interaction processes is still insufficient, and many unique applications remain unexplored. The first part of this thesis describes the quantitative study of the fundamental processes in early stages of femtosecond laser excited gold. The second part discusses the investigation of a unique application using femtosecond laser to tune the silicon microring resonators.

In the fundamental investigation, a single state warm dense gold was generated by isochorically heating a free standing gold thin foil of 30nm thickness with a 45fs laser pulse at 400nm. The uniform heating of such a target was confirmed by simultaneous measurement of the reflectivity from its front and rear sides with two frequency chirped probe pulses, at energy density up to $\sim 5\text{MJ/kg}$. The frequency chirped pulse probe single shot technique was developed so that the evolutions of the reflectivities from front and rear surfaces of the heated foil were mapped in frequency domain. Optical pump-probe technique was then used to study the optical properties of gold in the first several picoseconds after laser excitation. The reflectivity (R) and transmissivity (T) of

the excited target were measured simultaneously, and its AC conductivity was calculated from measured R and T. Experimental results were used to benchmark the first principle calculations based Density Functional Theory (DFT) and Quantum Molecular Dynamic (QMD) simulations.

In the application study, the feasibility of using femtosecond laser pulses for tuning frequency in silicon microring resonators (SMR) was investigated. Due to fabrication imperfection, the designed resonant frequencies of SMRs are difficult to achieve accurately (e.g. 1nm variation in height can result in an SMR out of tune). It has been demonstrated that femtosecond laser pulses can tune the resonant frequency of SMRs permanently to either shorter or longer wavelengths, and controllable tuning is also possible.

Preface

This thesis is an original work by Zhijiang Chen. Some of the research in this thesis derives from collaborative works with researchers from University of Alberta, and some with researchers from other universities and institutes. The research works from Chapter 3, 4 and 5 were led by Professor Andrew Ng from University of British Columbia with Professor Ying Tsui being the major collaborator at University of Alberta. The works in Chapter 8 was from the collaboration with Professor Vien Van and his student Daniel Bachman, and my supervisors Professor Robert Fedosejevs and Professor Ying Tsui. The data re-analysis in Chapter 6 was inspired by Professor Andrew Ng and Professor Ying Tsui. The experimental work in Chapter 7 was inspired by Professor Robert Fedosejevs, and the data analysis was inspired by Professor Ying Tsui. The thesis introduction in Chapter 1, the research background in Chapter 2, and the conclusions in Chapter 9 are my original works.

Chapter 3 has been published as: Z. Chen, V. Sametoglu, Y.Y. Tsui, T. Ao, and A. Ng, “Flux-Limited Nonequilibrium Electron Energy Transport in Warm Dense Gold,” *Phys.Rev.Lett.* 108, 165001(2012). I was responsible to design the experimental setup, led the experiment carried out at Advanced Laser Light Source facility, and analyse the experimental data. Dr. Sametoglou assisted with the experiment. Professor Tsui gave advices on the experiment and helped to interpret the data. Dr. Ao gave suggestions on the experiment. Professor Ng suggested the problem, involved in the interpretation of the data and prepared the initial draft of the manuscript. All authors contributed to the discussion and writing of the manuscript.

Chapter 4 and 5 has been published as: Z. Chen, B. Holst, S. E. Kirkwood, V. Sametoglu, M. Reid, Y.Y. Tsui, V. Recoules, and A. Ng, “Evolution of ac Conductivity in Nonequilibrium Warm Dense Gold,” *Phys.Rev.Lett.* 110,

135001 (2013). I was responsible to design the experimental setup, led the experiment carried out at Advanced Laser Light Source facility, and analyse the experimental data. Dr. Holst and Dr. Recoules were the main contributors for the theoretical calculations. Dr. Kirkwood, Dr. Sametoglou, and Dr. Reid assisted with the experiment. Professor Tsui gave advices on the experiment and helped to interpret the data. Professor Ng suggested the problem, coordinated the collaboration to compare experiment data and theoretical calculations, and prepared the initial manuscript. All authors contributed to the discussion and writing of the manuscript.

Chapter 8 has been published as: D. Bachman, Z. Chen, A.M. Prabhu, R. Fedosejevs, Y.Y. Tsui, and Vien Van, “Femtosecond laser tuning of silicon microring resonators,” *Opt.Lett.* 36, 4695-4697 (2011), and D. Bachman, Z. Chen, R. Fedosejevs, Y.Y. Tsui, and V. Van, “Permanent fine tuning of silicon microring devices by femtosecond laser surface amorphization and ablation,” *Opt.Express* 21, 11048-11056 (2013). I was responsible to design the setup of femtosecond laser pulse tuning and carry out experiments using that setup. Bachman was responsible for the measurement and analysis of the microring resonance frequency. He also fabricated the devices used in the second paper. Dr. Prabhu fabricated the device for the first paper. Bachman prepared the initial drafts of the manuscripts of the two papers. All authors contributed to the discussion and writing of the two manuscripts. Professor Fedosejevs, Professor Tsui and Professor Van helped to interpret the data and gave advices on planning the experiments. Professors Fedosejevs and Tsui also suggested the problem as a continuation of a previous Ph.D student’s (Sean Kirkwood) research work.

Acknowledgements

First of all, I would like to express my gratitude and appreciation to my supervisors Professor Robert Fedosejevs and Professor Ying Tsui. It was their patient guidance, inspirations and supports that led me through my Ph.D study. I would also like to thank Professor Andrew Ng from University of British Columbia, who had shared a lot of his invaluable experience and ideas with me and helped me overcome the challenges.

It was my honour to work with my wonderful colleagues from the Laser Plasma Group and the ECE department throughout my Ph.D study. Dr. Yogesh Godwal, Dr. Ilya Utkin, Dr. Henry Tiedje, Dr. Manisha Gupta, Mianzhen Mo, Shyama Banerjee, Atif Ali, Daniel Bachman, Fatema Chowdhury, Shaun Kerr and Raj Masud are some of them who have shared the pleasure and challenges with me.

An important part of my Ph.D research was the experimental campaigns at Advanced Laser Light Source facility. There, I had the pleasure and honour to work with Dr. Sean Kirkwood, Dr. Matt Reid, Dr. Yoann Pertot, Dr. Sylvain Fourmaux and also the great supporting staff. I will remember the nights that we spent in the lab till morning.

I own a special thanks to my wife Liying Ou for her support and patience in the past 6 years during my Ph.D study. She also taught me to balance between life and work. I would also like to thank our lovely baby girl Eleanor. Her smile always relives my stress.

Last but not least, I want to thank my parents, who let me pursue my studies so far away from home.

Table of Contents

1	Introduction	1
1.1	Research Background	1
1.2	Research Objects and Thesis Outline	5
2	Femtosecond Laser Pulse Interaction with Solid	7
2.1	Femtosecond Laser Absorption Mechanisms	8
2.1.1	Collisional absorption	9
2.1.2	Collisionless absorption	14
2.2	Electron-Electron Thermalization	20
2.3	Electron-ion Energy Coupling	22
2.4	Electron Thermal Conductivity	23
2.5	Lattice Disassembly after Femtosecond Laser Excitation	25
2.6	Summary	26
3	Generation of Single State Warm Dense Gold	27
3.1	The Need of Single State Measurement	27
3.2	Formation of Uniformly Heated Target	29
3.3	Verification of Uniform Heating	32
3.3.1	Preparation of Free Standing Gold Thin foil	33
3.3.2	Experimental Setup	37
3.3.3	Single Shot Chirped Pulsed Probe Technique	39
3.4	Experimental Results	48

3.5	Summary	53
4	AC Conductivity Measurement of Warm Dense Gold	55
4.1	Single Shot Chirped Pulse Measurement of Reflectivity and Trans- missivity	56
4.2	Evolution of AC Conductivity in Warm Dense Gold	57
4.3	Data Analysis Based on Drude Model	59
4.4	Interpretation of The upper Limit of Uniform Heating	67
4.4.1	Flux Limited Ballistic Electron Energy Transportation	67
4.5	Summary	70
5	Comparison with First Principles Calculation	71
5.1	Theoretical calculations	71
5.1.1	Calculation of Electron Heat Capacity C_e	73
5.1.2	Calculation of Electron-ion Coupling Factor g_{ei}	76
5.1.3	AC Conductivity Calculation	81
5.2	Comparison between Experimental Result and Simulation Result	83
5.3	Summary	88
6	Interpretations of Warm Dense Gold using Two Temperature Model Calculation	89
6.1	Interpretation of Lattice Disassembly Measurement	90
6.2	Interpretation of Phonon Hardening Measurement	94
6.3	Summary	99
7	Femtosecond Laser Absorption Measurement in Thick Gold Film	101
7.1	Experimental Measurement	102
7.1.1	Laser System	102
7.1.2	Experimental Setup	103
7.1.3	Sample and Spot Size Measurement	104

7.1.4	Experimental Result	108
7.2	Comparison to Calculations with Single State Dielectric Constant	109
7.3	Summary	113
8	Tuning of Silicon Microring Resonators	114
8.1	Silicon Microring Resonators	114
8.2	Changing the Effective Refractive Index of Silicon Microring Resonators by Femtosecond Laser Pulses	118
8.2.1	Tuning a Silicon Microring Resonators with Multiple Laser Shots on a Same Area	119
8.2.2	Controllable Tuning of a Silicon Microring Resonator	121
8.3	Limitations and Future Improvements	123
8.4	Summary	127
9	Impact and Future Work	128
9.1	Impacts of the Thesis Research	128
9.2	Future Research Directions	129
9.2.1	Properties of Warm Dense Matter with Non-thermalized Electrons	130
9.2.2	DC Conductivity of Warm Dense Matter	130
A	Tuning a Silicon Microring Resonators with Multiple Laser Shots on Same Area	151
B	Controllable Tuning of a Silicon Mircoring Resonator	155

List of Tables

6.1	QSS life time of warm dense gold thin foil before disassembly . .	91
6.2	The time that it takes for DWF to reach 1/e of its original value (t^{DWF}), and the corresponding ion temperature (T_i^{DWF}) at that time.	98

List of Figures

2.1	Flow chart of femtosecond laser pulse interaction with solid target.	8
2.2	Diagram of resonance absorption	17
3.1	Mixture of states of bulk material excited by femtosecond laser pulse	28
3.2	Density evolution of isochoric laser heated free standing solid foil after femtosecond laser pulse excitation. $T=0$ denotes the laser arrival time.	30
3.3	Procedure of uniform heating of free standing gold thin foil by ballistic electron transportation	32
3.4	Procedure to prepare free standing gold thin foils	34
3.5	(1)Setup that is used to lift-off the gold thin foil; (2)A sample plate coated with gold thin foil.	34
3.6	An example of foil thickness (29.9nm) measured by AFM	35
3.7	An example of free standing surface quality measured by Zygo white light interferometer	35
3.8	Layout diagram of a sample plate	36
3.9	Schematic diagram of the laser system we used at ALLS. It amplifies a 10nJ laser pulse to 30mJ by the chirped pulse amplification (CPA) technique.	38
3.10	Conceptual layout diagram to verify the uniform excitation of a 30nm gold thin foil excited by 400nm, femtosecond pump pulse.	39

3.11	Layout of a grating compressor.	40
3.12	Transient grating technique.	42
3.13	FROG trace spectrogram of the chirped probe pulse.	43
3.14	FROG trace spectrogram of the pump pulse	44
3.15	Complete setup of front and rear surface reflectivities of femtosecond laser pulse excited gold thin foil	45
3.16	An example of energy density calibration of an excited free standing thin foil.	47
3.17	An example of front and rear reflectivities of the probe pulses imaged on the ICCD cameras.	48
3.18	Pump pulse induced XPM on probe pulse	49
3.19	Fit to the XPM-FDI ripples using the law of fringe frequency.	51
3.20	Lineouts of front and rear reflectivity evolution of probe pulses at different energy densities.	52
3.21	Comparison of the initial change of reflectivity from front and rear surfaces at 540fs after the laser heating.	53
3.22	Comparison of the initial change of reflectivity from front and rear surfaces at 5ps after the laser heating.	54
4.1	Layout diagram of pump probe experiment of warm dense gold.	57
4.2	Example of the chirped pulse probe reflectivity and transmissivity measurement of the excited foils at energy density around 4MJ/kg.	58
4.3	Evolution of AC conductivity of warm dense gold at different excitation energy density	60
4.4	Best fit to ε_i with Drude model	62
4.5	ε_i between 0.64eV and 10000eV obtained from different reports.	63
4.6	ε_i^{IB} by subtracting ε_i with ε_i^{Drude}	64
4.7	ε_r^{IB} as a function of upper limit in the Kramers-Kronig integration.	65
4.8	Time evolved n_e and τ at different excitation energy densities.	66

4.9	Initial values of n_e and τ at different excitation energy density. . .	66
4.10	Maximum energy flux that can be carried by non-thermal ballistic electrons (Q_{NT}) and absorbed laser flux (Q_L) as a function of energy density	69
4.11	The ratio of Q_L over Q_{NT} as a function of absorbed laser flux. The dashed line is for eye guiding	69
5.1	Comparison of electron heat capacity C_e	75
5.2	Maximum electron temperature right after electron thermalization as a function of energy density.	76
5.3	Comparison of electron-ion energy coupling factor g_{ei}	80
5.4	TTM calculated ion temperature at 540fs and 6ps after the peak of pump laser with different g_{ei}	81
5.5	Comparison of calculated σ_r and σ_i with experimental data at room condition.	84
5.6	Comparison between experimental data and simulation of AC conductivity at 540fs after pump pulse.	85
5.7	Measured and calculated time evolved AC conductivity.	86
5.8	Comparison of g_{ei} of aluminium from different calculations . . .	87
6.1	TTM calculation using the new optimum value of C_e of the ion gained energy density $\Delta\varepsilon$ at the time of lattice disassembly. . .	92
6.2	Best fit values of QSS with $\Delta\varepsilon=2.4\pm 0.6\times 10^5$ J/kg to the the experimental data.	93
6.3	Recalculation of time evolved DWF with $g_{ei}=2.2\times 10^{16}$ W/m ³ /K. . .	96
6.4	Recalculation of DWF with $g_{ei}=2.2\times 10^{16}$ W/m ³ /K and $\Theta_D=165$ K. . .	97
6.5	Recalculation of DWF with $g_{ei}=2.2\times 10^{16}$ W/m ³ /K and $\Theta_D=99$ K. . .	98
7.1	Setup of femtosecond laser absorption measurement.	104
7.2	An ablation spot of $14.2\mu m$, measured by Zygo white light profilometer	107

7.3	An example measurement plot to determine the spot size by the Gaussian beam limiting technique for the FL=10cm lens.	107
7.4	Experimental results of the absorption of 800nm, 150fs laser pulses as a function of incident fluence on gold thin film. FL indicates the focal length of the used laser beam focusing optics.	108
7.5	The calculated laser reflectivity as a function of peak energy fluence using dielectric functions measured at single state compares to experimental data. FL indicates the focal length of the used laser beam focusing optics.	112
8.1	An SEM picture of a silicon microring resonator	116
8.2	Experimental setup that is used to tune the SMRs.	119
8.3	Experimental setup that was used to measure the resonant wavelength of the SMRs	120
8.4	Diagram for the calculation of modified section in an SMR . . .	123
8.5	A scheme to tune the resonant wavelength to desire value (λ_a) by amorphization only.	125

Abbreviations and Symbols

List of commonly used abbreviations and Symbols

AC	Alternating current
AFM	Atomic force microscope
DC	Direct current
DFT	Density functional theory
DWF	Debye-Waller factor
FDI	Frequency domain interferometry
FROG	Frequency resolved optical gating
fs	femtosecond (10^{-15} of a second)
FWHM	Full width at half maximum
ILH	Isochoric Laser Heating
ps	picosecond (10^{-12} of a second)
QSS	Quasi-steady state
TTM	Two Temperature Model
SMR	Silicon Microring Resonator
SEM	Scanning electron microscope
UED	Ultrafast electron diffraction
WDM	Warm Dense Matter
XPM	Cross phase modulation

C_e	Electron heat capacity
C_i	Ion heat capacity
e	Unit charge
E_F	Fermi energy
g_{ei}	Electron-ion energy coupling constant
κ	Electron thermal conductivity
k_B	Boltzmann constant
m_e	Electron mass
n_e	Electron density
R	Reflectivity
T	Transmissivity
T_e	Electron temperature
τ	Electron collision time
σ_r	Real part of AC conductivity
σ_i	Imaginary part of AC conductivity
T_i	Ion temperature
T_F	Fermi temperature
Θ_D	Debye temperature
ω_p	Plasma frequency

Chapter 1

Introduction

1.1 Research Background

Femtosecond(fs, 10^{-15} second) laser pulses [1] can be used to perform material processing in an unprecedented manner. They have been widely utilized for a variety of applications, such as nano-scale material modification and processing [2], particle acceleration for medical treatments [3, 4], investigation of conditions in planetary cores in astrophysics [5], and even the quest for artificial solar energy by laser fusion [6]. This is because femtosecond laser pulses can reach the same intensity as longer duration laser pulses at much lower energy, so that less amount of energy is needed to achieve phase transition and modify material. In material processing, the overall volume of modified material is generally related to the deposited laser energy. Less amount of employed energy and smaller heat affected zone [7] from femtosecond laser excitation thus can help to achieve better spatial resolution in the process. However, since the the laser pulse deposits energy to the electron system in a time that is much shorter than the electron-ion energy coupling time, the material will be in a non-equilibrium state, e.g. electron temperature (T_e) is much higher than that of the ions (T_i).

The general processes of femtosecond laser solid interactions are,

(1) The energy of the laser pulse is firstly absorbed by the electrons, because they are far more susceptible to acceleration in the laser's EM field than the heavier ions. The excited electrons may not have a thermalized energy distribution (Fermi-Dirac distribution) shortly after the laser pulse, and the time of electron thermalization may depend on the photon energy[8] and laser intensity [9], mechanisms of laser absorption, and the material properties themselves [10]. Typically, such process takes tens to hundreds of femtoseconds.

(2) The optical properties of the excited materials can be modified within the laser pulse duration, no matter they are thermalized or not. This can in turn, change the rate of laser absorption, and even the dominating mechanisms of laser absorption [11, 12].

(3) The energy from the electron system will take a few to a few tens of picoseconds to couple their energy to the ion system, which mainly depends on the material's electron-phonon coupling properties[13, 14]. Here the coupling time may be defined as the time needed to reduce the difference between T_e and T_i to $1/e$ of their maximum difference.

(4) The solid target can change to different phases, such as liquid, vapor or plasma once sufficient energy is transferred to the ion system, and may lead to material removal from the target.

Due to the non-equilibrium condition, many details in the ultrafast laser matter interaction procedure are not well understood yet. In equilibrium conditions, the materials have their well defined phases, which depends on their temperature and density. In solid target excited by femtosecond laser pulses, on one hand, the electron temperature can be easily above the material's Fermi temperature (T_F), which is comparable to a plasma state. On the other hand, the lattice system is much colder than the electrons, and its density is similar to that of solid before material disassembly. Material in such state cannot be completely described by either plasma physics or solid state physics. This much less studied material condition is usually referred to as warm dense mat-

ter (WDM), which is defined for the states of material with temperature in the same order of its Fermi temperature(T_F), while the density is on the order of its solid phase [15]. The exact boundary for WDM is not clearly defined. Typically, materials with 0.1 to 10 times of its solid density, while the temperature is in the range of 1 to 100eV¹ are of the main interests in warm dense matter study[16]. More specifically, femtosecond laser excited material with high electron temperature (T_e) but much lower ion temperature (T_i) may be referred to as non-equilibrium WDM, or two temperature WDM [17]. To better control the femtosecond laser material processing, it is necessary to understand the pathway from non-equilibrium, to equilibrium in the warm dense matter state. That is, (1) from non-thermalized to thermalized electron temperature distribution, and (2) from two temperature to one temperature ($T_e = T_i$) in the laser excited material.

Characterization of warm dense matter generated by femtosecond laser has been of great interests over the past decades. Milchberg *et. al* [11] measured the reflectivities of a 300fs laser pulse as a function of laser intensity (laser power per unit area) on aluminum film surface and interpreted the results in terms of the corresponding electrical conductivity. However, due to the density gradient and temperature gradient, which were not well characterized, their interpretation of the results was questionable [18]. To minimize or completely eliminate the gradient effect, an isochoric laser heating method to uniformly excite a free standing ultra thin film target was proposed by Forsman *et. al* [19]. Although the original proposed experimental was based on aluminum, the followed up studies are focused on gold instead. This is because gold has no native oxide layer on its surface, which can avoid the mixture of materials, or gradient of materials in the studies, which is especially important for thin films of only tens of nanometers thick.

Based on the proposed method, Widmann *et. al* [20] isochorically excited

¹in plasma physics community, electron volt(eV) is usually used as temperature unit. To convert to Kelvin (K), 1eV=11600K

the 30nm free standing gold thin foil with a 150fs laser pulse at 400nm. Uniform excitation of the thin foil target relies on the assumption that the thermal energy could be distributed across the foil by laser excited ballistic electrons. The time evolved AC conductivity of such two temperature warm dense gold thin foil was extracted from the measurement of reflectivity and transmissivity of an 800nm, 150fs probe pulse. It was observed that the AC conductivity stayed at a quasi-steady state(QSS), where the AC conductivity remains almost constant, for a few picoseconds. Later study by Ao *et. al* [16] measured the disassembly time of such warm dense gold with frequency domain interferometry (FDI) technique. The amount of shift of interference fringes was found to have similar QSS behaviour for similar durations as a function of excitation energy density (absorbed energy per unit mass), until disassembly of the foils occurred. The broadband dielectric function of warm dense gold during quasi-steady state was measured by Ping *et. al* [21], and band structure seemed to exist, which suggested that the foil remained at solid phase during QSS.

Using the measured lifetime of QSS, the lattice temperature at disassembly time can be calculated with two temperature model (TTM), which considers two coupled equations that describe the electron and ion temperatures separately. Based on the parameters from solid state physics in equilibrium state, i.e. $T_e=T_i$, the result from TTM calculations suggested a constant melting point in femtosecond excited warm dense gold, while this melting point would be more than twice of that from equilibrium condition [16, 22]. With the recent development of density functional theory (DFT) calculation, the parameters for TTM calculation, such as electron heat capacity and electron ion coupling factor, can be calculated as a function of T_e . These two calculated parameters were significantly different from those under equilibrium condition [14]. The phase transition condition in recent measurement of ultrafast electron diffraction through femtosecond laser excited warm dense gold was interpreted by Ernstorfer *et. al* [23] with TTM based on DFT calculated parameters. Their

result suggested that not only was super heating found in femtosecond excited gold, but its melting temperature for T_i would also increase with electron temperature (a phenomenon called phonon hardening), or the excitation energy density in other words. The authors indicated that “Strong electronic excitation reduces the screening of the attractive internuclear potential, resulting in a steepening of the phonon dispersion and a hardening of the lattice” [23].

1.2 Research Objects and Thesis Outline

The above-mentioned studies are important milestones in the understanding of the evolution of non-equilibrium warm dense matter. However, the interpretations of those studies were based on certain assumptions. A systematic study is needed to re-visit those studies and examine the validity of the assumptions, which is the general goal of my Ph.D study.

In my thesis research, the first study is to verify the assumption of uniform heating of femtosecond laser excited warm dense gold by laser excited ballistic electron energy transportation. This was done by measuring the front and rear reflectivities of an excited free standing gold thin foil simultaneously as a function of time with two laser probe beams. The results indicated that a 30nm gold thin foil can be uniformly heated at absorption laser fluence up to $6.4 \times 10^{12} \text{W/cm}^2$ with a 45fs laser pulse, or 5MJ/kg in excitation energy density. This is covered in Chapter 3.

In the second study, the time resolved AC conductivity of warm dense gold was re-visited by using a frequency chirped pulse probe beam technique. The new measurement can obtain the evolution of AC conductivity in a single shot, so that the details of the quasi-steady state period masked by previous multiple shot measurement are unveiled. This is reported in Chapter 4.

In the third study, the two important parameters from first principles calculations, electron heat capacity C_e , and electron-ion coupling factor g_{ei} , are

benchmarked with the AC conductivity data. The optimum values of C_e and g_{ei} are found. This is described in Chapter 5.

In the fourth study, the experimental data by Ao *et. al* [16] and Ernstorfer *et. al* [23] are re-visited by two temperature model calculations with optimum values of C_e and g_{ei} . The new interpretation suggests a melting condition of T_i similar to that in equilibrium state instead of super heating for gold. This is reported in Chapter 6.

As a comparison between theoretical study under ideal conditions and application with more complexity, the results of AC conductivity measured from single state (uniformly excited) warm dense gold is used to interpret the data of femtosecond laser reflectivity from a thick gold film surface as a function of incident laser energy fluence (energy per unit area). This is described in Chapter 7.

As a demonstration of the capability of femtosecond laser pulses, a new application to tune silicon micro-ring resonators (SMR) is reported in Chapter 8, and the potential improvements needed for actual application is proposed.

Last but not least, the impact of my Ph.D research is summarized in Chapter 9, and the potential further paths along these studies are also given.

To start with, a more detailed overview of femtosecond laser pulse interaction with solid targets is provided in the next chapter.

Chapter 2

Femtosecond Laser Pulse Interaction with Solid

For femtosecond laser pulse interactions with solid target, the general processes are shown in Fig.2.1. First of all, the laser pulse is absorbed by the electron system, while the electrons thermalize between themselves. Typically it takes tens to hundreds of femtoseconds for the electrons in metal to achieve a Fermi distribution[9, 24, 25, 8]. Shortly after the end of the laser pulse, the absorbed energy stores mostly in the electron system, since it takes a few to a few tens of picoseconds to couple energy to the lattice system[13, 16]. As the lattice temperature increases, the kinetic energy of the ions also increases, and it can be of the same order of magnitude as the potential energy between the ions, so that the ions are strongly coupled. If the excitation energy density is sufficiently high, the displacement of the ions from their equilibrium position can become sufficiently large, so that the vibration of the lattice becomes unstable and lead to lattice disassembly. Melting can lead to lattice disassembly and one empirical rule for melting under equilibrium condition is called the Lindemann's melting criterion [26], which suggests that melting occurs when the root-mean-square(RMS) of atomic vibration amplitude is a fraction of the distance to its nearest neighbour. Such fraction is usually considered to be a constant

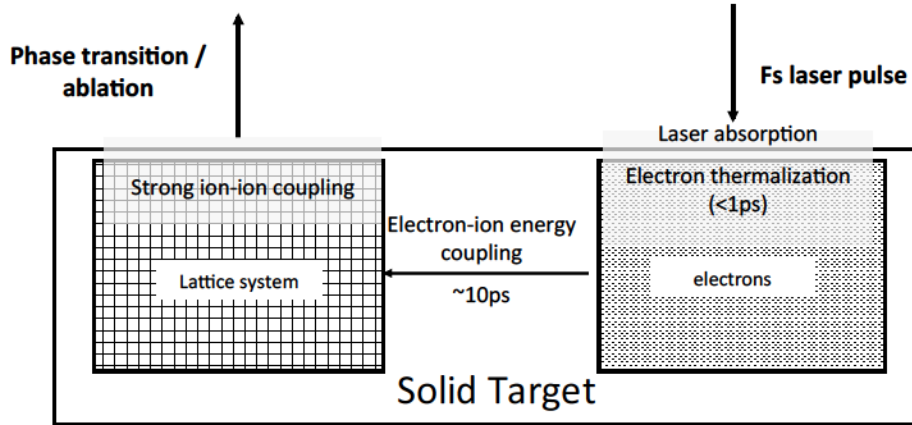


Figure 2.1: Flow chart of femtosecond laser pulse interaction with solid target.

about 0.1, which also depends on the lattice structure [27]. Such criterion is sometimes used in the study of non-equilibrium warm dense matter [28], but direct experimental evidence is still needed to test its validity. Typically, lattice disassembly occurs on the order of a few picosecond, and results in phase transitions, e.g. solid-liquid or solid-vapour and solid-plasma transitions, which will lead to ablation and material removal on the solid surface.

Thus, in the first few picoseconds, the femtosecond laser excited solid is in a non-equilibrium warm dense matter state. This poorly understood state is the main focus of this thesis.

2.1 Femtosecond Laser Absorption Mechanisms

It has been of great interest for researchers to study the absorption of femtosecond laser on solid samples since late 1980s. The knowledge of femtosecond laser absorption can be used to extract much information about the properties of the excited materials. Early measurements by Milchberg *et. al* were used to deduce the DC conductivity of aluminum at high electron temperature (T_e) and low ion temperature (T_i) [11, 18]. The studies by Fedosejeves *et. al* showed how the laser absorption varies with plasma density gradient and incident an-

gle for different laser intensities [29, 30]. Price *et. al* measured the absorption on the surface of metals and dielectrics, which revealed that materials are in a “universal plasma mirror” states when they are irradiated by laser pulses with intensities above $10^{16}\text{W}/\text{cm}^2$ [31]. The study by Ping *et. al* shows that in the relativistic regime, laser prepulse and ion mobility will increase the laser absorption [32]. For the above studies, models from plasma physics were used for interpretation, and hydrodynamic expansion needs to take into account. More recent studies by Fisher *et. al* [33] on aluminum, and Kirkwood *et. al* [12] on copper extended the study to lower laser intensity ($10^{11}\text{W}/\text{cm}^2$). Their data were then interpreted using both models of solid state and plasma state with smooth interpolation in between.

2.1.1 Collisional absorption

In laser pulse interaction with solid targets, it is usual that the electrons play an direct role for absorption, since they are much lighter than the ions and thus more susceptible to the laser field than the lattice system or the ions. The energy absorbed in the electron system usually takes a few picoseconds to transfer to lattice system before the material disassembly starts. As a result, within the pulse duration of a femtosecond laser pulse, the lattice remains cold, and hydrodynamic expansion usually is not significant and sometimes can be ignored. However, the material properties of the target can still change significantly during the laser pulse and thus change the absorption rate. There is also a new challenge that the electron and ion systems are not in thermal equilibrium, or sometimes a well defined thermal distribution does not exist for the electrons during the laser pulse.

There are two major mechanisms for femtosecond laser absorption. One is called collisional absorption, while the second one is collisionless absorption. The absorption of optical laser, or EM wave, by collisional absorption in solid

can be described by its dielectric constant $\varepsilon(\omega)$ ¹, which consists of both real and imaginary parts,

$$\varepsilon(\omega) = \varepsilon_r(\omega) + i\varepsilon_i(\omega) \quad (2.1)$$

The dielectric constant of a certain material varies with the electro-magnetic (EM) field angular frequency (ω). The real part $\varepsilon_r(\omega)$ is a measure of the polarizability of a medium, while the imaginary part relates to the energy loss of such medium. In ideal metal or plasma, where interband transition does not exist, the dielectric constant may be approximated by the classical Drude model. When an EM field (E) with angular frequency ω is applied on a metallic medium, since the ions are much heavier than the electrons, we can simply assume that only electrons can move under the field. The equation of motion for free electrons with average velocity of v_e can be written as,

$$\frac{dv_e}{dt} = -\frac{eE}{m_e} - \frac{v_e}{\tau_c} \quad (2.2)$$

Using the relation $v_e = \frac{dx}{dt}$, where x is the electron displacement. Eq. 2.2 can be re-arranged as,

$$m_e \frac{d^2x}{dt^2} + m_e \nu \frac{dx}{dt} = -eE = -E_0 e^{-i\omega t} \quad (2.3)$$

Where m_e is the electron effective mass, $-e$ is the unit charge of an electron, and $\nu = 1/\tau_c$ is the collision frequency of electrons. The electron displacement x can be solved as,

¹The full dielectric constant depends on both wave frequency ω that oscillates perpendicular to the laser propagation direction, and the the wave number k along the propagation direction. According to the Lindhard's theory of dielectric constant, the dependent of k can be ignored in the long wavelength limit, e.g. $k \ll k_F$, where k_F is the Fermi vector of the material [34]. Such approximation is valid for optical laser propagates in metal, because k is in the order of $10^7/\text{m}$ while k_F is in the order of $10^{10}/\text{m}$.

$$x(t) = \frac{eE}{m_e(\omega^2 + i\nu\omega)} \quad (2.4)$$

This can be related to the polarization per unit volume, or polarization density P , such that,

$$P = -n_e ex = -\frac{n_e e^2 E}{m_e(\omega^2 + i\nu\omega)} \quad (2.5)$$

where n_e is the free electron density in the medium. The dielectric constant in CGS system. thus can be written as,

$$\begin{aligned} \varepsilon(\omega) &= 1 + 4\pi \frac{P}{E} = 1 - \frac{4\pi n_e e^2}{m_0(\omega^2 + i\nu\omega)} = 1 - \frac{\omega_p^2}{(\omega^2 + i\nu\omega)} \\ &= 1 - \frac{\omega_p^2 \tau_c^2}{1 + (\omega\tau_c)^2} + \frac{\omega_p^2 \nu}{\omega(\nu^2 + \omega^2)} i \end{aligned} \quad (2.6)$$

where $\omega_p^2 = \frac{4\pi n_e e^2}{m_e}$ is the plasma frequency. Equation 2.6 is the expression of classical Drude theory for free electrons [35]. The Drude theory implies that the dielectric constant of a medium depends on its free electron density n_e and their collision frequency ν . Free electron density usually increases with the temperature within the pulse duration. In solid state physics for electrons in thermal equilibrium, the probability of electrons at different energy states can be described by Fermi-Dirac distribution [34],

$$F(\epsilon) = \frac{1}{e^{(\epsilon-\mu)/k_B T_e} + 1} \quad (2.7)$$

where ϵ is the energy of a certain state, μ is the chemical potential, and k_B is the Boltzmann constant. According to Eq.2.7, the probability of electrons at higher energy states increases with temperature T , while the conduction band of the solid also lies at higher energy states.

The electrons in solid follow Fermi-Dirac distribution is because of the

Pauli exclusion principle that limits the availability of low energy states[34]. In plasma physics regime, the limitation by Pauli exclusion principle is no longer important, and typically the Maxwell-Boltzmann distribution is used to describe the probability of electron energy[36],

$$F(\epsilon) = \frac{1}{e^{\epsilon/k_B T_e}} \quad (2.8)$$

In plasma physics, the free electron density is proportional to the ionization level when the ion density remains almost constant. In thermal equilibrium, the ionization level can be described by Saha's ionization equation in CGS units [37],

$$\frac{n_{i+1}n_e}{n_i} = \frac{(2\pi m_e k_B T)^{3/2}}{h^3} \frac{2g_{i+1}}{g_i} e^{-U_i/k_B T} \quad (2.9)$$

where n_{i+1} and n_i are the densities of ions of $(i + 1)^{th}$ and i^{th} ionization stages, while g_{i+1} and g_i are the statistical weights of them respectively, n_e and m_e are the density and mass of the electrons, k_B is the Boltzmann constant, T is the temperature, and U_i is the ionization energy for i^{th} ionization stage. The number of electrons increases with equilibrium temperature T . Here we assume that $T = T_e = T_i$, i.e., electrons and ions are in equilibrium. The accuracy of this equation when $T_i \neq T_e$ is still not well studied yet.

In the case of femtosecond laser absorption, however, the electron temperature is much higher than that of the ions, and the electrons may not thermalize between themselves to a well defined temperature distribution, so that the system is not at equilibrium. Equations 2.7 and 2.9 are not sufficient to describe the free electron density in this case. The actual electron density may relate to different laser excitation mechanisms in this transient state. Some of these mechanisms are collisionless, such as multiphoton ionization and tunnelling ionization. There is also collisional ionization, which means that some of the high energy electrons can ionize bound electrons by collisions with them.

The electron collision frequency has a different temperature dependence in solid state and plasma state. In solid state physics, the collision frequency between electrons is proportional to the square of electron temperature T_e according to Landau Fermi liquid theory [38], i.e.,

$$\nu_{ee} = AT_e^2 \quad (2.10)$$

where A is a proportionality constant. Such theory is also used to estimate the electron thermalization time, which will be discussed later in this chapter.

Electron-ion collision frequency in laser excited solid may be described by electron-phonon energy and momentum transfer, whose temperate dependency is [38],

$$\nu_{ei} = BT \quad (2.11)$$

where B is a proportionality constant. This relation is valid in electron-ion equilibrium, i.e. $T = T_e = T_i$, while its validity in non-equilibrium state is yet to be studied.

In the case of plasma, however, the collision frequency decreases as the temperature increases, since electrons with higher velocity can escape from Coulomb collisions easier. For electron-ion collisions, the collision frequency in a Maxwellian plasma in CGS unit is [39],

$$\nu_{ei.pl} = 4(6\pi)^{1/2} Z \frac{n_e e^4}{m_e^2 v_e^3} \ln \Lambda \quad (2.12)$$

where the electron velocity $v_e = \sqrt{\frac{3kT_e}{m_e}}$, Z is the average ionization state of the atoms, and $\ln \Lambda$ is the Coulomb logarithm, which represents the accumulative effect of Coulomb collisions within the effective interaction range. For solid density plasma, one may note that both Z and n_e increase with T_e according to Eq. 2.9, which counteracts the decrease due to v_e , so the significant reduction

of collision frequency does not occur until a high level of ionization is achieved.

The contribution of electron-electrons collision to electrical conductivity in some plasma regimes is still not well understood. It is usually considered that the collisions between electrons do not change the total momentum of electron current. However, for a laser AC field, i.e. a laser pulse which has an EM field of optical frequency, when the e-e collision frequency is comparable to that of the field, the electron distribution can be changed within a cycle of the field. Especially when the electrons are in the course of thermalization, such effect needs to be taken into account [40]. Usually ν_{ee} is not calculated independently in plasma physics. Instead, it may be combined into the effective collision frequency ν_{eff} which also includes the collision between electrons and ions [41, 40, 42]. In the case of Aluminum, ν_{eff} is found to increase with T_e when T_e is below T_F , but decrease as T_e continues to increase according to detailed kinetic simulation studies [41].

2.1.2 Collisionless absorption

When the target material is excited to a plasma-like regime with high ionization state, electron collision rate decreases as T_e or laser intensity increases. The local absorption of EM field energy of material ($Q(z)$) at certain location z under that target surface can be related to its dielectric constant,

$$Q(z) = \frac{1}{2}\omega \frac{\text{Im}(\varepsilon(z, \omega))}{4\pi} |E(z, \omega)|^2 \quad (2.13)$$

According to Eq.2.6, when the collision frequency is significantly lower than the laser frequency, i.e., $\nu^2 \ll \omega^2$, the Imaginary part of ε is,

$$\text{Im}(\varepsilon) \approx \frac{\omega_p^2 \nu}{\omega^3} \quad (2.14)$$

Obviously, the collisional absorption becomes ineffective when ν continues to decrease. For plasmas near solid density, the absorption may start to de-

crease from its maximum value before $\nu^2 \ll \omega^2$, since the plasma frequency increases with electron density at higher T_e which leads to a reduction of depth that the laser light can be absorbed by the collisional process. This has been demonstrated in Price *et. al*'s measurements [31], where a “plasma mirror” is formed, as an analogue to a metallic mirror which reflects most of the laser light. In order to transfer energy from laser to these high density plasmas above such intensity, e.g. $\sim 10^{15} \text{W/cm}^2$, other mechanisms have to come into play.

Among the collisionless mechanisms, the resonance absorption is the best known and investigated one [43, 44, 30, 45]. To initiate the resonance absorption, the propagation direction of the incident laser has to be away from target normal, and the electric field of the pulse has to be parallel to the plane of incident. In this case, the laser pulse is called P-polarized (*P-pol*) to the target, or sometimes referred as transverse-magnetic (TM). In the case of *P-pol*, the electric field of the laser penetrates into the plasma with a steep rising density gradient, by which its energy can transfer into to the plasma by driving electron plasma waves near the critical surface, where the electron plasma frequency ω_p equals to that of the laser frequency ω . For S-polarization (*S-pol*), where the electric field is normal to the plane of incident, or for normal incident laser light, there is no E-field component that oscillates in the direction of plasma gradient.

To understand the resonance absorption, we can revisit the dielectric constant ε in Eq.2.6. A simple case for the collisionless limit is that according to Eq.2.14, the imaginary part of ε becomes small, in which case, the real part of ε can also be simplified to,

$$\text{Re}(\varepsilon) = n^2 \approx 1 - \frac{\omega_p^2}{\omega^2} \quad (2.15)$$

using the relation that $\omega^2 \tau_c^2 = \frac{\omega^2}{\nu^2} \gg 1$, where n is the refractive index of the

plasma. When the laser pulse propagates in a plasma with increasing electron density along z axis as shown in Fig.2.2, its direction of propagation will be diffracted due to the refractive index gradient. As it approaches the critical density n_c layer, the refractive index becomes 0, and the propagation vector becomes perpendicular to the direction of density gradient. i.e. in y direction only, and the electric field has component in z direction only. According to Maxwell's equations, the EM wave in plasma can be written as [36],

$$\nabla \times \mathbf{E} = \frac{i\omega\mathbf{B}}{c} \quad (2.16)$$

$$\nabla \times \mathbf{B} = \frac{-i\omega\varepsilon\mathbf{E}}{c} \quad (2.17)$$

where c is the speed of light in vacuum, one may expect that the electric field will have a singularity, i.e. approaches infinity, at the critical surface according to Eq.2.15, such as,

$$\mathbf{E} = \frac{-c}{i\omega\varepsilon} \nabla \times \mathbf{B} = \frac{-c}{i\omega(1 - \frac{\omega_p^2}{\omega^2})} \nabla \times \mathbf{B} \quad (2.18)$$

In reality, such singularity will disappear due to the plasma wave damping, i.e. the imaginary part of ε is not actually zero. The energy from the EM field of the laser pulse can transfer to the plasma wave due to such damping. Due to the collisionless approximation, fast electrons with kinetic energy much higher than the thermal energy of the plasma will be generated near the critical surface, but eventually, they will be thermalized by coulomb collisions with other ions and electrons. The ratio of laser absorption due to such mechanism can be over 50%, which depends on the laser wavelength, electron density gradient and the laser incident angle [29, 30, 45].

If the electric field intensity in resonance absorption becomes strong enough, electrons near the critical surface, instead of resonating with the laser field, can

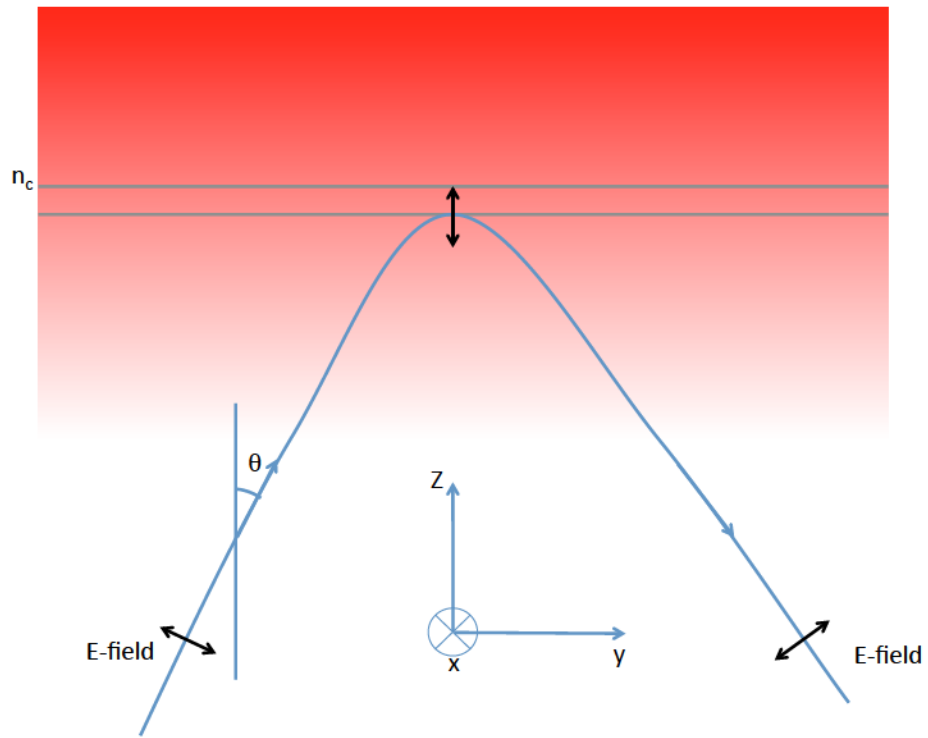


Figure 2.2: Diagram of resonance absorption

be dragged out of the plasma-vacuum surface and then pulled back into the plasma within a single cycle of the field. Such a process is generally referred as vacuum heating [46]. In a further step, if the electrons that are pulled back into the plasma do not collide with other electron or ions within the skin depth but travels deeper into the plasma, e.g. beyond the critical density layer, then such mechanism can transfer the energy beyond the laser penetration depth immediately. Such non-local energy transportation is sometimes called the anomalous skin effect [47].

There is another type of collisionless absorption in solid state physics regime, which is the interband absorption. In this case, the photon energy is larger than that of the bandgap between free electrons and bound electrons. Take gold, a typical noble metal, for example, there is only one conduction electron in the $6s$ band, while the $5d$ band is fully filled. The energy difference between the unfilled $6s$ band and the top of $5d$ bands for gold is about 2.4eV [48]. A photon of 2.5eV has a much larger probability to be absorbed than one with 2.3eV, since the former one can excite an electron from the top of the $5d$ band to $6s$ band. One may include the interband absorption in the equation of motion of electrons, then Eq. 2.3 can be revised as,

$$m_e \frac{d^2x}{dt^2} + m_e \nu \frac{dx}{dt} + m_e \omega_0^2 x = -eE = -eE_0 e^{-i\omega t} \quad (2.19)$$

where ω_0 the radial frequency of the bandgap energy. The dielectric function from Drude theory can also transform to the Lorentz-Drude model [34],

$$\varepsilon_r = 1 + \omega_p^2 \frac{\omega_0^2 - \omega^2}{(\omega_0^2 - \omega^2)^2 + (\omega\nu)^2} \quad (2.20)$$

$$\varepsilon_i = \omega_p^2 \frac{\omega\nu}{(\omega_0^2 - \omega^2)^2 + (\omega\nu)^2} \quad (2.21)$$

If a photon's energy is below the bandgap energy of the target material, interband absorption may still be possible by multiphoton absorption (MPA).

MPA is a non-linear process, whose probability increases with the square of the intensity of the laser pulse. This is because MPA requires the photons be absorbed by a single atom before it decays from the transient state back to the original state or another transient state, which can happen in picosecond or femtosecond time scale, depending on the material and its states.

Besides MPA, there is another type of intensity dependent absorption mechanism called tunnel ionization (TI). In a simple case, assuming that for an atom of $Z=1$ (Hydrogen), an electron has an orbit of r from the atomic core, its potential energy $P = -e^2/r$. The condition for ionization is that r approaches infinity, but the corresponding P will increase as well, and the kinetic energy of the electron cannot support itself to be ionized. However, when an laser pulse with electric field E is applied, the potential field can be suppressed by $-eEr$, so the total potential field becomes $P_{total} = -e^2/r - eEr$. It can be seen that if the absolute value of P_{total} is smaller than the kinetic energy of the electron, then the electron can tunnel through the potential barrier and become ionized. However, it requires that $\gamma \ll 1$, where γ is the Keldysh parameter [49],

$$\gamma = \frac{\omega\sqrt{2m_eP_0}}{eE} \quad (2.22)$$

where P_0 is the ionization potential. This is because the laser field is an AC field, and the Keldysh parameter is the ratio of electron tunnelling time to half a period of the laser field. The electron has to finish the tunnelling process before the laser field flips over for TI. On the other hand, if $\gamma \gg 1$, MPA is expected to dominate.

In femtosecond laser interaction with solids, if the target is a non-metal material, where free electrons are scarce, it requires MPA or TI, or interband absorption process to create such electrons at the beginning of the pulse. Then collision absorption or resonance absorption will dominate thereafter when n_e is sufficiently large.

At even higher laser intensity e.g. $> 10^{18}W/cm^2$, the radiation pressure

from the laser becomes significant and can be larger than the plasma pressure. Such pressure can couple to the electrons, which is usually called pondermotive force [36]. One of the absorption mechanisms related to pondermotive force is called $J \times B$ heating. In such case, the electrons that oscillate with the electric field E will be distorted by the magnetic field of the laser by Lorentz force, and electrons will be driven in the direction of laser propagation. Such a mechanism becomes dominating as the laser intensity increases, since resonance absorption and related mechanisms will be saturated due to the distortion of electron orbits along the E field [50].

When the light pressure, in the form of pondermotive force, becomes larger than the plasma pressure, e.g. laser intensity of 10^{20}W/cm^2 or larger, the plasma will be pushed inward. A radial pondermotive force will also be formed by the electric field in longitudinal direction due to the density gradient direction with the magnetic field. Such force will push electrons out from the center of the laser, and the ions will be pulled out due to charge separation. As a result, density gradient is formed parallel to the electric field, which can support resonant-like absorption even when the laser pulse is normal to the target. This is referred to as hole-boring [51]. Such mechanisms at ultra high intensity can result in an absorption ratio approaching unity [32].

In my thesis studies, for most case, a solid gold target is irradiated by a femtosecond laser pulse at 400nm (3.1eV) with an intensity no more than the order of 10^{13}W/cm^2 , the dominant absorption mechanism is expected to be interband absorption, because the energy difference between $5d$ and unfilled $6s/p$ bands in gold is 2.4eV, which is 0.7eV less than the photon energy.

2.2 Electron-Electron Thermalization

The studies of thermalization between electrons when excited by femtosecond laser pulses have mainly been limited to investigations at low excitation laser

intensity or energy density, where no target damage was observed. There were several investigations in the 1990s on electron thermalization in gold in low excitation energy density regime [9, 24, 25, 8].

In the study by Fann *et. al*, photoemission spectroscopy technique was employed to measure the electron distribution function [9, 24], while in the study by Sun *et. al*, the measurement was based on transient reflectivity and transmissivity from a femtosecond probe pulse. Both of their measurements indicate that the thermalization time decreases as the energy difference (ΔE) between the excited electrons and Fermi energy(E_F) increases. A general relation between thermalization time and ΔE follows the Fermi-liquid theory under random phase approximation [52],

$$\tau_{th} = \tau_0 \left(\frac{E_F}{\Delta E} \right)^2 \quad (2.23)$$

where τ_0 is the proportionality constant of the target material. This value was determined to be about 2fs in gold from Fann *et. al*'s measurement. The above equation has a similar form as Eq.2.10 sinice they come from the same theory. In my thesis studies of gold, $E_F=5.5\text{eV}$, and ΔE is no more than 0.7eV when excited by 3.1eV photons. τ_{th} is thus expected to be no less than 120fs. It should be noted that this equation is only valid when T_e is around 0K. In high power femtosecond laser excitation, the final T_e can be easily above E_F , and the solution of time dependent Boltzmann equation is required for accurate determination of relaxation times [8, 10].

When the electrons are thermalized, i.e. an electron temperature distribution is established, one may use the well known two temperature model (TTM) to describe the femtosecond laser excited solid [13, 53]. The TTM consists of two coupled equations,

$$C_e \frac{\partial T_e}{\partial t} = \frac{\partial}{\partial z} \kappa(T_e) \frac{\partial T_e}{\partial z} - g_{ei}(T_e - T_i) + Q(z, t) \quad (2.24)$$

$$C_i \frac{\partial T_i}{\partial t} = g_{ei}(T_e - T_i) \quad (2.25)$$

where T_e and T_i represents the temperatures for the electrons and ions respectively; z is the distance from the target surface, t is time related to the peak of the laser pulse; C_e and C_i are the volumetric heat capacities for electrons and ions respectively; τ_p is the FWHM duration of the laser pulse; κ is the electron thermal conductivity; g_{ei} is the electron-ion coupling factor, and Q is the absorbed laser power per unit volume.

The heat capacity C_e is directly related to C_e . In solid state physics, it can be obtained from the free electron gas(FEG) model [34],

$$C_e(T_e) = \frac{\pi^2}{2} \left(\frac{k_B T_e}{\epsilon_F} \right) n_e k_B \quad (2.26)$$

where k_B is the Boltzmann constant. We can see that C_e is proportional to the electron temperature T_e and free electron density n_e . However, the FEG based on the Sommerfeld expansion is only an approximation assuming T_e is significantly less than E_F . At higher T_e , one needs to know the internal energy of the electron system as a function of T_e . This can be obtained from density functional theory calculations (DFT). The details will be discussed in Chapter 5.

2.3 Electron-ion Energy Coupling

As can be seen from the TTM equations (Eq.2.24 and 2.25), the electron ion energy coupling is the link between electron and ion systems. The coupling rate is determined by the coupling factor g_{ei} . Similar to electron-electron thermalization, experimental studies of electron-ion energy coupling factor have mainly been focused on the low energy density regime [9, 13].

Take gold for example. In Fann *et. al's* measurement, the coupling factor

g_{ei} was determined from the photoemission spectroscopy measurement, when T_e is below 1000K. The value was determined to be in the range of 2.5 to $6 \times 10^{16} \text{W}/\text{m}^3 \text{K}$. The large uncertainty was likely due to the small amount of change in T_e compared with its room condition (300K). Later study by Holthfeld *et. al* used different techniques including transient reflectivity and transmissivity, damage threshold, and surface expansion measurements. The range of g_{ei} was determined to be $2.2 \pm 0.3 \times 10^{16} \text{W}/\text{m}^3 \text{K}$. In that study, the maximum value T_e was in the range between around 1000K and 10000K.

In the case of higher T_e , no experimental result is available, but first principles calculations have been carried out to determine the electron temperature dependent g_{ei} [14]. The method of calculation and the benchmark tests of such calculation will be discussed in detail in Chapter 5.

2.4 Electron Thermal Conductivity

The skin depth, through which the laser intensity decreases to 1/e of its value on the surface, is typically $\sim 10 \text{nm}$ for most metals [54]. A temperature gradient thus exists after femtosecond laser excitation in the target, although ballistic electrons in solid state physics regime [13], or free streaming fast electrons in plasma physics regime [55] may transfer energy beyond the skin depth thickness. Electron energy diffusion occurs along the temperature gradients, which is described by the electron thermal conductivity κ , which can be found in Eq. 2.24.

In the solid state physics regime, κ is related to electron heat capacity C_e according to the kinetic model of gases [34],

$$\kappa = \frac{C_e v_F l_{mfp}}{3} = \frac{C_e v_F^2}{3 \nu_{eff}} \quad (2.27)$$

where $l_{mfp} = v_F / \nu_{eff}$ is the electron mean free path for conduction electrons travelling at Fermi velocity $v_F = \sqrt{2\epsilon_F / m_e}$, while ν_{eff} is the effective electron

collision frequency.

In high density plasma, one can adopt the conductivity model by Lee and More [56] with electron density dependent [40],

$$\kappa_p = \frac{128(0.24 + Z)n_e k_B^2 T_e}{3\pi(4.2 + Z)m_e \nu_{ei}} \quad (2.28)$$

In the non-equilibrium warm dense matter regime, a possible treatment of κ is to take the interpolation between solid state and plasma regime due to the non-availability of a reliable model at the moment. A method for interpolation was proposed by Anisimov *et.al* [57], and the examples for silver and aluminum can be found in Schmidt *et.al*'s work [58]. Recent interest in the study of electrical conductivity in warm dense matter [11, 20, 59] may in turn shed light on the thermal conductivity of material in this regime, according to the Wiedemann-Franz law [34],

$$\frac{\kappa}{\sigma} = LT \quad (2.29)$$

where σ is the electrical conductivity, and L is the proportionality constant. In solid state physics, it is known as Lorentz number, which equals to $2.44 \times 10^{-8} W \cdot \Omega / K^2$. In the warm dense matter regime, the density functional theory calculation suggests a similar value of Lorentz number [60] for solid density warm dense aluminium for a single temperature, i.e. $T_e = T_i$, in the range of 0.1 to 1eV. The widely used Lee and More conductivity model [56] suggests a lower value of the Lorentz number ($1.18 \times 10^{-8} W \cdot \Omega / K^2$), for solid density warm dense aluminium at a higher single temperature of greater than 10eV.

2.5 Lattice Disassembly after Femtosecond Laser Excitation

In equilibrium condition, lattice disassembly in a solid is generally the result of severe lattice vibration so that the phonons become disordered at high ion temperature [34]. This is usually referred to as thermal melting. In Femtosecond laser excited material, non-thermal melting becomes possible in certain materials. For example, it has been observed in semi-conductors such as silicon [61] and germanium [62], when a sufficient number of valence electrons are excited to the conduction band after the absorption of a femtosecond laser pulse, the lattice bonding softens and disassembly occurs without the need of an increase in ion temperature. In insulators, due to the lack of free carriers to shield the strong local charge after irradiation by intense laser pulse, Coulomb explosion becomes possible [63].

In the case of metal, on the other hand, the melting point may increase under non-equilibrium conditions. First principles calculations by Recoules *et. al* [64] found that the frequency of the phonon spectrum may increase significantly in gold when T_e is in the order of a few electron-volts. This may lead to the increase in the Debye temperature and thus the melting point of gold.

Experimentally, researchers have claimed the observation of increased melting point in femtosecond excited gold [16, 23] according to their TTM calculations. Especially, in Ernstorfer *et. al's* study, they found that the melting point increases as a function of T_e [23], which agrees with Recoules *et. al's* calculation [64]. Details of their work and re-interpretation of their results will be presented in Chapter 6.

2.6 Summary

The general processes of femtosecond laser solid interaction is reviewed in this chapter, from laser absorption to lattice disassembly. It is obvious that many details of the electron and ion/lattice behaviours are still not clearly known. It is mainly because of the thermal non-equilibrium condition in solid target shortly after femtosecond laser pulse excitation. My Ph.D research was focused on the study of femtosecond laser pulse excited gold, in order to give better understanding in these details, especially for electron-ion energy coupling and lattice disassembly conditions.

Chapter 3

Generation of Single State Warm Dense Gold

To understand the material in warm dense matter state more precisely, the measurement needs to be carried out in a single state with minimum temperature and density gradient. It may be done by isochoric heating technique [19] to excite a free standing thin foil target with a femtosecond laser pulse. The experiments were carried out at the Advanced Laser Light Sources (ALLS) facility in Canada. As a first step, one needs to verify that the thin foil target can be excited uniformly. A chirped pulse single shot probe technique was developed to measure the reflectivity from the front and rear surfaces of the foil simultaneously for this purpose.

3.1 The Need of Single State Measurement

Warm dense matter state is an important state which links the condensed matter state and plasma state. WDM created in a laboratory usually consists of different states with density and temperature gradients. For example, when material is excited by a femtosecond laser pulse with sufficient energy, within a few to few times of picosecond, the surface layer becomes a hot plasma and

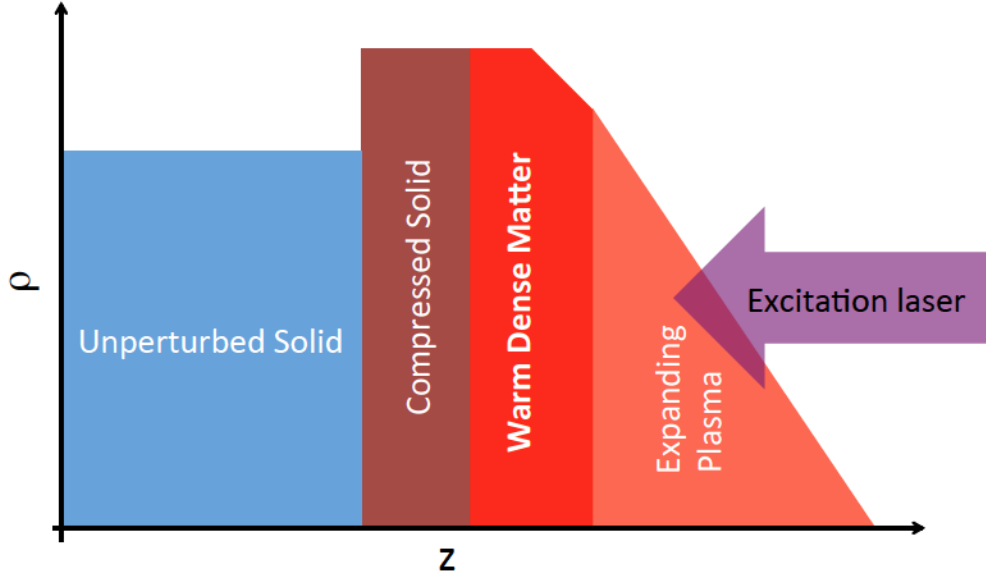


Figure 3.1: Mixture of states of bulk material excited by femtosecond laser pulse

starts to expand. Such expansion compresses the material inward and may result in warm dense matter and compressed solid layers. This mixture of states of material is shown in Fig.3.1.

The interpretation of the data measured from such convoluted states is complicated, since it needs to consider temperature and density gradients as well as energy transport as discussed in Chapter 2, and hydrodynamic expansion may also need to be taken into consideration. For example, the measurement of femtosecond laser absorption in aluminum was used to extract the DC conductivity in WDM state by Milchberg *et. al* [11]. Their original interpretation, which was based on a constant density gradient, has substantial difference from the DC conductivity model developed by Lee and More [56], which was found to corroborate with the shocked compressed aluminum data measured by Ng *et. al* [65]. However, when time dependent electron density gradient is taken into consideration, their data was found to have reasonable agreement with Lee and More's kinetic theory model as well as the density functional theories model by Perrot *et. al* [66].

To avoid such complexity and in order to benchmark theories more accu-

rately, an idealized slab plasma (ISP) concept was proposed by Forsman *et al* [19] to generate single state WDM with minimum temperature and density gradient. The original proposal was to excite free standing ultrathin aluminum foil with ultrafast femtosecond laser pulses, with a technique called isochoric laser heating (ILH). The basic idea of this technique is to deliver energy to the target in a femtosecond time scale, and thus the hydrodynamic expansion can be minimized to achieve an almost isochoric conditions. At the same time, the target is thin enough that the energy can be distributed uniformly throughout its thickness. In reality, due to the significance of aluminum oxide layers, the idea was realized with free standing gold thin foils instead [20, 16, 21].

In isochoric laser heating, it is expected that a well defined electron temperature can be reached in less than a picosecond. The laser heated free standing solid foils are expected to have a density close to solid for a few picoseconds before lattice disassembly[16]. During this time, the lattice constant of the heated solid may increase slightly due to the increase of T_e and T_i [67]. Eventually, when the lattice disassembly condition is reached, which typically takes a few to a few tens of picoseconds, a hydrodynamic expansion of the foil occurs[68]. An illustration of the mass density evolution is shown in Fig.3.2. My Ph.D research was focused on the investigation of isochoric laser heated gold thin foil within in a time window after the thermalization of the electrons, and before the lattice disassembly.

3.2 Formation of Uniformly Heated Target

In order to generate single state excited WDM, it needs the energy to be deposited uniformly in the target before significant expansion occurs. In terms of energy deposition depth, optical laser pulses are actually inferior when compared with other sources such as X-ray, electrons or ions. The typical skin depth, through which the laser field intensity decreases to $1/e$ of its original

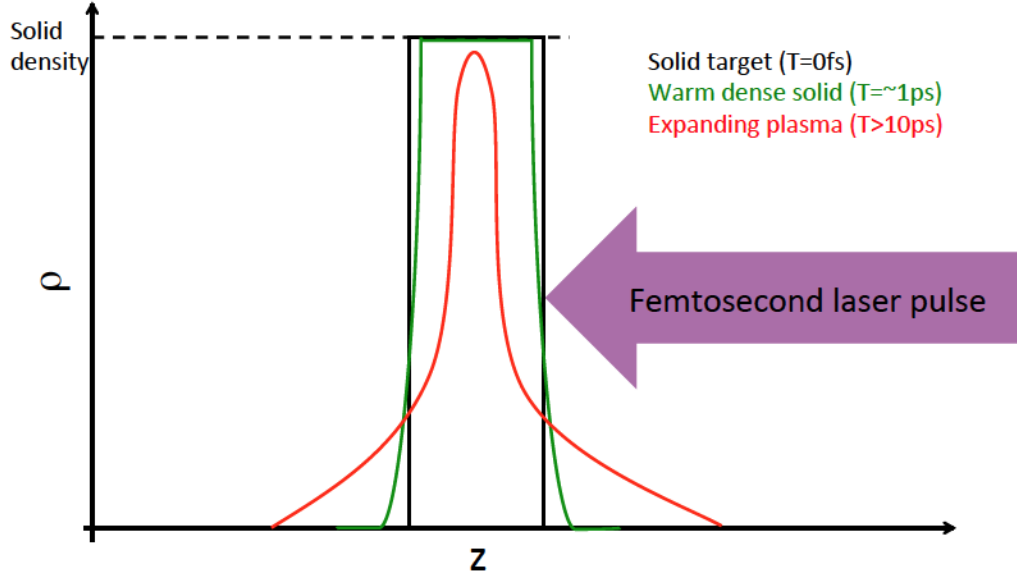


Figure 3.2: Density evolution of isochoric laser heated free standing solid foil after femtosecond laser pulse excitation. $T=0$ denotes the laser arrival time.

value, for optical laser pulses in metal is only on the order of 10~20nm [69], while hard X-ray can penetrate hundreds of nanometer to many micrometers depending on the atomic number of material [70], fast electrons and ions of MeV order energy can penetrate millimetres or even further [71]. However, unlike lasers, the availability of the other sources of femtosecond pulse width are limited at the moment. On the other hand, although a very thin free standing foil may be uniformly heated, it may not be suitable for warm dense matter study. For example, gold thin films of less than 20-30nm would have optical properties that are much different from that of bulk [48].

Previous studies that measured the transient reflectivity of gold thin foils after femtosecond excitations below damage threshold shows that the femtosecond pulses can excite ballistic electrons in a gold thin films [72, 73, 74, 75, 13]. These ballistic electrons travel in the conduction band at near Fermi velocity (v_F) and can transport the laser energy throughout the thin foil rapidly. The theoretical value v_F for gold is 1.4×10^6 m/s, according to the Fermi energy of gold (5.5eV). The range of ballistic electron transportations in gold are found

to be $\sim 100\text{nm}$ from experiments of transient reflectivity of thin foils after laser excitation [74, 75, 13].

In previous studies of isochoric heating of warm dense gold [20, 16, 21], 30nm free standing gold thin foils were used as targets, whose thickness is less than 1/3 of the reported ballistic electron range. It is thus expected that the 30nm gold thin foil can be uniformly excited by ballistic electrons. The gold thin foils are excited by femtosecond laser pulses at 400nm, which are from the frequency doubled output of Ti:Sapphire laser system. The process of ballistic electron transportation in gold is illustrated in Fig. 3.3. (1) The 400nm(3.1eV) photons are absorbed mainly by the 5*d* electrons of gold, which are about 2.4eV below the unfilled states in 6*s* band[48], in the skin depth region. (2) These electrons are excited upto 0.7eV above the Fermi energy (E_F) and transport ballistically near v_F ¹ around the foil until they are thermalized. The life time, or thermalization time for electrons at ΔE above E_F is $\tau_{th} = \tau_0(\frac{E_F}{\Delta E})^2$ according to Fermi liquid theory [34, 73, 9]. For $\Delta E = 0.7\text{eV}$, τ_{th} is about 120fs using $\tau_0=2\text{fs}$ according to Fann *et. al*'s photoemission spectroscopy measurements on gold at low energy density below damage threshold [9, 24], (3) Assuming that the ballistic range (l_{ba}) is 100nm as reported by previous studies [74, 75, 13], electrons with l_{ba} longer than the foil thickness will make multiple transits in the foil [77] instead of escaping, because the work function of gold is 5.1eV. It takes about 100fs to finish such process, and the laser energy absorbed within the skin depth is expected to distribute uniformly within a 30nm gold thin film. The work function of our gold foils may be modified by surface hydrocarbon layers formed during the exposure to air and water in the fabrication process[78]. However, if a significant amount of electrons overcome the work function and escape from the foil, a space charge electric field will be

¹The ballistic electrons excited from 5*d* orbitals after absorption of 3.1eV photon should have an energy between Fermi energy (5.5eV) of gold and 0.7eV above it (6.2eV), which corresponds to 1 to 1.06 times of the Fermi velocity in gold ($1.4 \times 10^6\text{m/s}$). In experimental measurements, the ballistic electrons travels at around $1 \times 10^6\text{m/s}$ [74, 76, 13, 73]. The actual velocity of the ballistic electrons may be affective by the direction of the Fermi surface[77].

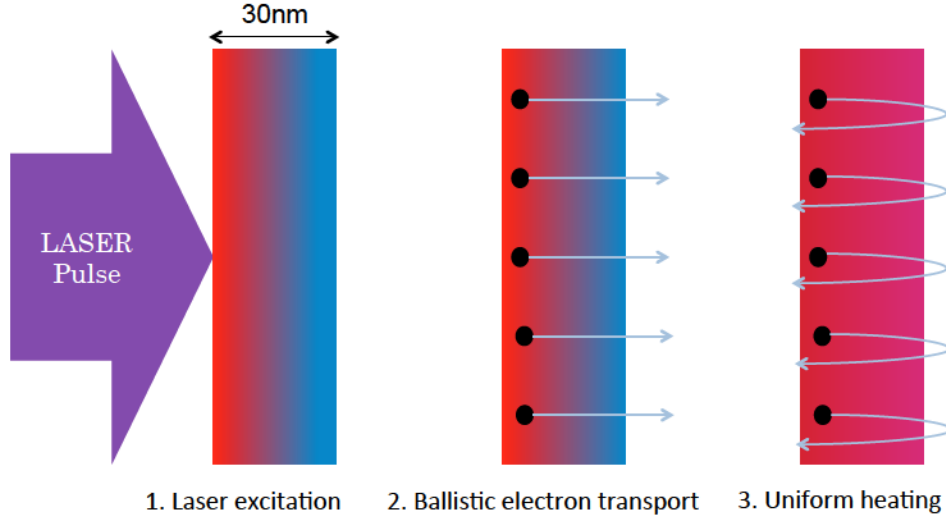


Figure 3.3: Procedure of uniform heating of free standing gold thin foil by ballistic electron transportation

generated to limit more electrons from escaping. It was reported that only a very small number of electrons can escape from a silver surface at excitation laser intensity up to $10^{14}\text{W}/\text{cm}^2$ [79].

3.3 Verification of Uniform Heating

Earlier studies that measured the AC conductivity and disassembly time of warm dense gold [20, 16, 21] are based on such an assumption of uniform excitation by ballistic electrons. However, in those studies, as the excitation energy densities increases, the measurements with probe pulses at different polarization start to give significantly difference results in the interpretations of AC conductivities based on a single state assumption [22]. The uniform excitation condition becomes questionable at such energy densities. It is thus necessary to examine if the foil is uniformly excited before further investigations.

3.3.1 Preparation of Free Standing Gold Thin foil

The technique to fabricate free standing gold thin foils of 30nm thickness follows the suggestions of C.M. Cadwalader from Lawrence Livermore National Laboratory (LLNL), who has prepared targets for the earlier isochoric laser heating experiments [20, 16, 21]. The procedure is described as follows, with a diagram shown in Fig.3.4.

(1) Coat a very thin layer of soap (LiquiNox concentrated soap) on a piece of microscope slide of 2 inch \times 3 inch in size by putting a droplet on the slide, and even out the soap by wiping it many times gently with a piece of kimwipe, until it looks as smooth as the original slide. Then sputter 30nm of gold thin film on the soap layer using the magnetron sputtering system at the NanoFab at University of Alberta with its standard deposition procedure.

(2) Mount the slide coated with soap and gold on a dedicated manipulator consisting of two motion stages (see Fig.3.5(1)), and gradually submerge the slide into fresh distilled water while the soap dissolves and the gold film comes off. The gold film will float on the water surface due to surface tension.

(3) When a whole piece of gold film floats off, use a wafer tweezers to hold a sample plate, and put it underneath the gold film with $\sim 45^\circ$ angle. Once the plate contacts the film, withdraw the plate while keeping the $\sim 45^\circ$ angle. The film will be coated on the plate. Use Q-tips to clear any foil that wraps to the back side of the plate, then place the plate face up on a piece of kimwipe until it is dry. A coated sample plate is shown in Fig.3.5(2).

The thickness of the thin foil is measured by an atomic force microscope (AFM, Veeco D3100). The film for the thickness measurement was prepared as the aforementioned procedure, except in step (3), it was taken out from the water with an microscope slides instead of the sample plate. The measurements were taken on the steps from the edge of the film to the slide surface. An example is shown in Fig. 3.6. The film thickness for our experiments were 29.4 ± 1.5 nm. The surface quality of the free standing foils mounted on a sample

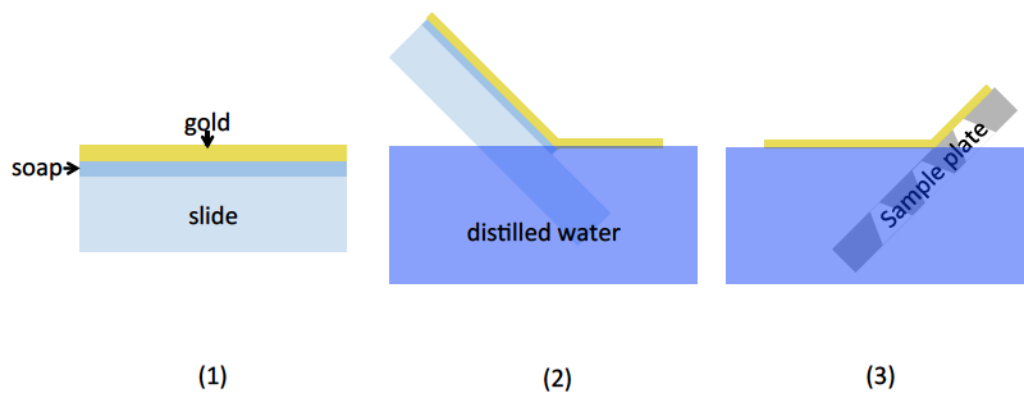


Figure 3.4: Procedure to prepare free standing gold thin foils

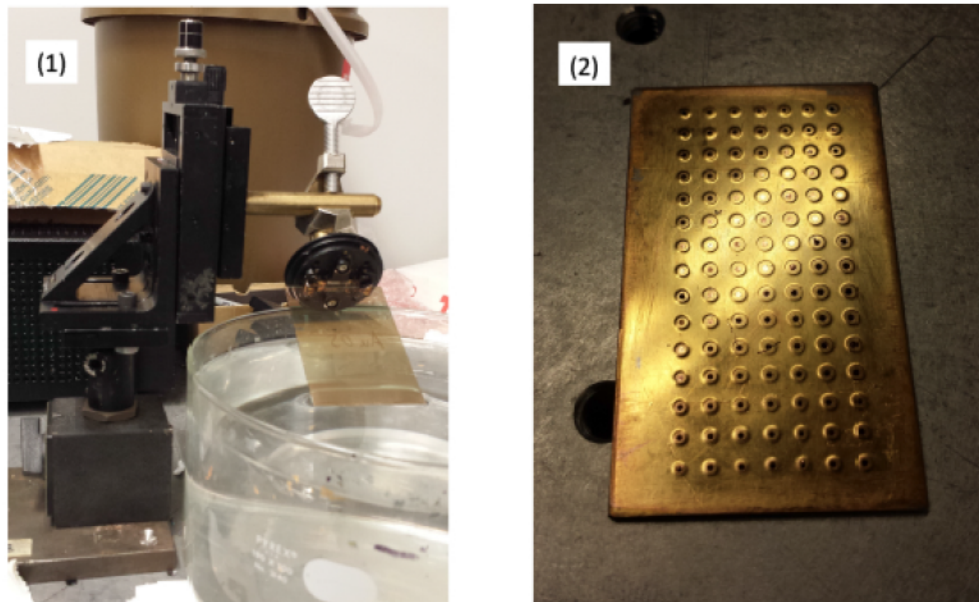


Figure 3.5: (1) Setup that is used to lift-off the gold thin foil; (2) A sample plate coated with gold thin foil.

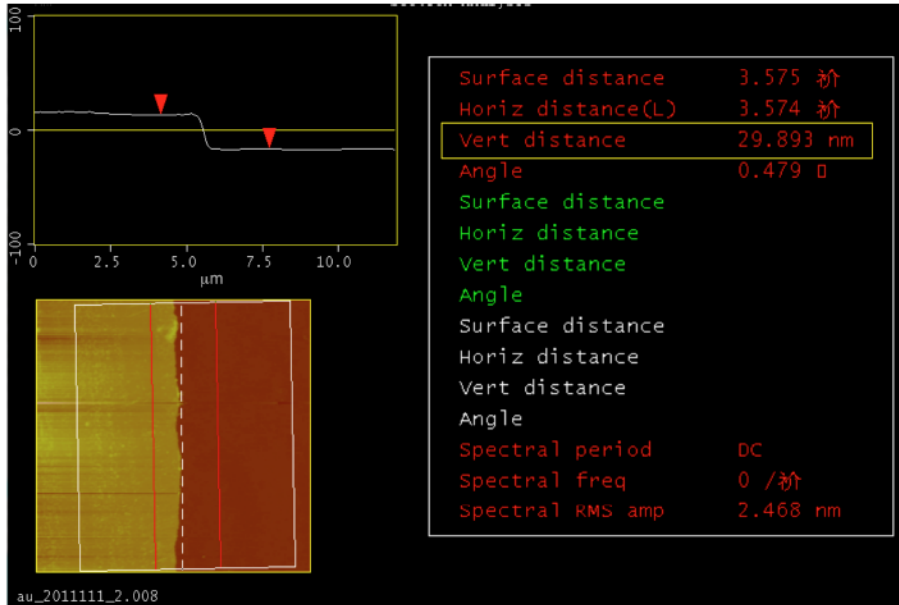


Figure 3.6: An example of foil thickness (29.9nm) measured by AFM

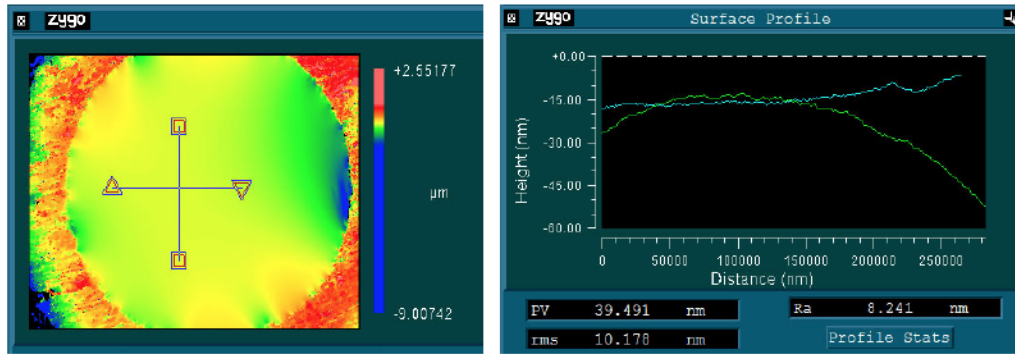


Figure 3.7: An example of free standing surface quality measured by Zygo white light interferometer

plate was checked by a white light profilometer (Newview 5000, Zygo). The flatness of a foil is typically better than 40nm, which is $1/20\lambda$ of our probe beam at 800nm, an example is given in Fig. 3.7. The above described technique has also been applied to produced free standing diamond like carbon (DLC) foil targets [80].

The sample plate that is used to mount the free standing foils are made from 1.1mm thick stainless steel by our department's machine shop. It has $7 \times 15 = 105$ holes where the foils stand on without supporting from the back.

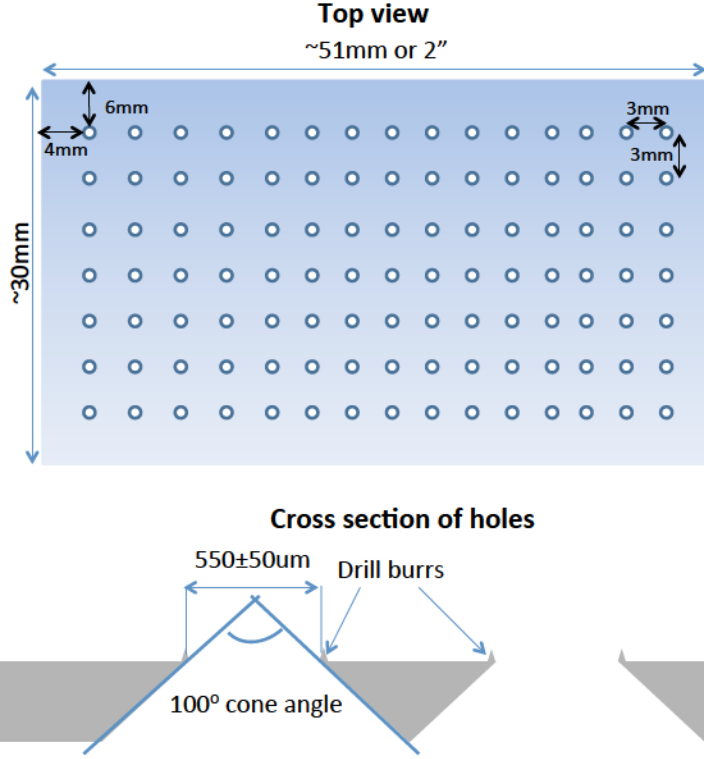


Figure 3.8: Layout diagram of a sample plate

The holes are $550 \pm 50 \mu\text{m}$ in diameter. A 100° cone angle is on the back of each hole so that the 45° incident probe beam can transmit through. Drill burrs are smoothed a little using sandpapers but not completely. These small amount of drill burrs around the holes are found to help keeping the foils flat and stretched. A diagram of a sample plate is shown in Fig.3.8.

The dielectric constant for 800nm probe at room temperature of these free standing foils is also measured. This is based on the measurement of the reflectivity (R) and transmissivity (T) of 800nm pulses at 45° incident angle. The pulses are generated by the Ti:sapphire laser system from our lab at University of Alberta. The incident laser fluence is controlled to be less than $0.01 \text{J}/\text{cm}^2$, which is two orders of magnitude below the damage threshold. The measured R and T is then used to extract the corresponding complex reflective index ($\tilde{n} = n + ik$). This technique is based on the transfer-matrix method [81],

which can calculate R and T of a uniform and isotropic material with known thickness and refractive index by solving the Maxwell equations in the form of matrices. The inverse application of this technique [20, 22] is used to find out the corresponding \tilde{n} of a material with known R and T at certain thickness, by generating a high resolution R and T to \tilde{n} mapping. The dielectric constant is obtained from the relation $\varepsilon = \tilde{n}$. The ε of our free standing gold thin foil is found to be $-(22.4 \pm 1.8) + i(1.26 \pm 0.10)$ at 1.55eV, which is in reasonable agreement with Johnson and Christy's measurement of $-(23.9 \pm 0.3) + i(1.5 \pm 0.2)$ [48].

3.3.2 Experimental Setup

The experiment to verify the uniform heating of free standing gold thin foils by isochoric laser heating was carried out at ALLS with the assistance of Dr. Vahit Sametoglu, who was a postdoctoral fellow at U of A. The 10Hz beam light at ALLS was used for our experiment. This laser system is custom made by Thales Inc.. It has one regenerative amplifier and two multi-pass amplifiers in its chirped pulse amplification system (CPA) [82], which can deliver 45fs FWHM laser pulses centered at 796nm, with a maximum pulse energy of 350mJ after compression. However, the flashlamp of the pump laser for the second amplifier was not in good condition during our beam time, which significantly distorted the beam quality. For our experiment, we used only the first amplifier for better laser beam quality. The amount of pulse energy delivered by the first amplifier is more than sufficient for the experiment. A schematic diagram of this laser system is shown in Fig. 3.9.

The general concept of our experimental setup is described below, while the corresponding diagram for the measurement is shown in Fig. 3.10.

(1) The thin 30nm gold thin foil target is excited by a 400nm laser pulse with 45fs pulse duration at normal incident. The state of the excited material is referred to by its excitation energy density (ΔE_D), i.e. absorbed energy per unit

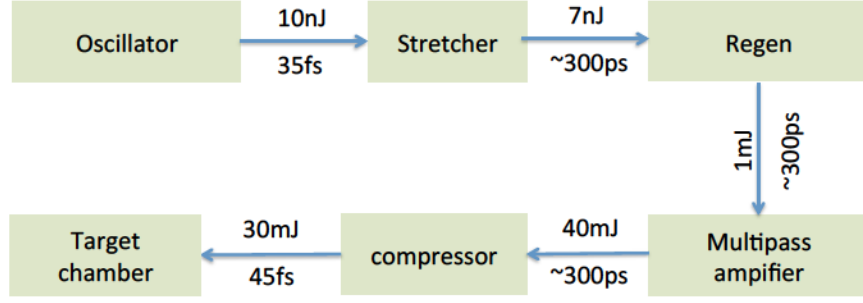


Figure 3.9: Schematic diagram of the laser system we used at ALLS. It amplifies a 10nJ laser pulse to 30mJ by the chirped pulse amplification (CPA) technique.

mass in Joule/kg. The absorbed energy is obtained by subtracting the reflected and transmitted portion from the incident energy, i.e. $E_{abs} = E_{inc} - E_{ref} - E_{tra}$. The incident, reflected and transmitted energies are measured by three photodiodes (PD_I, PD_R and PD_T) respectively. The spatial distribution of those beams are measured by two CCD cameras (CCD_T and CCD_R). CCD_T measures the transmitted beam when a foil exists during the experiment, and the incident beam profile is measured when there is no foil on the beam path. CCD_R is responsible for the measurement of the reflected beam from the foil surface. The mass of the excited material $M = A \times l \times \rho$, where A is the excited area, l is the thickness of the foil, and $\rho = 19300 \text{ kg/m}^3$ is the density of gold under room conditions. In our measurement, A is confined within the center circular region of the excited area, whose diameter is $20 \mu\text{m}$, which is about 1/3 of the FWHM of the focused pump beam, and the corresponding absorbed energy in the region is used to calculate ΔE_D .

(2) Two 800nm probe pulses from the front and rear sides of the foil at 45° incident angle are used to measure the reflectivity simultaneously as a function of time. The FWHM of the probe beams is about $500 \mu\text{m}$ on the target surface, which is almost an order of magnitude larger than the pump beam. The polarization of the probe pulses are set to $P\text{-pol}$, which is cross-polarized to the 400nm pump pulse. The $P\text{-pol}$ pulse is considered to be more

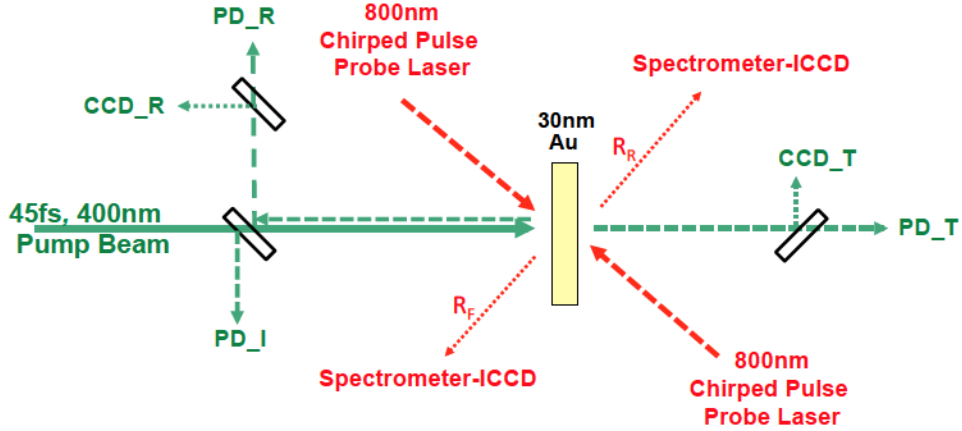


Figure 3.10: Conceptual layout diagram to verify the uniform excitation of a 30nm gold thin foil excited by 400nm, femtosecond pump pulse. Reflectivities of the excited foil from front and rear sides (R_F and R_R) are measured with two chirped pulse probes simultaneously

sensitive to temperature and density gradient than S - pol , since it has electric field component oscillating in transverse direction of the foil. If the foil is not uniformly heated throughout its thickness, one would expect the reflectivities from front and rear to be different from each other. Here the probe pulses are negatively chirped, i.e. short wavelength component comes earlier than the long wavelength. This was used to map the temporal evolution of reflectivity in the spectral regime. For each side of reflectivity, a spectrometer is used to decode the reflectivity evolution as a function of wavelength, and the spectra are imaged onto an ICCD camera. This chirped pulse technique can measure the time resolved evolution of reflectivity in a single shot, which simplifies the experiment when compared to the traditional delay line scan method [20].

3.3.3 Single Shot Chirped Pulsed Probe Technique

To get a linearly chirped probe pulse while keeping the pump pulse to its compression limit, we used two different grating compressors, i.e., one for the pump pulse, and the other for the probe. A diagram of grating compressor is shown in Fig.3.11 In such compressor, if the normal separation between the

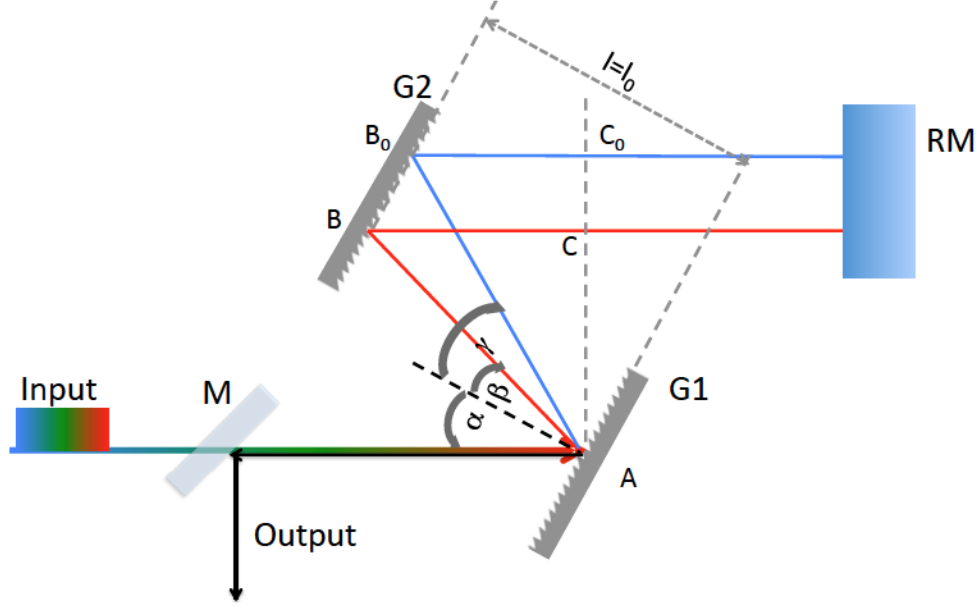


Figure 3.11: Layout of a grating compressor. It consists of two gratings (G1 and G2), a retro-mirror (RM) and an output mirror (M).

two gratings G1 and G2 are properly set corresponding to the input pulse i.e. $l = l_0$, it can compress the positive chirped (long λ component ahead of short λ component) input from the amplifier to its Fourier transform limit

$$\Delta f_{pulse} \times \Delta \tau_{pulse} \approx 0.44 \quad (3.1)$$

where Δf_{pulse} is the frequency bandwidth of the laser pulse, and $\Delta \tau_{pulse}$ is a minimum FWHM pulse duration, assuming the laser pulse shape is Gaussian in time. However, if the path length $l \neq l_0$, then the pulse can be over or under compressed, and the output will have negative or positive chirp.

The mechanism of a grating compressor is that a grating can separate different frequency components of a pulse to create group velocity dispersion (GVD). According to the grating equation,

$$d \sin(\alpha + \beta) = m\lambda \quad (3.2)$$

where α and β are the incident and diffraction angle with respect to the

grating normal, d is the grating pitch, λ is the wavelength of certain component in the beam, and m is any integer. Usually a grating is optimized for $m=1$. The beam path \overline{ABC} of the redder component in Fig. 3.11 can be written as a function of grating separation l ,

$$\overline{ABC} = AB + BC = \frac{l}{\cos(\beta)} + AB \cos(\alpha + \beta) = \frac{l}{\cos(\beta)}(1 + \cos(\alpha + \beta)) \quad (3.3)$$

Similarly, the beam path for the bluer component $\overline{AB_0C_0}$ is given in Eq.3.3 by replacing β with γ . Once the incident angle of the beam to the compressor is set, the dispersion angles for each component are fixed, and the only variable is l . For a positive chirped input pulse whose redder component is T_0 ahead of the bluer component, one can set l to fulfil the condition that,

$$T_0 c = \overline{AB_0C_0} - \overline{ABC} \quad (3.4)$$

where c is the speed of light.

The width of a chirped pulse was measured by frequency resolved optical gating (FROG) implemented with transient grating (TG) technique [83, 84]. As shown in Fig.3.12, when the laser pulse passes through a mask with three small holes (see inset), while the beam is co-center with the mask, three small portion of the beam will pass through with almost equal energy each. For a properly prepared femtosecond pulse without spatial chirp, each pulse contains the same phase information as the main pulse. Sub-beams E_1 and E_2 are focused by a spherical mirror onto a piece of fused silica glass after reflected on a mirror mounted on a motorized delay line. These two pulses generates periodical interference in the glass, which forms a transient grating whose k-vector $k_{TG} = k_1 - k_2$. The third sub-beam E_3 goes through similar path length as E_1 and E_2 without travelling on the delay line, before being focused by the same spherical mirror to the same point in the glass. Such beam is scattered

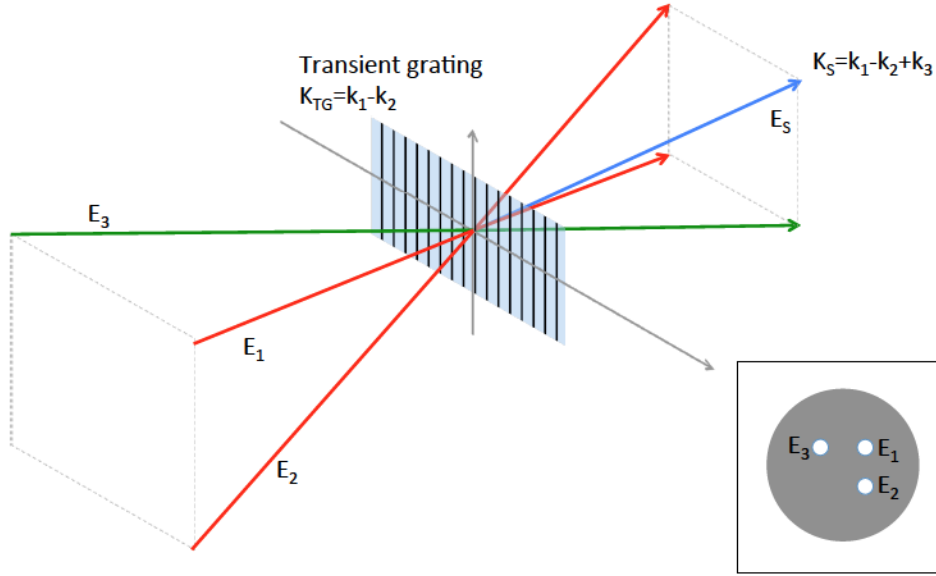


Figure 3.12: Transient grating technique. Beam E_1 and E_2 generates transient grating effect in a piece of glass, when beam E_3 passes through the grating, it is scattered according to Bragg's law and part of its energy propagates in the direction of E_s . Inset is the mask that used to select E_1 , E_2 and E_3 from the beam to be measured.

according to the Bragg condition in reciprocal space $k_S = k_3 + k_{TG}$. The scatter beam is collected by a spectrometer. The full phase information for the laser pulse then can be obtained by scanning the motorized delay line.

The electric field of E_S has the form [85],

$$E_S(t, \tau) \propto E_1(t - \tau)E_2^*(t - \tau)E_3(t) = E(t)E^2(t - \tau) \quad (3.5)$$

where τ is the separation between E_3 and E_1 (or E_2) caused by the delay line. The amplitude of the three beams should be similar, which is represented simply by E . The intensity of the FROG signal on a spectrogram of laser frequency vs. time delay is ,

$$I_{FROG}(\omega, \tau) \propto \left| \int_{-\infty}^{\infty} E(t)E^2(t - \tau) \exp(-i\omega t) dt \right|^2 \quad (3.6)$$

An example of FROG scan is given in Fig.3.13. The wavelength vs. time slope is 2.5nm/ps. According to Eq. 3.5, for a Gaussian pulse , the maximum of

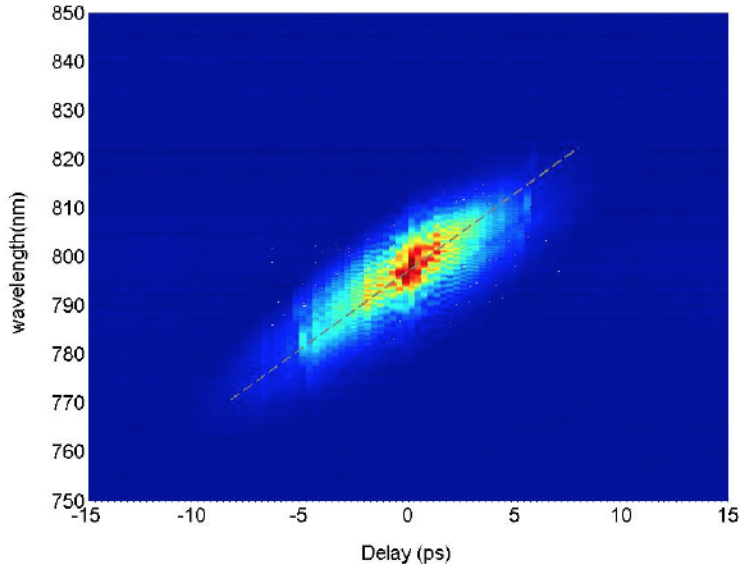


Figure 3.13: Spectrogram measured by TG-FROG technique of the probe pulse that is used for the experiment. The best fit slope is 2.5nm/ps, which corresponds to 3.8nm/ps for the actual linear chirped pulse

E exists when $\tau = 2/3$ [86, 87]. As a result the slope on the spectrogram is only 2/3 of the real signal, and the real slope here should be 3.8nm/ps. This time-wavelength relation agreed with the cross-check by delaying the probe pulse with known distance on the delay stage, and observing the on set of reflectivity change in probe pulse due to pump pulse excitation. The FWHM spectral width of the Ti:sapphire laser system is 24nm, so the nominal FWHM pulse duration is 6.5ps. The time resolution of a linear chirped pulse is governed by the relation [88],

$$\delta t = \sqrt{\Delta T_0 \Delta T} \quad (3.7)$$

where ΔT_0 is the minimum width of the laser pulse, which is about 45fs FWHM for this laser system, and ΔT is the chirped pulse with a 6.5ps FWHM duration. Accordingly, the probe pulse resolution is about 540fs.

The TG-FROG system is also used to measured the width of 400nm pump pulse. The 400nm pump is produced by second harmonic generation (SHG)

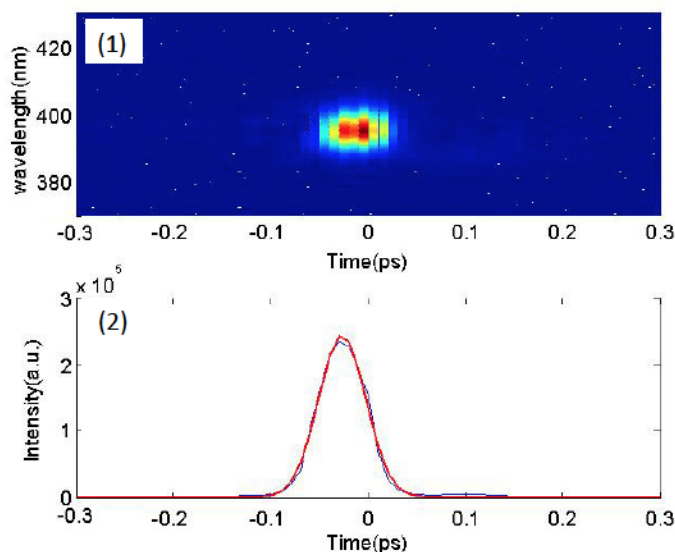


Figure 3.14: (1) Spectrogram of the 400nm pump pulse, and (2) its spectral integrated intensity as a function of time (blue line). The red line is the best Gaussian fit with 56fs FWHM, which corresponds to 45fs FWHM of the actual pulse

from the 800nm pulse using a $600\mu\text{m}$ thick KDP crystal. This 800nm pulse is compressed to its minimum duration using another grating compressor housed in a vacuum chamber. The FWHM of the 400nm pulse on the FROG spectrogram is 56fs as shown in Fig.3.14, which corresponds to 45fs FWHM of the actual pump pulse, after using the correction factor of 1.22 for a Gaussian pulse [87].

A detail experimental setup diagram is given in Fig. 3.15.

(1) The femtosecond seed pulse is generated from an oscillator and chirped to a few hundred picoseconds before being amplified in the regen and multi-pass amplifier. The amplified pulse is separated by a 90:10 beam splitter (BS).

(2) 90% of the laser energy goes into the pump pulse compressor housed in a vacuum chamber (10^{-6} Torr). This pulse is compressed to its minimum width, and passes through a KDP crystal for second harmonics generation. The 400nm pump pulse is reflected by a few dichroic mirrors (400nm high reflectivity and 800nm high transmissivity) to eliminate the 800nm component, and goes into the target chamber to be focused by a parabolic mirror of 35cm effective

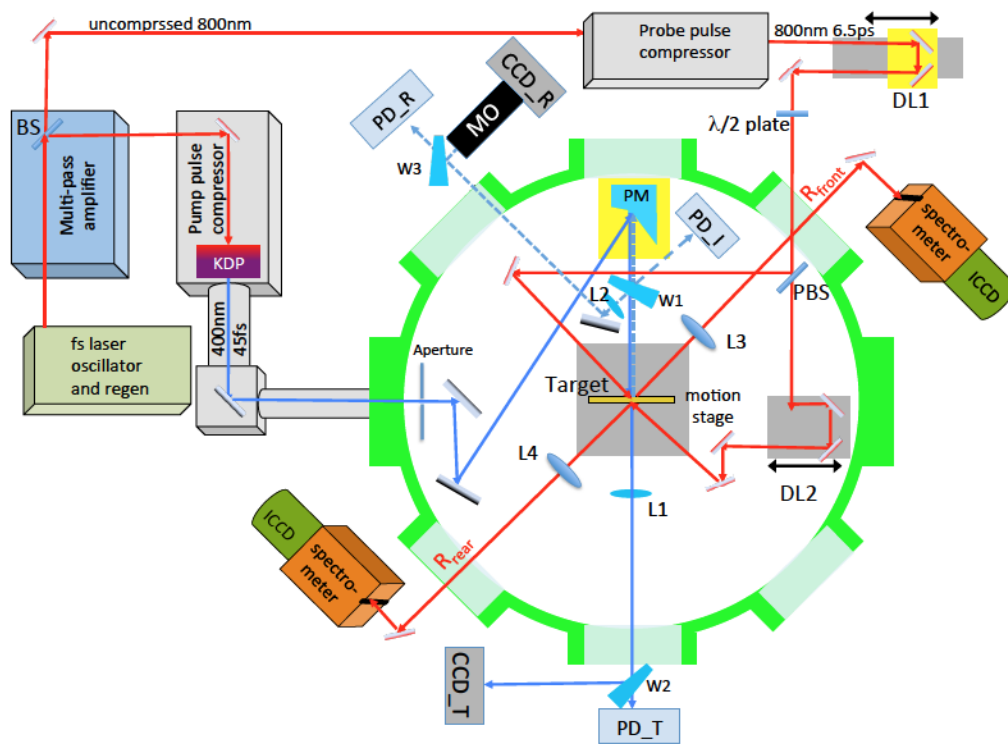


Figure 3.15: Complete experimental setup of 400nm pump pulse excitation, and 800nm front and rear chirped pulse probe experiment to examine the uniform heating of a 30nm free standing gold thin foil (not to scale). Detailed description is in the context.

focal distance. The beam is focused onto the 30nm free stand gold thin foil at normal incident. The target is mounted on a three axes motion stage. The size of the focal spot is controlled by an aperture located near the chamber entrance, which changes the F-number of the focal condition. The typical FWHM of the focal spot is $64\pm 2\mu m$. The input pump pulse energy is sampled by a thin wedge (W1) to a photodiode (PD_I). The energy transmitted from the foil is collected by a lense of FL=15cm (L1). This energy is measured by another photodiode(PD_T). The beam profile is measured by a CCD camera(CCD_T). The reflected energy from the pump pulse is sampled by the other surface of W1 and measured by photodiode PD_R. The reflected spot profile is measured by CCD_R with imaging optics consist of an FL=25cm lens (L2) and a 5X microscope objective (MO). An example of energy density measurement at the center of the heated area is given in Fig.3.16.

(3) 10% of the laser energy goes into the probe pulse compressor. The beam is “over compressed” to a negative chirped of 6.5ps as described before. It is separated into two pulses by a pellicle beam splitter (PBS). One measures the reflectivity from the front surface at 45° incidence, the other one measures the reflectivity from the rear surface symmetrically. The polarization of the probe beams are set to *P-pol* by a half wave plate. The reflected probe beams are imaged onto the slits of two spectrometers (MS260i, Oriel) equipped with 1200line/mm gratings. The slit width is set to $100\mu m$, which corresponds to $10\mu m$ in space on the target surface. Two intensified CCD cameras (ICCD, DH720, Andor) are coupled to the spectrometers respectively. The image on the slit is re-imaged on the vertical direction of the ICCD, while the spectral/time evolution of the probe beam is streaked in the horizontal direction.

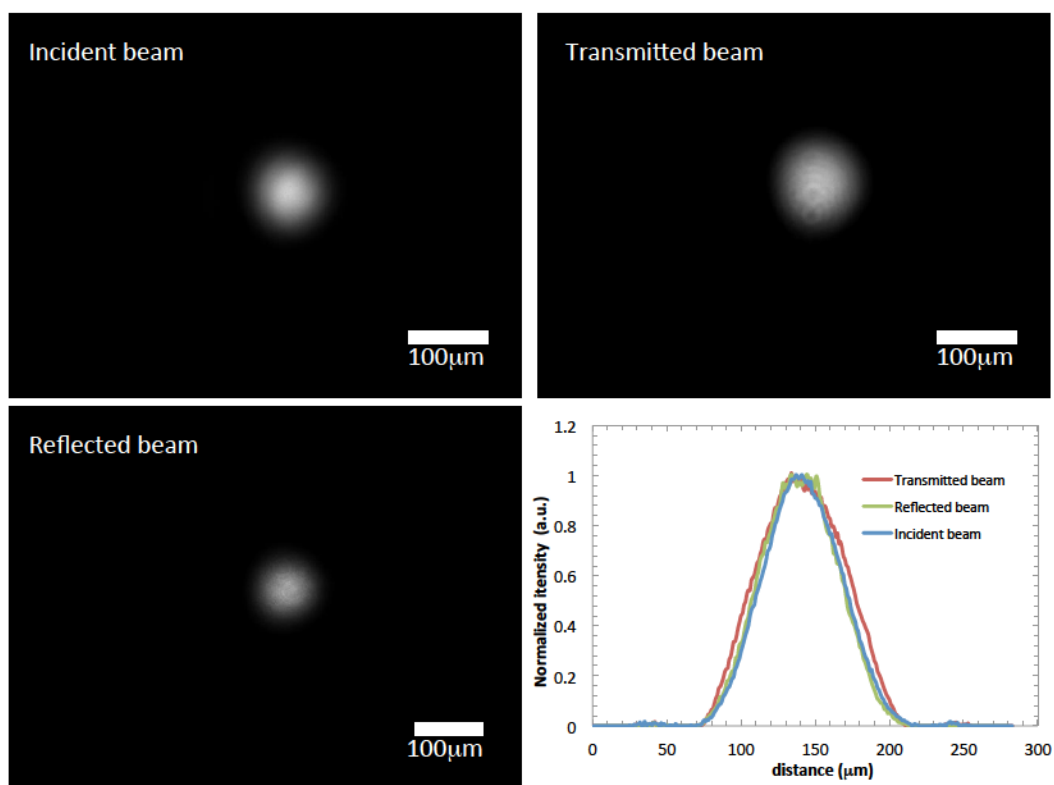


Figure 3.16: An example of energy density calibration of an excited free standing thin foil. The incident, reflected and transmitted energies measured by photodiodes are $14.2\mu J$, $5.7\mu J$ and $1.1\mu J$. According to the CCD images of these three beams on the target, the energy encircled in the center $22\mu m$ diameter area (1/3 of the FWHM) takes up 8.4% ($1.2\mu J$), 9.1% ($0.51\mu J$) and 6.6% ($0.075\mu J$) of the measured energy of each beam respectively. As a result, $0.61\mu J$ is absorbed in these area, which corresponds to an absorption rate of 51%. The absorbed fluence in this area is $0.16J/cm^2$. If the 30nm gold foil is uniformly excited, the corresponding energy density is 2.8MJ/kg.

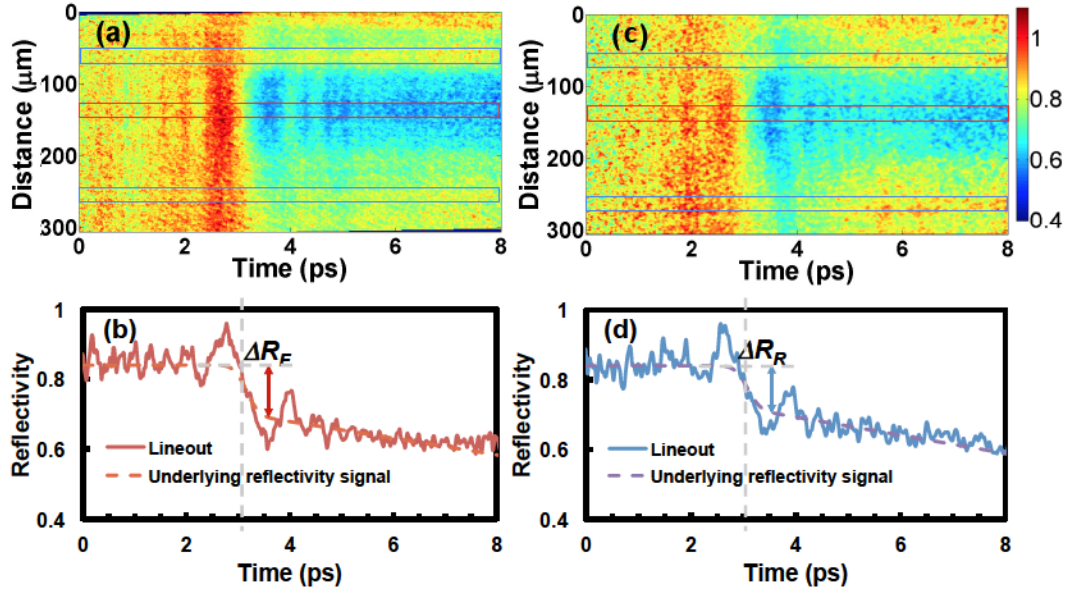


Figure 3.17: An example of front and rear reflectivities of the probe pulses imaged on the ICCD cameras.

3.4 Experimental Results

The reflectivities of the probe pulses from the front (R_F) and rear side (R_R) are quantitatively analysed from the images taken from the ICCD cameras. An example of a foil excited to 4.5MJ/kg is shown in Fig.3.17. In this figure, (a) and (c) are the images taken by the front and rear cameras. The original horizontal axis is the wavelength of the probe pulse, which is converted to time delay using the linear chirped mapping relation 3.8nm/ps as discussed above. The vertical axis is the spatial image of the slit on the spectrometer. To better understand the temporal evolution of the heated area, lineouts of the center 20 μm of the excited region (red square), after normalized by the unheated region (blue squares), are given in (b) and (d) of Fig.3.17.

A major feature of the reflectivity as a function of time shown in Fig.3.17 is that it drops at around 3ps, when the excitation pulse comes. As can be seen that there are aperiodic ripples on both R_F and R_R , whose frequency increases with the temporal distance from these initial falling edge of the reflectivity right after the laser heating. Such ripples are the result of cross phase modulation

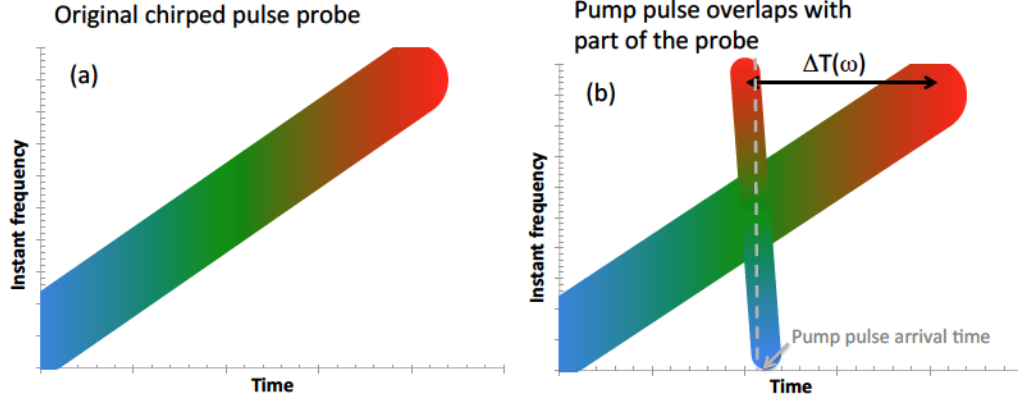


Figure 3.18: (a) Original frequency-time mapping of the chirped pulse probe. (b) When part of the probe pulse overlaps in time with the pump in the gold thin foil, optical Kerr effect happens inside the foil, and XPM effect modulates the phase of that part of the pulse.

(XPM) of part of the probe pulse occurs in the target when it overlaps with the pump pulse. The phase shifted portion of the probe pulse enters the spectrometer and interferes with the rest of the original probe pulse. Such effect is usually called frequency domain interference effect (FDI). This combination effect of XPM and FDI was observed in glass substrate before [89]. A schematic diagram that explains the XPM process is shown in Fig. 3.18.

The FDI effect of two pulses is the Fourier transform of two pulses from time domain to frequency domain. Such phenomenon is achieved with the help of a grating inside the spectrometer. For two pulses with electric fields amplitude in time domain,

$$E_{pr}(t) = E_0(t) \exp(i\omega_0 t) \quad (3.8)$$

$$E_{ref}(t) = \sqrt{A} E_0(t) \exp(i\omega_0 t + \Delta T(\omega)) \quad (3.9)$$

where A is the intensity ratio of the second pulse normalized to the first one, ΔT is the separation of these two pulses, and ω_0 is the center frequency for each pulse. The Fourier transform for the sum of two pulses is [90],

$$F[E_{pr}(t) + E_{ref}(t)] = E(\omega - \omega_0)[1 + \sqrt{A} \exp(i\omega \Delta T)] \quad (3.10)$$

where $E(\omega)$ is the Fourier transform of $E(t)$. In reality, one observes the intensity instead of the amplitude, so that,

$$|F[E_{pr}(t) + E_{ref}(t)]|^2 = E^2(\omega - \omega_0)[1 + A + 2\sqrt{A} \cos(i\omega\Delta T)] \quad (3.11)$$

Obviously, the aperiodic fringes of FDI is inversely proportional to ΔT . As can be found from Fig.3.18 (b), ΔT for each frequency ω is determined by its temporal or spectral difference with the corresponding component of the pump pulse, which explains why the frequency of the fringes increases with their own temporal distance from the initial falling edge of the reflectivity. One can also find that the oscillation term in Eq.3.11 is proportional to \sqrt{A} instead of A , so that those fringes are easy to observe even when only a small portion of the probe pulse is modulated by XPM, e.g. 1% of the modulated energy can correspond to fringes of 10% amplitude of the DC signal.

Due to the chirped pulse resolution of 540fs, the falling edge of reflectivity can be significantly broadened. One may use those aperiodic FDI fringes to locate when the pump and probe pulse overlap in time. This can be done by finding out pump-probe overlap time T_0 that can best fit to those fringes according to Eq.3.11. An example is given in Fig.3.19.

Although those fringes can provide information of the pump pulse arrival time, they also mask the actual evolution of reflectivity. For the probe pulse reflectivity after the pump pulse excitation, our treatment is to do a linear fit from 540fs after T_0 to a certain point as the change of R_F and R_R still linear, and extend this line backward to 45fs after T_0 . For the reflectivity before the pump pulse, from the beginning of the probe pulse time window to 45fs before T_0 , the probe pulse reflectivity is fitted by a straight line as the cold foil reflectivity. The portion from 45fs before to 45fs after T_0 is simply connected by a straight line, because the evolution of probe pulse reflectivity during the pump pulse excitation is not known in detail. At the end, the combined signal

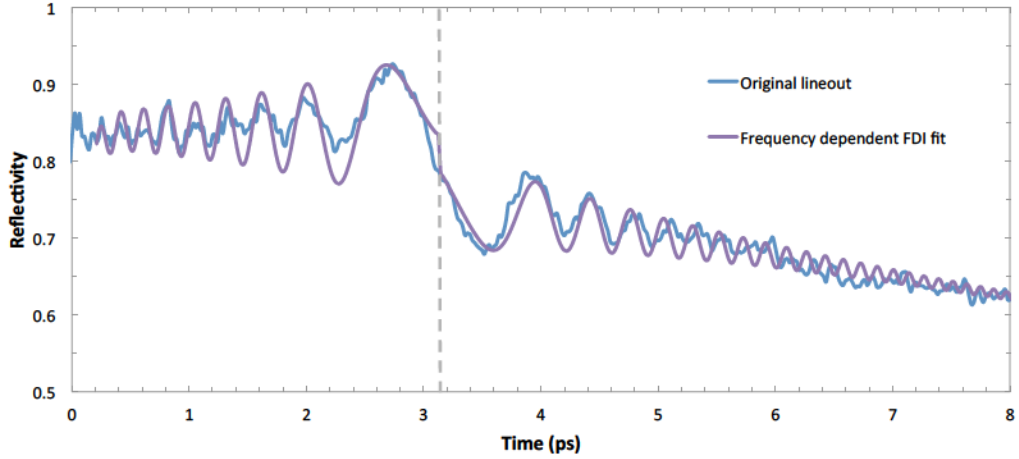


Figure 3.19: Fit to the XPM-FDI ripples using the law of fringe frequency. The best fit gives the pump pulse arrival time around 3.15ps.

is convoluted with a Gaussian instrumental function of 540fs FWHM, such as shown in Fig. 3.17 (b) and (d). The initial changes of R_F and R_R right after the laser excitation are measured by the difference between cold foil reflectivity and our fitting to the lineout at 540fs, which are marked as ΔR_F and ΔR_R .

The plot of R_F and R_R as a function of absorbed laser energy flux (ΔI), or the average energy density (ΔE) of the heated foils are shown in Fig.3.20. One can see that the initial change of R_F keeps increasing with absorbed laser intensity, or energy flux, however, the initial change of R_R reaches its maximum at $6.4 \times 10^{12} W/cm^2$ and does not change more until at a later time.

To get a better view of such phenomena, the comparison of ΔR_F and ΔR_R as a function of absorption energy flux is shown in Fig.3.21. It seems that both ΔR_F and ΔR_R are close to each other below $6.4 \times 10^{12} W/cm^2$, or 5MJ/kg. Beyond that, ΔR_F rises far more significantly while ΔR_R still stays little changed. This is an indication that the foil has a significant temperature gradient above $6.4 \times 10^{12} W/cm^2$. At a later time, according to Fig.3.20, the thermal gradient starts to reduce, but it takes a few picoseconds for such process, which is much longer than the lifetime of ballistic electrons. Such phenomenon shows that above a critical absorption energy flux, or energy density, a 30nm gold thin

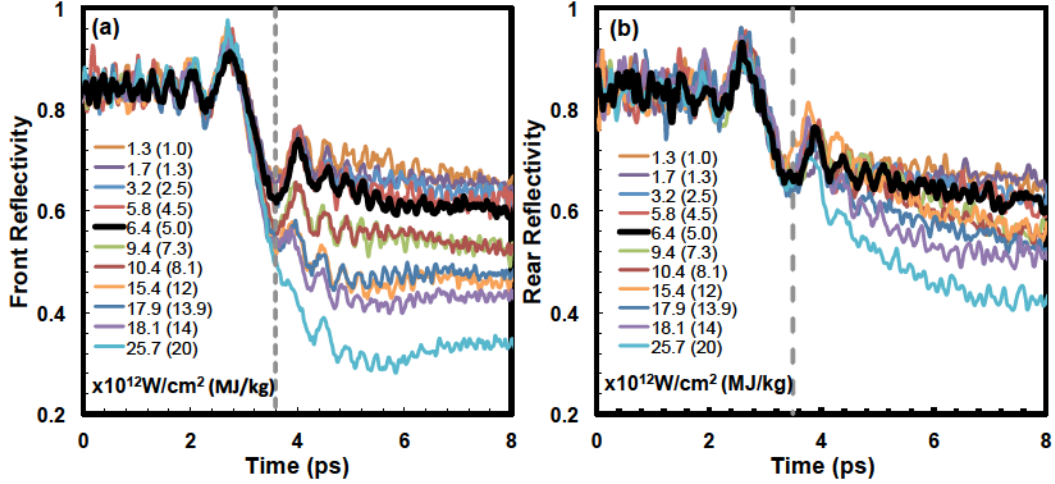


Figure 3.20: Lineouts of (a) reflectivity from the front surface and (b) rear surface as a function of absorbed laser intensity, or average energy density. The dash line indicates 540fs after the initial excitation.

foil cannot be uniformly excited by ballistic electron transportation alone. A thermal gradient is formed after the decay of such electrons and the electrons are thermalized. The subsequent energy transportation from the front surface to the rear is carried by thermal diffusion [13], which takes a few picoseconds and the significant disassembly can happen at the same time [16] as electrons also couple energy to the lattice system.

As a major result, it seems that using the 45fs pump at 400nm, the 30nm gold foil can only be uniformly excited upto $\sim 5 MJ/kg$, or an equivalent absorbed peak intensity of $\sim 6.4 \times 10^{12} W/cm^2$. Beyond that, the isothermal condition and isochoric heating condition no longer hold, and a thermal gradient as well as mixture of states can exist. This gives an upper limit to the investigation of single state warm dense gold. The measurement of AC conductivity in warm dense gold will be described in the next chapter, then the result will be used to give some interpretation of such a limit for uniform excitation.

It is also noticeable that for laser flux above $\sim 6.4 \times 10^{12} W/cm^2$, R_R continue to catch up R_F in picosecond time scale, which is significantly longer than the life time of the ballistic electrons in gold. This is because a thermal gradient

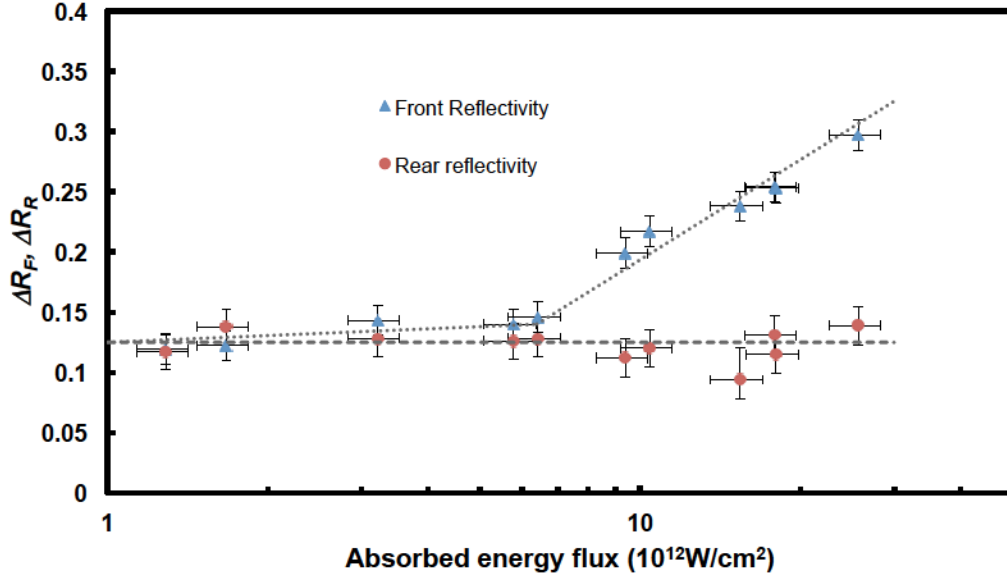


Figure 3.21: Comparison of the initial change of reflectivity from front and rear surfaces at 540fs after the laser heating. The dash and dotted lines are for eye guidance

between the front and rear sides is formed after the electrons are thermalized, which should happen within a picosecond [9], and the energy from the front has to transfer to the rear side by electron thermal diffusion. The speed of electron thermal diffusion depends on the temperature and density of the electrons, which is not well known in warm dense matter state. For gold, it is generally considered to be within 10nm/ps [13], so it takes a few picoseconds to transport energy through a 30nm foil. As can be seen from Fig.3.22, at 5ps after the pump pulse, the deviation of the front and back reflectivities for absorbed energy flux above $\sim 6.4 \times 10^{12} \text{W/cm}^2$ becomes less pronounced than at 0.54 ps. This is likely because significant amount of energy is transported from the front to the back via the thermal diffusion process.

3.5 Summary

In this chapter, the uniform heating of a 30nm free standing gold thin foil by femtosecond laser pulse excitation was tested by measuring the probe pulses

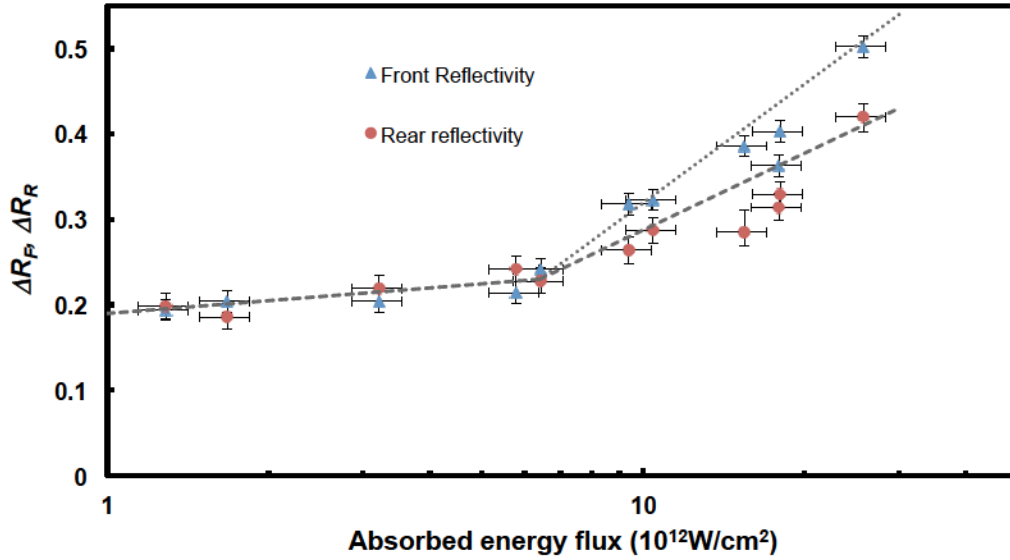


Figure 3.22: Comparison of the initial change of reflectivity from front and rear surfaces at 5ps after the laser heating. The dash and dotted lines are for eye guidance

reflectivities from the front and rear sides of the foil simultaneously. We found that using a 45fs FWHM laser pulse at 400nm, the foil can be excited up to 5MJ/kg. Thermal gradient in the thin foil target was observed above this energy density, which sets an upper limit for isochoric and isothermal laser heating in our experimental condition.

Chapter 4

AC Conductivity Measurement of Warm Dense Gold

The study of electrical conductivity has long been of interest in warm dense matter investigations. The electrical conductivity of WDM provides information about energy and particle transport on the one hand, and on the other hand, it is important for the understanding of laser matter interactions.

Early studies of electrical conductivity in WDM include the measurements of reflectivity of shocked compressed material [91], short pulse laser self absorption [11, 29, 18], and direct measurement on capillary exploded metal wires [92, 93]. However, such measurements are either indirect, e.g. depend on theoretical models [56, 94] to extract data, and/or were done in a mixture of states.

The concept of isochoric laser heating allows the single state measurement of AC conductivity ($\sigma(\omega)$) at optical frequencies [19]. The AC conductivity evolution of single state warm dense gold was first deduced from multiple shot pump-probe measurement of reflectivity (R) and transmissivity (T) by changing the probe pulse to different time delays related to the pump pulse [20]. In that study, an essentially constant in time behaviour of AC conductivity was observed in the excited gold thin foil before disassembly [16], which was referred to as quasi-steady state (QSS). Because both electron and lattice temperatures

are changing within that time window, the AC conductivity should respond to such change. However, due to the shot to shot fluctuations, it is possible that small changes in AC conductivity were masked. In my study, a chirped-pulse probe technique was developed as described in the previous chapter. This technique provided an opportunity to study the AC conductivity evolution in a 6.5ps window within a single shot.

4.1 Single Shot Chirped Pulse Measurement Reflectivity and Transmissivity

The front and rear reflectivity of warm dense gold was measured at wavelength around 800nm as indicated in Chapter 3. The warm dense gold is a 30nm free standing gold foil isochorically heated by a 400nm, 45fs FWHM laser pulse at normal incident, which was found to be uniformly heated upto 5MJ/kg as discussed in Chapter 3 [95]. To obtain the AC conductivity of an excited gold thin foil, a chirped-pulse probe center at 800nm is incident on the foil surface at 45° with *P-pol*. The reflectivity and transmissivity (R and T) of the probe pulse as a function of time were mapped linearly in the spectral regime, so two spectrometers coupled with ICCD cameras were used to decode the information, which is similar to the front and rear side reflectivity measurement. The measured R and T were used to extract the complex refractive index $\tilde{n} = n + ik$ using the inverse transfer-matrix method [81, 20]. The complex dielectric constant ε is the square of \tilde{n} . The complex AC conductivity σ is related to the dielectric constant [34],

$$\sigma(\omega) = (1 - \varepsilon(\omega))i\frac{\omega}{4\pi} \quad (4.1)$$

The experimental setup is shown in Fig.4.1, which is similar to the front and rear reflectivity measurement described in Chapter 3, except that there

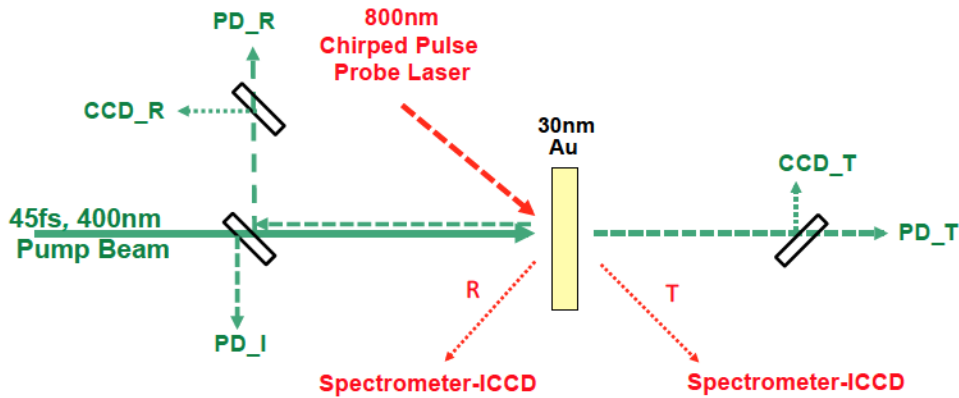


Figure 4.1: Layout diagram of pump probe experiment. A 30nm gold thin foil is excited by a 400nm, 45 femtosecond pump pulse. A chirped pulse probe of 6.5ps FWHM centered at 800nm is used to measure the reflection and transmissivity of the foil as a function of time

is only one probe beam from the front surface of the thin foil, and the reflectivity and transmission of this probe beam are measured simultaneously. The measurement was also carried out at the Advanced Laser Light Source Facility (ALLS), with the help of Dr. Matt Reid from the University of Northern British Columbia, and Dr. Sean Kirkwood from the University of Ottawa.

4.2 Evolution of AC Conductivity in Warm Dense Gold

The lineout of reflectivity and transmissivity from the original image is taken by comparing the center of the heated region with the cold region as those for front and rear reflectivity measurement discussed in Chapter 3. Ripples caused by XPM-FDI effects (see Chapter 3 for detail) are overlaid on the R and T data. The evolution of R and T after the laser excitation is fitted by a two-piece spline fit. The first part of the spline is a linear function starting from 45fs after pump pulse excitation, the second part is a quadratic function with the same derivative and value of the first part at the junction. The

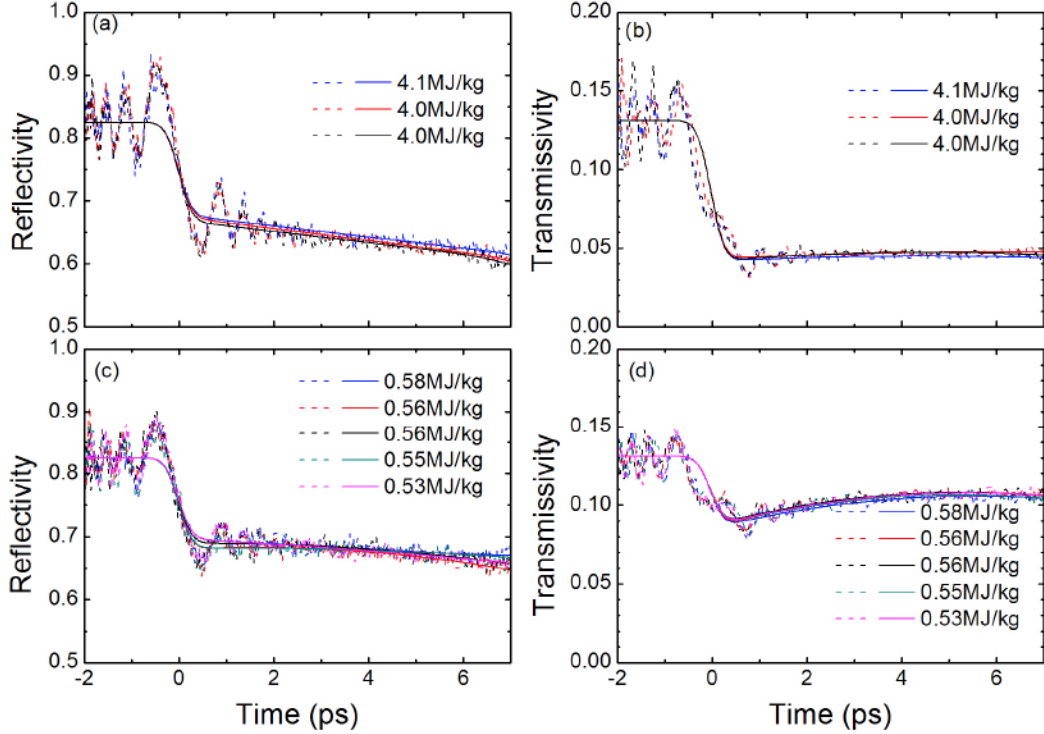


Figure 4.2: Example of the chirped pulse probe reflectivity and transmissivity measurement of the excited foils at energy density around 4MJ/kg. ((a) and (b)), and 0.55MJ/kg ((c) and (d)). The dashed lines are the lineout from the original data, while the solid lines are the best fits to them For convenience, the time at 0ps is defined as the pump pulse arrival time.

junction of the spline fit is chosen by the minimum square error condition when compared to the original data, and each piece has a minimum width of 1ps. Examples of both R and T measurements around 4MJ/kg and 0.55MJ/kg are shown in Fig.4.2. A 540fs FWHM Gaussian instrumental function is used to convolute with the best fit data to account for the chirped pulse probe resolution. We can see from the figure that the initial change of reflectivity at excitation energy density $\sim 0.5\text{MJ/kg}$ is similar to that at $\sim 4\text{MJ/kg}$, which agrees with the front and rear reflectivity measurement shown in Fig.3.21. Nevertheless, the differences in the slopes for subsequent changes are obvious. On the other hand, significantly larger amount of change is observed in the transmission at $\sim 4\text{MJ/kg}$ than that at $\sim 0.5\text{MJ/kg}$ right after laser excitation.

Using the inverse matrix method [81, 20, 22] mentioned above, the complex

AC conductivity as a function of time can be extracted from the R and T data. Two assumptions were based on: (1) the foil is uniformly excited at all times and (2) the foil thickness stays at 30nm during the 7ps time window of the measurement, In the first 100fs, the absorbed energy may not be uniformly distributed by ballistic electron energy transport, but this should not be an issue since our time resolution is about 0.5ps. It is confirmed by previous studies [16, 22], that the gold foil did not show measurable expansion for upto 6 ± 0.7 ps at excitation energy density upto 4.3MJ/kg. The corresponding AC conductivity data from our R and T measurements are show in Fig.4.3¹. As can be seen from the figure, both real (σ_r) and imaginary (σ_i) parts show a rapid change after the laser excitation at 0ps, followed by a much slower change. The rapid change is likely due to the sharp increase of T_e when the electrons are thermalized shortly after the pump pulse excitation, while the slower change is a result of electron-ion energy coupling.

4.3 Data Analysis Based on Drude Model

In the classical picture of AC conductivity, it relates to two important parameters of material according to the Drude theory [34]. One is the conduction electron density n_e , the other one is the electron collision time τ . These two parameters are discussed using the models of solid and plasma as in Chapter 2. However, they are rarely studied in the warm dense matter regime. Our measurement of AC conductivity of warm dense gold gives a good opportunity to extract these two parameters.

From Eq.4.1, the dielectric constant $\varepsilon(\omega)$ of a certain material can be calculated from its AC conductivity,

$$\varepsilon(\omega) = 1 + \frac{4\pi i\sigma}{\omega} \quad (4.2)$$

¹The unit of conductivity in CGS is s^{-1} , $1s^{-1}=10^{-9}$ S/m when converted to SI unit.

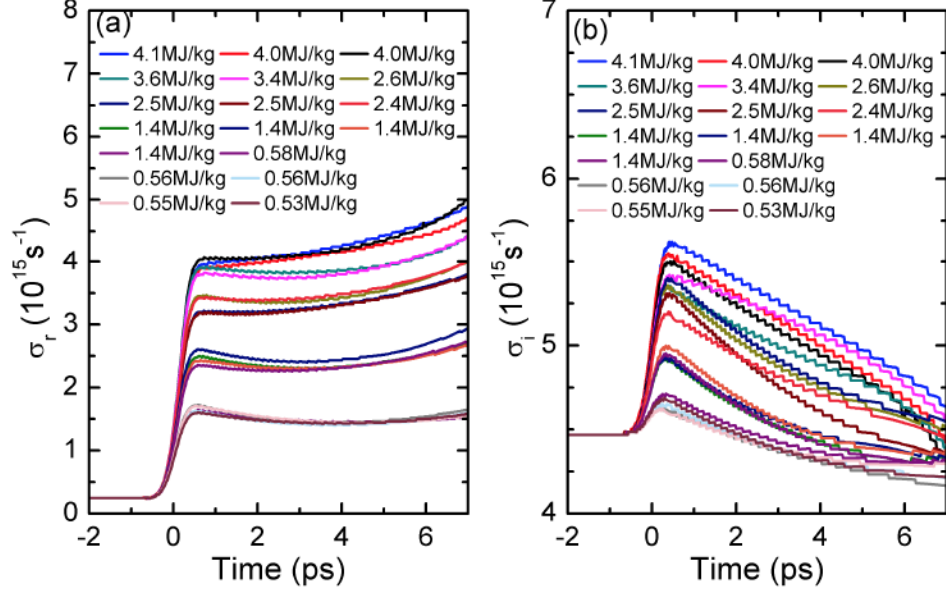


Figure 4.3: Evolution of (a) real part and (b) imaginary part of AC conductivity of warm dense gold at different excitation energy density. The data are extracted from the best fit to R and T lineouts. The labels indicate the energy densities at which the measurements were done individually. Some labels of a same energy density were taken from different shots at a same excitation energy density.

One may recall the expression of Drude theory for dielectric constant according to Eq.2.6.,

$$\varepsilon_r^{Drude} = 1 - \frac{\omega_p^2 \tau^2}{1 + \omega^2 \tau^2} \quad (4.3a)$$

$$\varepsilon_i^{Drude} = \frac{\omega_p^2 \nu}{\omega(\omega^2 + \nu^2)} \quad (4.3b)$$

n_e and τ can then be calculated by rearranging the above equations,

$$\tau = \frac{1}{\nu} = \frac{1 - \varepsilon_r^{Drude}}{\varepsilon_i^{Drude} \omega} \quad (4.4)$$

$$\omega_p^2 = (1 - \varepsilon_r^{Drude}) \left(\omega^2 + \frac{1}{\tau^2} \right) \quad (4.5)$$

$$n_e = \frac{\omega_p^2 m^*}{4\pi e^2} \quad (4.6)$$

where m^* is the effective mass of electrons. The electron effective mass in gold is found to be 0.99 ± 0.04 of the actual electron mass [48], so m^* is considered to be the same as m_e in my study.

The dielectric constant of our thin foil is $-(22.4 \pm 1.8) + i(1.26 \pm 0.10)$ at room temperature. According to the above equations, one can get n_e at room condition equals to $(4.1 \pm 0.27) \times 10^{22}/\text{cm}^{-3}$, and τ equals to $(7.9 \pm 1.5) \times 10^{-15}\text{s}$. The electron density is well below the well known value $5.9 \times 10^{22}/\text{cm}^3$ [34]. The lower value is a result of not considering contributions from interband transition and the atomic polarizability [96, 97]. To consider the contributions, we can write

$$\varepsilon_r = 4\pi n_a \alpha_a + \varepsilon_r^{IB}(\omega) + \varepsilon_r^{Drude} \quad (4.7a)$$

$$\varepsilon_i = \varepsilon_i^{IB}(\omega) + \varepsilon_i^{Drude} \quad (4.7b)$$

where n_a is the atomic density, α_a is the atomic polarizability, $\varepsilon_r^{IB}(\omega)$ and $\varepsilon_i^{IB}(\omega)$ are the real and imaginary parts of dielectric function due to band transition, and ε_r^{Drude} and ε_i^{Drude} are those due to conduction electrons as described in Drude model. i.e. Eq. 2.6.

The atomic polarizability α_a is from the electric dipole moment per unit volume of atoms. It consists of two major contributions. One is from the ionic core, which includes the nuclei and the core electrons, the other one is from the valence electrons from the outer shells [98]. For gold, the reported static atomic polarizability is within the range of 39 ± 10 in atomic unit (a.u., $1\text{a.u.} = 0.148 \text{\AA}^3$) [99, 98]. No frequency response of α_a (dynamic polarizability) for gold is reported in the literature so far. For photon energy well below the bandgap energy, the dynamic polarizability at photon frequency should be close

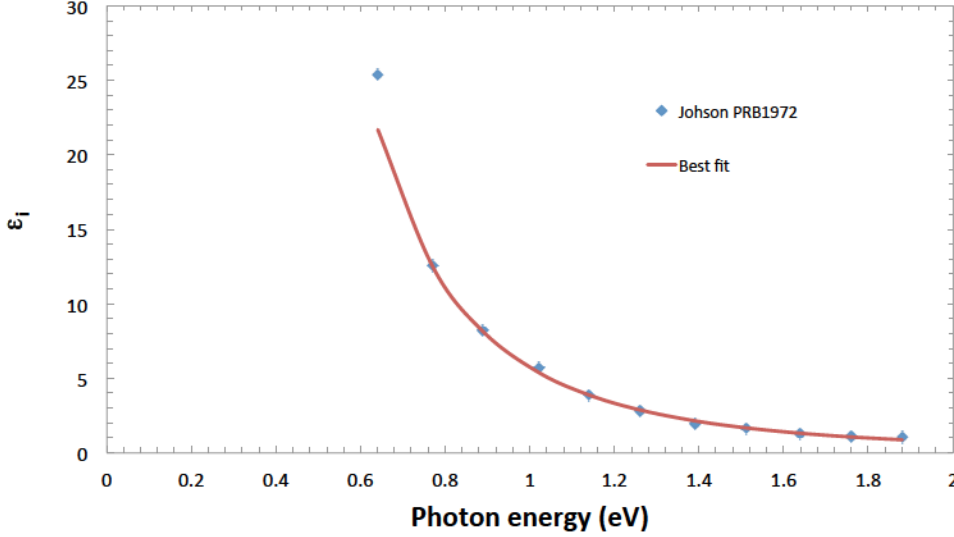


Figure 4.4: Best fit to ε_i in Johnson *et.al*'s measurement [48] from 0.64eV to 1.88eV with Drude model. The fitting parameters are $n_e = 5.88 \times 10^{22} \text{cm}^{-3}$ and $\tau = 9.3 \times 10^{-15} \text{s}$

to its static value [99]. Accordingly $\alpha(\omega)$ at 1.55eV(800nm) should be similar to the static value, since it is well below the first valence bandgap for gold at 2.4eV [48].

The interband contribution for ε_i is found to approach 0 for photon energy below 1.8eV [48, 96], so for our measurement at 1.55eV, ε_i only consists of the free electron Drude part. The real part of the dielectric function ε_r , can be obtained by Kramers-Kronig relation from the imaginary part [96],

$$\varepsilon_r^{IB} = \frac{2}{\pi} \int_{\omega_0}^{\infty} \frac{\omega' \varepsilon_i^{IB}(\omega')}{(\omega')^2 - \omega^2} d\omega' \quad (4.8)$$

where ω_0 is the onset of ε_r^{IB} , which is taken to be 1.8eV. Such a relation means that one can obtain ε_r^{IB} if the broadband value of ε_i^{IB} is known. In my calculation, ε_i^{IB} is obtained by subtracting the free electron contributions (using fitting parameters from Fig. 4.4) from reported measurements of ε_i . The free electron contribution ε_i^{Drude} is obtained from the best fit to ε_i between 0.64eV and 1.88eV reported by Johnson and Christy [48] with Eq.4.3. The fitting parameters are $n_e = 5.88 \times 10^{22} \text{cm}^{-3}$, and $\tau = 9.3 \times 10^{-15} \text{s}$ (Fig.4.4).

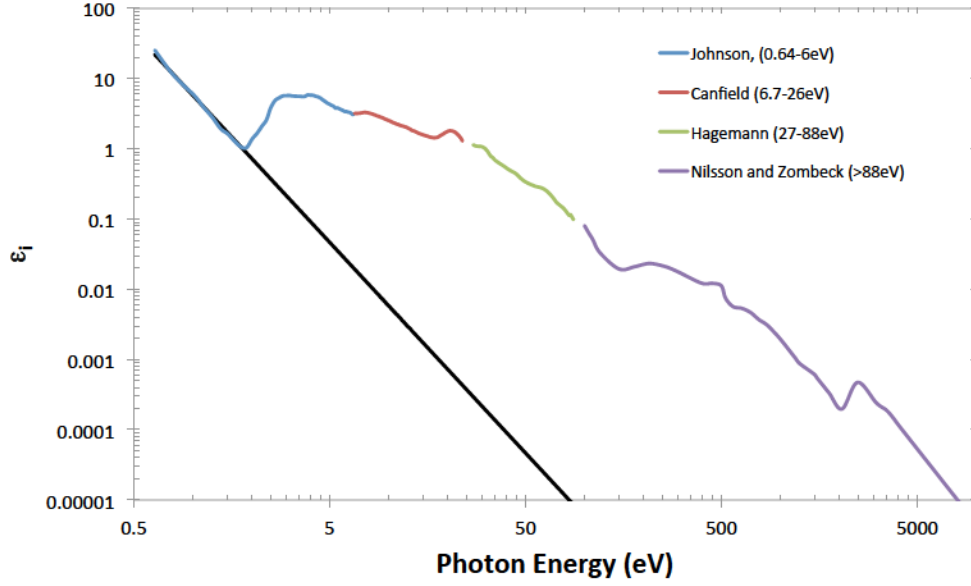


Figure 4.5: ε_i between 0.64eV and 10000eV obtained from different reports (see context). The black line is the free electron contribution (ε_i^{Drude}) to ε_i using Eq. 4.3(b) with $n_e = 5.88 \times 10^{22} \text{cm}^{-3}$ and $\tau = 9.3 \times 10^{-15} \text{s}$

The broadband dielectric constant upto 10keV as shown in Fig.4.5 consists of the data reported from different measurements within different range: (1) 0.64-6eV by Johnson *et.al* [48], (2) 6-26eV by Canfield *et.al* [100], (3)27-88eV by Hagemann *et.al* [101], and (4) above 88eV by Nilson and Zombeck *et.al* [102, 103]. After the subtraction of ε_i^{Drude} , ε_i^{IB} is shown in Fig. 4.6. When upper limit of the Kramers-Kronig integration in Eq. 4.8 is defined as 10keV, ε_r^{IB} is 6.38 ± 0.19 at 1.55eV.

The real part of free electron contribution ε_r^{Drude} is then separated from the measured dielectric constant, by subtracting the contribution from atomic polarizability (4.3 ± 1.1) and the interband portion (6.38 ± 0.19). No correction to the imaginary part is needed. At room temperature, ε^{Drude} is $-(33.1 \pm 2.8) + i(1.26 \pm 0.10)$. The corresponding n_e becomes $5.96 \pm 0.5 \times 10^{22} / \text{cm}^3$, which agrees well with the known value of $5.9 \times 10^{22} / \text{cm}^3$.

At excited states, the same correction factors may be used since the maximum electron temperature is only $\sim 3\text{eV}$ at 4MJ/kg, which will be shown in

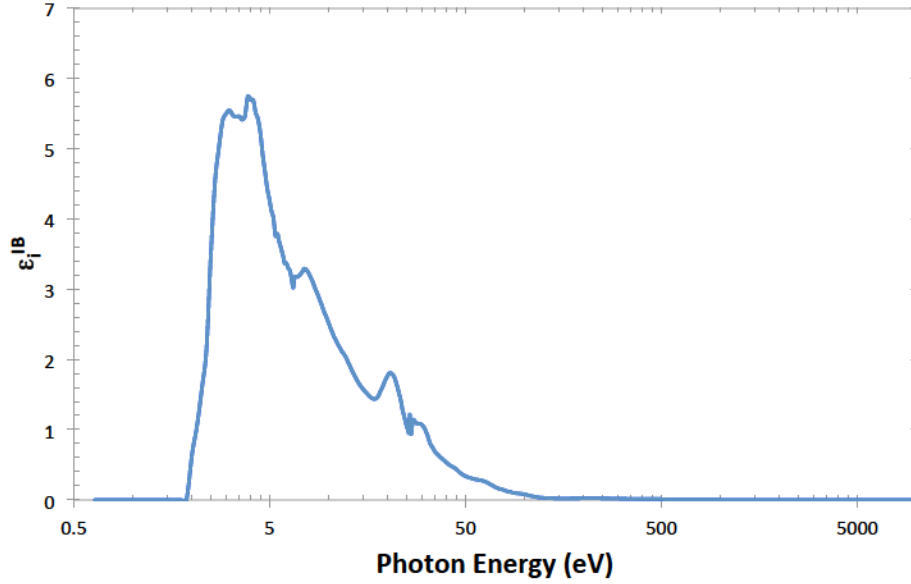


Figure 4.6: ε_i^{IB} by subtracting ε_i with ε_i^{Drude}

the next chapter. As a supporting factor, less than 20% of ε_r^{IB} is contributed by ε_i^{IB} below 3eV according to Eq. 4.8, which is found by varying the upper limit of the integration as show in Fig. 4.7. So that we may use the same ε_r^{IB} obtained from room temperature through our range of calculations up to about 4MJ/kg.

The corresponding time evolution of n_e and τ at different excitation energy densities are shown in Fig.4.8. In general, a significant increase of n_e occurs right after the excitation, while τ decreases by almost an order of magnitude at the same time. These phenomena are the results of the rapid increase of electron temperature T_e due to laser heating. After the initial laser heating, in the next several picoseconds both n_e and τ only change gradually because the energy transfer from electrons to the lattice is relatively slow. Such process will be discussed in detail in the next chapter when I discuss the electron-ion coupling factor g_{ei} . Interestingly, for $\Delta E > 1\text{MJ/kg}$, n_e first decreases after the initial increase due to excitation but rises again at a later time. This is somewhat counter-intuitive because n_e should increase with T_e . One possibility is that with the rise in lattice temperature, the ions become more disordered

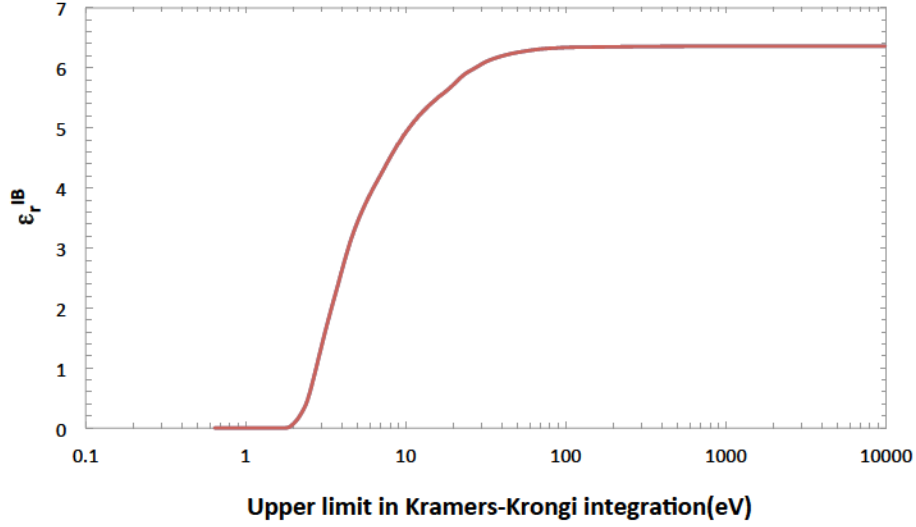


Figure 4.7: ϵ_r^{IB} as a function of upper limit in the Kramers-Kronig integration according to Eq. 4.8

and move somewhat from their original positions even before disassembly [28], which could effect the atomic polarizability α_a , and the interband contribution ϵ^{IB} may vary somewhat at the same time [21]. The change of these two parameters can affect the interpretation of n_e . Due to the lack of quantitative understanding of the evolution of such parameters, our main focus is placed at the initial value of n_e and τ right after laser excitation as a function of excitation energy density.

The initial values of n_e and τ are defined at 540fs after the arrival of the pump laser pulse, which is chosen to be the resolution of our chirped pulse probe. At this time, the electrons are expected to be thermalized [9], while the lattice remains cold [59]. The initial values of n_e and τ as a function of excitation energy densities are shown in Fig. 4.9. Obviously, the initial value of n_e increases as a function of ΔE or T_e , while τ decreases. To know the relation between these two parameters as a function of T_e at non-equilibrium warm dense gold, one needs to know how T_e increases with the excitation energy density. This will be discussed in the next chapter where a proper electron heat

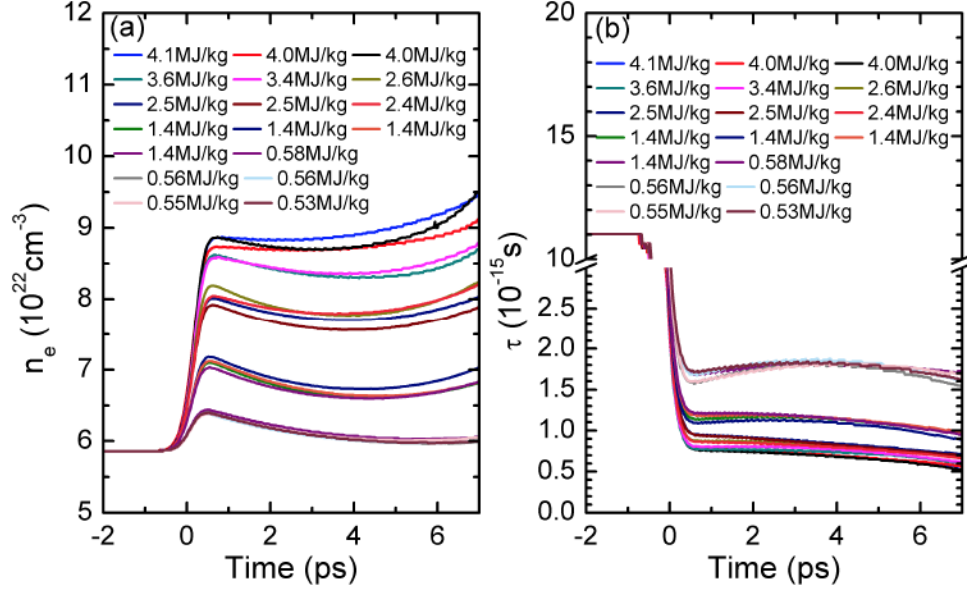


Figure 4.8: Time evolved n_e and τ at different excitation energy densities. The labels indicate the energy densities at which the measurements were done individually. Some labels of a same energy density were taken from different shots at a same excitation energy density.

capacity C_e is given. For now, we can attempt to interpret the upper limit for uniform excitation from Chapter 3 using the energy density dependent of n_e .

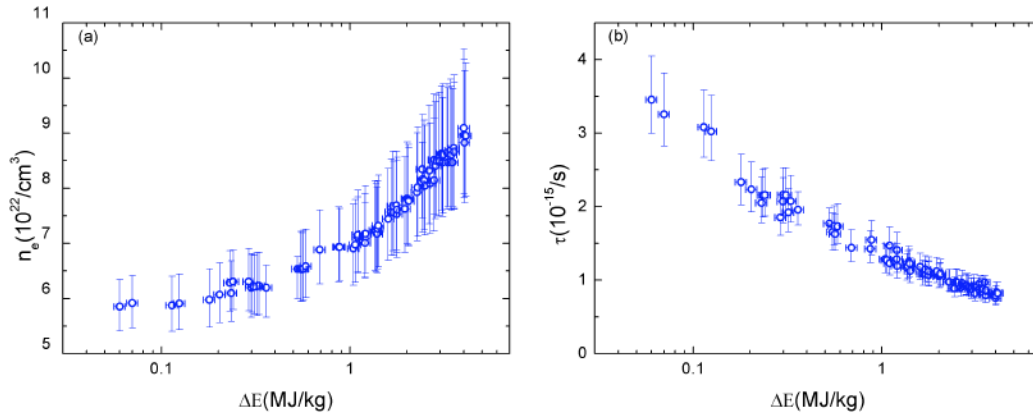


Figure 4.9: Initial values of n_e and τ at different excitation energy density.

4.4 Interpretation of The upper Limit of Uniform Heating

As one may remember the measurement of reflectivities of the probe pulses from the front and rear surfaces, above an excitation energy density of 5MJ/kg, or equivalently above a peak absorbed laser intensity of $\sim 6.4 \times 10^{12} W/cm^2$, significant discrepancy of the front and rear reflectivities is observed. Equally interestingly, according to Fig. 3.21, the initial change of reflectivity from the rear side (ΔR_R) remains essentially constant beyond the critical energy flux. The data suggest that the ballistic electron transport reached a saturation. A possible limiting process may come from the maximum energy flux that those ballistic electrons can carry.

4.4.1 Flux Limited Ballistic Electron Energy Transportation

In the early studies of non-local energy transport of hot electrons, the power flux of free streaming electron energy transportation in a planar target has a general form [55],

$$Q_{HE} = \frac{1}{2} m_e n_h \int_{-\infty}^{\infty} v^2 f(v) dv = \frac{1}{2} F n_h m_e v_h^3 \quad (4.9)$$

where $f(v)$ is the distribution function of the free streaming electrons, on which the flux limiting factor F depends, n_h is the hot electron density, and v_h is the average hot electron velocity. For a Maxwellian distribution plasma, F is taken to be 0.6. In reality, with a steep density and temperature gradient, the electron distribution can be far from Maxwellian, and F is found to be only about 0.06, which needs to be determined by kinetic theory calculations [104, 105, 106].

In our case of non-thermal ballistic electron transport, a similar model may

be used. Within the life time of the ballistic electrons, they can be considered as “hot electrons”, which travels near the Fermi velocity v_F . Since our pump pulse duration is only 45fs, which is significantly shorter the ballistic electron life time of about 100fs [13], before electron thermalization, the ballistic electrons excited from $5d$ band should populate the conduction band mostly between Fermi level and 0.7eV above it as discussed in Section 3.2, which corresponds to an energy range between 5.5eV and 6.2eV in gold. The corresponding distribution function $f(v)$ is non-zero only when electron energy ϵ is in this range. Because the electron velocity $v = \sqrt{\frac{2\epsilon}{m_e}}$, the ballistic electron velocity is in a range within 6% variation and thus it can be assumed to be a constant. Thus the flux limiting factor F can be considered to be 1 by assuming all ballistic electrons have the same velocity. n_h is considered to be the conduction electron density n_e , which can be obtained from our measurement from Fig. 4.9(a). Eq.4.9 can then be modified accordingly for the non-thermal (NT) ballistic electrons,

$$Q_{NT} = \frac{1}{2}n_e m_e v_F^3 \quad (4.10)$$

The theoretical value of v_F is $1.4 \times 10^6 m/s$, and the measured value is around $1 \times 10^6 m/s$ [74, 76, 13, 73]. Here we assume $v_F = 1.2 \times 10^6 m/s$. As a function of energy density, the maximum energy flux that can be carried by the ballistic electrons is shown in Fig. 4.10. As a comparison, the absorbed laser flux Q_L as a function of energy density is also shown in the same figure. As can be seen, Q_L has a larger slope than that of Q_{NT} , and at $\Delta E_D = 5MJ/kg$, $Q_L = Q_{NT}$, which can be interpreted as the maximum absorbed laser flux that the ballistic electrons can carry. Another plot of Q_L/Q_{NT} is shown in Fig. 4.11. In this plot, it can be seen that $Q_L/Q_{NT} = 1$ at around 5MJ/kg, or $\sim 6.4 \times 10^{12} W/cm^2$, which is approximately the same point where R_F starts to deviate from R_R significantly from the measurement.

The hypothesis of flux limitation suggests that when the absorbed energy flux is above the maximum energy flux that the ballistic electrons can carry, a

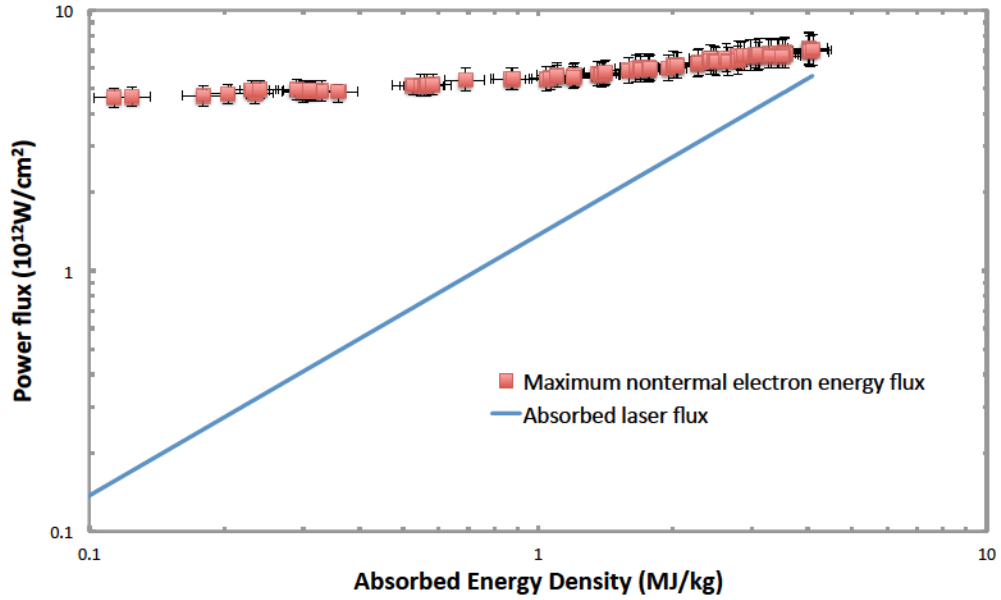


Figure 4.10: Maximum energy flux that can be carried by non-thermal ballistic electrons (Q_{NT}) and absorbed laser flux (Q_L) as a function of energy density

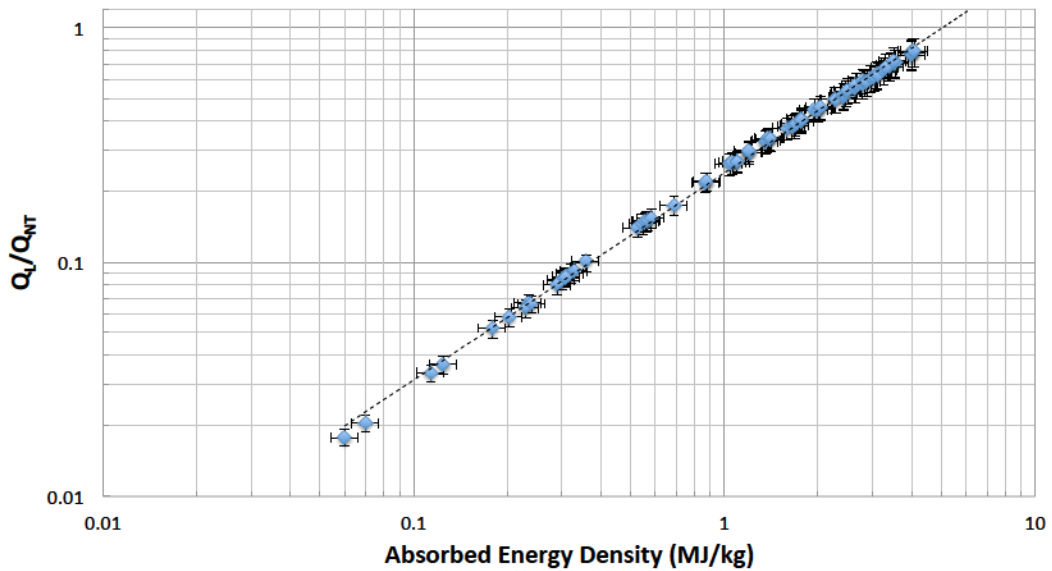


Figure 4.11: The ratio of Q_L over Q_{NT} as a function of absorbed laser flux. The dashed line is for eye guiding

thermal gradient is formed even for a foil thinner than the range of the ballistic electrons.

4.5 Summary

The time resolved probe pulse reflectivity and transmissivity of two temperature warm dense thin gold were measured. The corresponding AC conductivity was extracted. It is clear that the evolution of AC conductivity is dictated by two processes. Shortly after laser excitation, the increase of electron temperature led to a shapely change of AC conductivity, while the gradual change in conductivity afterward was resulted from the electron-ion energy coupling. The electron density in warm dense gold shortly after laser excitation was deduced using Drude theory. A possible reason for the upper limit of uniform excitation in the free standing gold thin foil was also given according to the electron density.

Chapter 5

Comparison with First Principles Calculation

In the previous chapter, the measurement of AC conductivity in warm dense gold is described and discussed. These data provide a good opportunity to benchmark first principles (*ab-initio*) warm dense matter simulations. This two temperature warm dense gold simulation was carried out by our colleagues from Commissariat à l'énergie atomique (CEA) in France. Here I will briefly describe the method they used in their simulations and then compare our experimental results to their simulation results

5.1 Theoretical calculations

In a femtosecond laser excited material, as described in the previous chapters, the electron temperature T_e is initially significantly higher than that of the ions T_i because the electron ion coupling time is in the order of picosecond to tens of picosecond. Therefore, it is necessary to consider electrons and ions separately. The temperatures of these two system, as mentioned in Chapter 2, can be described by two coupled equations: Eq.2.24 for T_e , and Eq.2.25 for T_i . As indicated in Chapter 3, when absorbed energy density is below 5MJ/kg, the

electron temperature can be expected to be uniform distributed in a 30nm thick gold thin foil, shortly after the laser pulse. For this case, we may simplified the two temperature model (TTM) equations by dropping the thermal diffusion term,

$$C_e \frac{\partial T_e}{\partial t} = -g_{ei}(T_e - T_i) + S(t) \quad (5.1a)$$

$$C_i \frac{\partial T_i}{\partial t} = g_{ei}(T_e - T_i) \quad (5.1b)$$

where $S(t)$ is the energy density deposition rate, which is just the rate of absorbed energy density (ΔE_D in MJ/kg) as a function of time. ΔE_D can be measured by taking the incident energy and subtracting the reflection and transmission portions as described in Chap.4. Here we assume that $S(t)$ is proportional to the laser intensity, which is approximately true for our case, because the laser absorption was about $48 \pm 5\%$ for excitation energy below 5MJ/kg through out the experiment. For a laser pulse of Gaussian shape in time, the energy deposition is given by

$$S(t) = \frac{\Delta E_D \rho_{Au}}{\tau_P \sqrt{\pi}} \exp\left[-\left(\frac{t - t_0}{\tau_P}\right)^2\right] \quad (5.2)$$

where ρ_{Au} is the density of gold in room condition ($1.93 \times 10^4 \text{ kg/m}^3$), $\tau_P = \frac{\tau_{1/2}}{2\sqrt{\ln 2}}$ with the FWHM of the laser pulse $\tau_{1/2}$, and t_0 is the time for the peak intensity.

In order to solve the TTM equations, what we need to get from the theoretical calculation are the electron heat capacity C_e , ion heat capacity C_i , and the electron-ion coupling factor g_{ei} . The early study of linear response of phonon from first principles calculation suggests that C_i does not change significantly with T_i [107]. In equilibrium measurements, C_i increased by about 5% when the temperature increased from 300K to 1300K [108]. Here we use $C_i = 2.5 \times 10^6 \text{ J/m}^3/\text{K}$ for gold, which follows the upper limit of Dulong-Petit

law [109, 34]. C_e and g_{ei} were calculated as a function of T_e in the following discussion.

Our first principles calculation was carried out with a plane wave code package called ABINIT [110] with parallel implementation [111]. This package solves the many body problem in the form of effective single particle Kohn-Sham Schrödinger equation with density functional theory (DFT) [112, 113],

$$\left(-\frac{\nabla^2}{2} + \nu_{eff}(x)\right)\phi_i(x) = \epsilon_i\phi_i(x) \quad (5.3)$$

where $\nu_{eff}(x)$ is the Kohn-Sham potential, $\phi_i(x)$ is the eigenstate of the i th orbital and ϵ_i is the corresponding orbital energy. $\nu_{eff}(x)$ consists of external potential ν_{ext} , Coulomb potential, or usually called Hartree potential ν_H , and the exchange-correlation potential ν_{xc} . Since the functionals for exchange and correlation are not known exactly, local density approximation (LDA) is applied. In order to improve the computational efficiency, a projector augmented wave (PAW) method [114, 115] is used to transform the fast oscillating wave functions into smooth ones.

The behaviours of the non-equilibrium electron and lattice systems with finite temperature are described by molecular dynamic (MD) simulation, which allows the ion temperature to be different from the electron temperature. T_e and T_i in the simulation are taken from the TTM calculation.

5.1.1 Calculation of Electron Heat Capacity C_e

In order to know how the electrons evolve with absorbed laser energy, the knowledge of electron heat capacity (C_e) becomes the first priority. As the standard definition of C_e [34], it is the temperature derivative of the electron system's internal energy at a constant volume,

$$C_e(T_e) = \left(\frac{\partial U}{\partial T_e}\right)_V \quad (5.4)$$

where U is the electron internal energy, which can be obtained from the electron density of states (EDOS) calculated using DFT with the corresponding Fermi distribution. The internal energy at each T_e is define as [34],

$$U_e(T_e) = \int_{-\infty}^{\infty} g(\epsilon, T_e) f(\epsilon, \mu(T_e), T_e) \epsilon d\epsilon \quad (5.5)$$

where $g(\epsilon, T_e)$ is the EDOS calculated from DFT at temperature T_e , $f(\epsilon, T_e)$ is the Fermi distribution (Eq.2.7). The chemical potential $\mu(T_e)$ is obtained at each T_e according to the conservation of total electron number that,

$$N = \int_{-\infty}^{\infty} g(\epsilon, T_e) f(\epsilon, \mu(T_e), T_e) d\epsilon = \int_{-\infty}^{\infty} g(\epsilon, 0) f(\epsilon, \epsilon_F, 0) d\epsilon \quad (5.6)$$

where $\epsilon_F=5.5\text{eV}$ is the Fermi energy in gold, which equals to the chemical potential at $T_e=0\text{K}$. Our calculation of C_e as a function of T_e is shown in Fig.5.1. We can see that our calculation of C_e is similar to the early work by Lin *et.al* [14]. In their study, the EDOS was only calculated at 0K, which resulted in the difference observed in Fig. 5.1. The free electron gas model (FEG) follows the parameters from standard textbook values (see Eq.2.26) [34]. Here we use the conduction electron density $n_e=5.9\times 10^{22}\text{cm}^{-3}$ the same as in room condition for all T_e , since the detailed evolution of n_e as a function of T_e is not well studied, especially in non-equilibrium condition. As can be seen from Fig. 5.1, significant difference is observed between FEG model and our calculation above 1/2eV.

Using C_e from different models, one can estimate the maximum T_e that can be obtained as a function of excitation energy density. Such an estimation can be carried out by simply removing the electron-ion coupling term from Eq.5.1(a), since the electrons in gold are expected to be thermalized at about 120fs after the pump pulse according to Fermi liquid theory calculation [9], and only a small amount of absorbed laser energy is transferred to the ions within a picosecond [59]. The comparison of maximum T_e between C_e from our

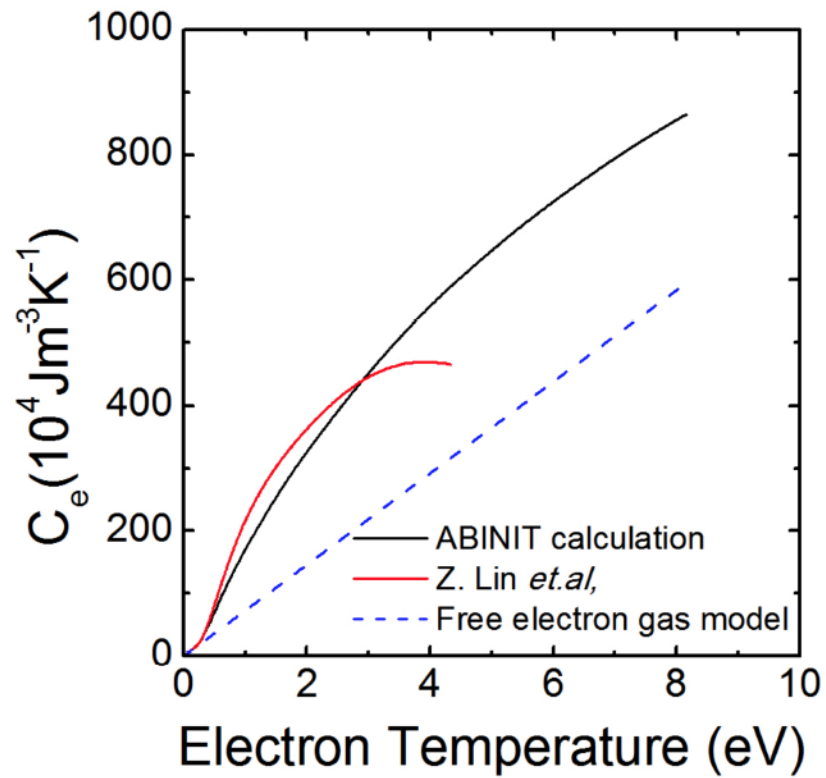


Figure 5.1: Our calculation of electron heat capacity C_e from ABINIT. As comparison, C_e calculated from previous calculation by Lin.*et.al* [14], and free electron gas model (FEG) [34] are shown on the same figure.

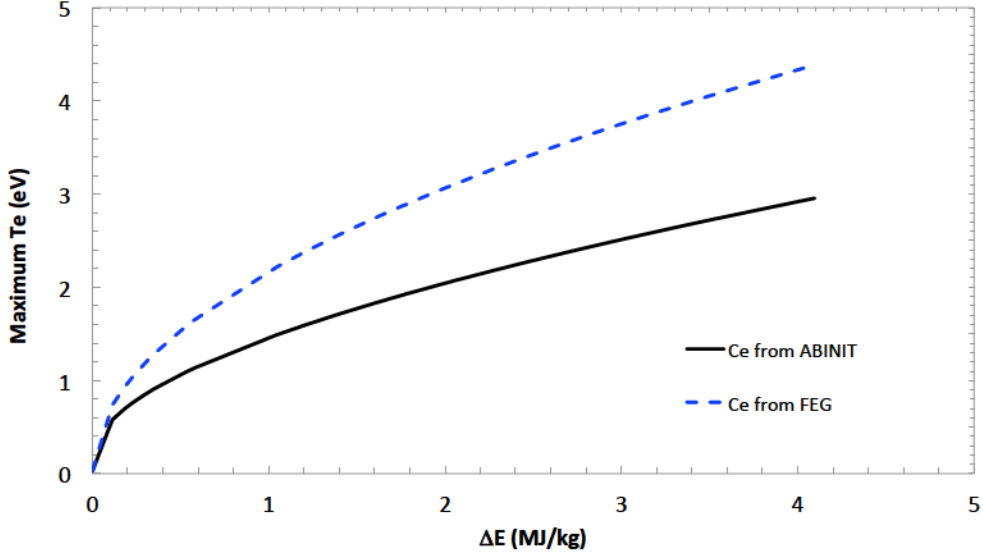


Figure 5.2: Maximum electron temperature right after electron thermalization as a function of energy density, which are calculated from two different C_e .

calculation and that from FEG is shown in Fig.5.2. Due to lower C_e in FEG, the corresponding T_e is significantly higher.

5.1.2 Calculation of Electron-ion Coupling factor g_{ei}

Since we have to solve both equations from TTM, the understanding of electron-ion coupling factor g_{ei} is necessary. The original definition of g_{ei} is the coefficient for energy transfer between electron and ion, which is proportional to the difference between T_e and T_i [53],

$$\left. \frac{\partial E}{\partial t} \right|_{ei} = g_{ei} \times (T_i - T_e) \quad (5.7)$$

In the previous studies to extract g_{ei} , experiments were carried with laser fluence around or below damage threshold [116, 13, 117] (about $0.12\text{J}/\text{cm}^2$ for gold at 400nm) using femtosecond laser pulses, and the value for gold was found to be approximately constant. Using our calculated C_e , maximum T_e is about 0.8eV at damage threshold of gold irradiated by 400nm femtosecond

laser pulse. No experimental data for g_{ei} is available at higher laser fluence condition. In first principles calculation [14], g_{ei} stays almost constant when T_e is less than 0.3eV, but changes significantly at higher T_e . Here we follow the method suggested by Lin. *et.al* [14] with more a detailed calculation using ABINIT.

Following the theory of electron ion energy coupling suggested by Allen [118], the electron-ion energy transfer rate in solid is,

$$\left. \frac{\partial E}{\partial t} \right|_{ei} = (4\pi/\hbar) \sum_{k,k'} \hbar\omega_Q |M_{kk'}|^2 S(k, k') \delta(\epsilon_k - \epsilon_{k'} + \hbar\omega_Q) \quad (5.8)$$

where k, k' denotes the number of quantum states of the electrons with ϵ_k and ϵ'_k for the corresponding energy, while Q is that for the phonon with energy $\hbar\omega_Q$, $M_{kk'}$ is the electron-phonon scatter matrix element, which represents the probability of a scatter process for an electron with initial and final states of k and k' , $S(k, k')$ is the thermal factor for the corresponding phonon absorption and emission processes due to electron scattering, whose expression is,

$$S(k, k') = [f(\epsilon_k) - f(\epsilon_{k'})]n(\omega_Q) - f(\epsilon_{k'})[1 - f(\epsilon_k)] \quad (5.9)$$

where f denotes the Fermi-Dirac distribution for electrons, i.e. $f(\epsilon_k) = \frac{1}{\exp[(\epsilon_k - \mu)/k_B T_e] + 1}$, and n is the Bose-Einstein distribution of the phonons, i.e., $n(\omega_Q) = \frac{1}{\exp(\hbar\omega_Q/k_B T_e) - 1}$.

The probability of an electron from initial state k making a transition to a final state k' after scattering with a phonon at state Q , $\hbar\omega_Q |M_{kk'}|^2$, is related to the electron-phonon spectral function $\alpha^2 F(\epsilon, \epsilon', \Omega)$, where α^2 is the electron-phonon coupling strength, while $F(\epsilon, \epsilon', \Omega)$ is the phonon density of states. It has the form that [118],

$$\alpha^2 F(\epsilon, \epsilon', \Omega) = [2/\hbar g(\epsilon_F)] \sum_{k,k'} \hbar\omega_Q |M_{kk'}|^2 \delta(\epsilon_k - \epsilon) \delta(\epsilon_{k'} - \epsilon') \delta(\omega_Q - \Omega) \quad (5.10)$$

Although $\alpha^2 F(\epsilon, \epsilon', \Omega)$ depends on both the initial (ϵ) and final (ϵ') electrons energy states, those electrons are usually near Fermi level with a few eV, while the phonon frequency Ω in THz regime corresponds to only a few meV energy. It was suggested by Wang *et.al* [119] that an approximation can be used so that $\alpha^2 F(\epsilon, \epsilon', \Omega) \approx \frac{g(\epsilon)g(\epsilon')}{g^2(\epsilon_F)} \alpha^2 F(\epsilon_F, \epsilon_F, \Omega) = \frac{g(\epsilon)g(\epsilon')}{g^2(\epsilon_F)} \alpha^2 F(\Omega)$, based on the assumption that the magnitude of $M_{kk'}$ is independent of k and k' . Here $g(\epsilon)$ is the electron distribution function for electron energy at ϵ .

To substitute Eq.5.10 back into Eq.5.8, we need to multiply Eq.5.8 by 3 factors of 1 for the integrations over Delta functions, i.e. $\int_0^\infty d\epsilon \delta(\epsilon_k - \epsilon)$, $\int_{-\infty}^\infty d\epsilon' \delta(\epsilon'_k - \epsilon')$ and $\int_{-\infty}^\infty d\Omega \delta(\omega_Q - \Omega)$. Using the relation that $\epsilon, \epsilon' \gg \hbar\Omega$, substitute Eq.5.9 and 5.10 into Eq. 5.8, we can get,

$$g_{ei}(T_e) = \frac{2\pi}{g(\epsilon_F)(T_i - T_e)} \int_0^\infty d\Omega \int_{-\infty}^\infty d\epsilon \times \alpha^2 F(\Omega) (\hbar\Omega)^2 [n(\hbar\Omega, T_i) - n(\hbar\Omega, T_e)] g^2(\epsilon) \left(-\frac{df}{d\epsilon}\right) \quad (5.11)$$

It seems like that the above equation depends on both T_e and T_i , but if we use the fact that $T_e \gg T_i$ right after the pump pulse, $\frac{n(\hbar\Omega, T_i) - n(\hbar\Omega, T_e)}{T_i - T_e} \approx \frac{n(\hbar\Omega, T_e)}{T_e} \approx \frac{k_B}{\hbar\Omega}$. The second approximation is based on the elimination of high order terms in Taylor expansion, which is legitimate when $k_B T_e \gg \hbar\Omega$. At a later time when T_i starts to increase, we also have the condition that $T_i \gg \hbar\Omega$, which leads to the same result that T_i can be eliminated. The final form of g_{ei} can be written as,

$$g_{ei}(T_e) = \frac{2\pi \hbar k_B}{g(\epsilon_F)} \int_0^\infty d\Omega \int_{-\infty}^\infty d\epsilon \times \alpha^2 F(\Omega) \Omega g^2(\epsilon) \left(-\frac{df}{d\epsilon}\right) \quad (5.12)$$

To carry out the above integration, we already have the electron DOS $g(\epsilon)$ and Fermi distribution f as a function of T_e when the calculation of C_e was carried out (see Eq.5.5 and 5.6). The electron-phonon spectral function $\alpha^2 F(\Omega)$ was carried out in ABINIT through linear response density functional pertur-

bation theory [107]. The integration of $\alpha^2 F(\Omega)$ gives the second moment of the phonon spectrum $\langle \omega^2 \rangle$ [120, 117],

$$\lambda \langle \omega^2 \rangle = 2 \int_0^\infty \alpha^2 F(\Omega) \Omega d\Omega \quad (5.13)$$

where λ is called the electron-phonon coupling constant. The left side of the above equation was measured near room temperature to be $23 \pm 4 meV^2$ [117], while our calculated $\alpha^2 F(\Omega)$ integrated to $21 \pm 2 meV^2$, which are in close agreement. It also worthy to mention that $\alpha^2 F(\Omega)$ is non-zero only below 5THz, which simplifies the above integration to a finite upper limit.

The result of our calculated g_{ei} is shown in Fig.5.3. Obviously, It increases significantly as a function of T_e , which is in reasonable agreement with that reported in Lin's work [14]. The difference observed in Fig. 5.3 is mostly caused by our use of T_e dependent EDOS $g(\epsilon, T_e)$, which is discussed in the calculation of $C_e(T_e)$. At low T_e , both calculated values agree well to the measured value ($2.2 \pm 0.3 \times 10^{16} W/m^3/K$) by Hohlfeld *et.al* [13], which is also shown in the figure. That experimental value was extracted within 0.3MJ/kg, and the maximum T_e is below 0.85eV.

We now have all the required parameters to solve the TTM equations. The ion temperature shortly after pump pulse excitation (540fs), and at 6ps after the pump pulse is shown in Fig.5.4 as a function of excitation energy density. Here the $C_e(T_e)$ from our calculation is used. Surprisingly, for 3MJ/kg and above, T_i is already well above the room condition melting point 1337K at 540fs after the pump pulse. Note that above the melting point, the ions should absorb some extra energy, which is called latent heat, before lattice disassembly. In gold, it is about $1.22 \times 10^9 J/m^3$ [121], or 502K equivalent in T_i at solid density. However, in the early measurement of warm dense gold disassembly [16], it takes about $6.3 \pm 0.7 ps$ before hydrodynamic expansion occurs at 4.3MJ/kg. Before the disassembly, it was also found that band structure still exists, indicating it is still in solid state form from broadband dielectric function measurements

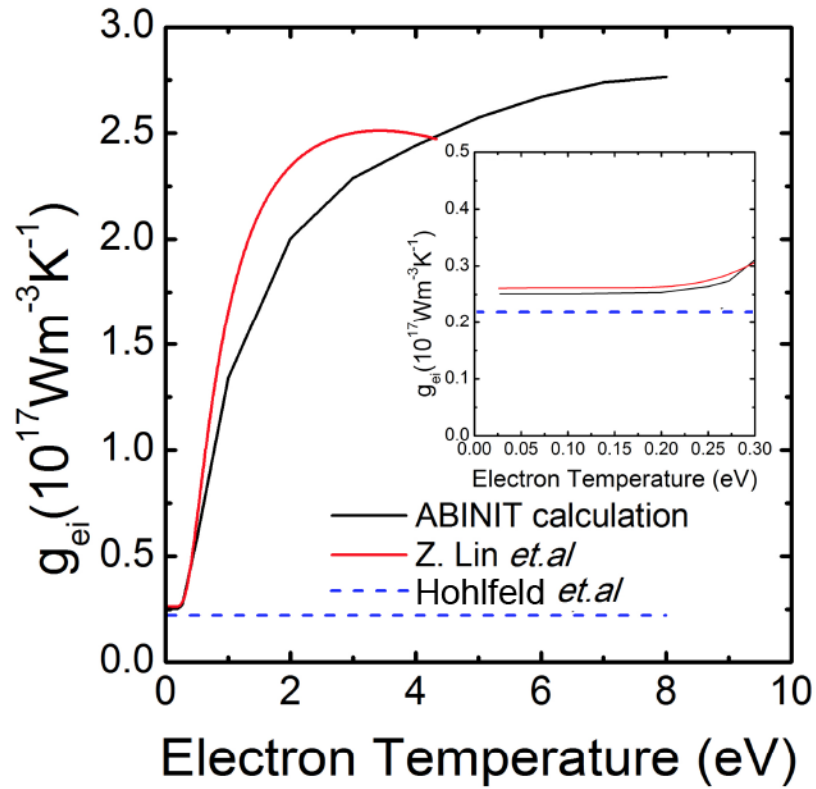


Figure 5.3: Our calculation of electron-ion energy coupling factor g_{ei} from ABINIT. As comparison, g_{ei} calculated from previous calculation by Z. Lin *et.al* [14], and the measurement by J. Hohlfeld *et.al* [13] at no more than 0.85eV are shown on the same figure. Inset is the magnified plot below 0.3eV, which shows little change of g_{ei} with temperature in calculation.

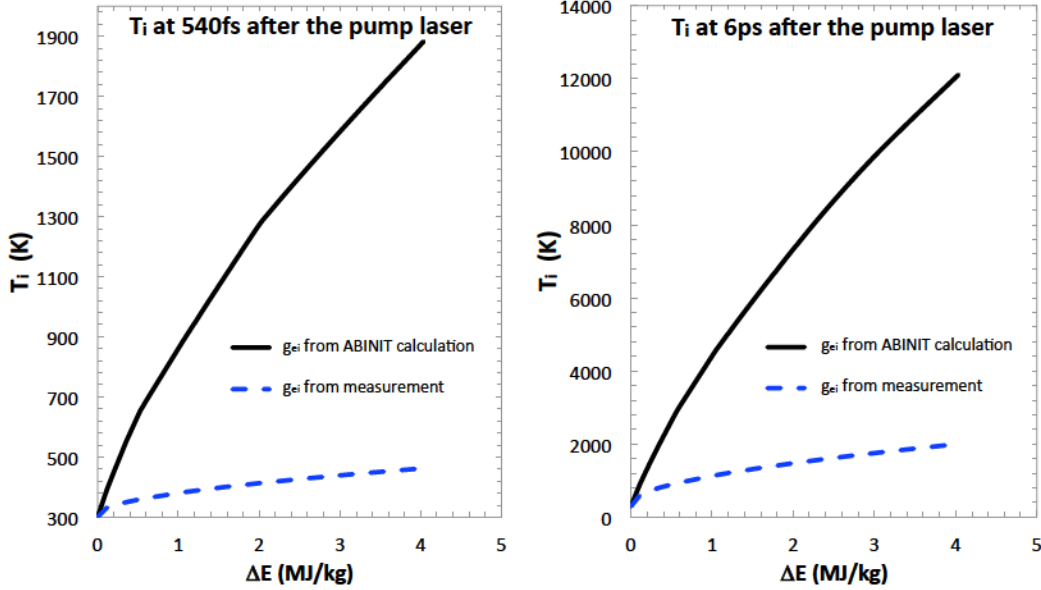


Figure 5.4: TTM calculated Ion temperature at 540fs and 6ps after the peak of pump laser with g_{ei} from ABINIT calculation, and from J.Hohlfeld *et.al*'s measurement [13]. Here C_e is from ABINIT calculation.

[21]. At 6ps after the pump pulse, T_i reaches above 1eV at 4MJ/kg (See Fig. 5.4) using ABINIT calculated g_{ei} in the TTM calculations. With such a high T_i , it is unlikely that the material remains solid in contradiction to the experimental observations. For comparison, the results of TTM calculation using $g_{ei} = 2.2 \times 10^{16} \text{W/m}^3/\text{K}$ are also shown in the Fig. 5.4 as dashed line. We can see that at 6ps, T_i only reaches 2000K at 4MJ/kg, which appears to be qualitatively agree better with the disassembly measurement.

5.1.3 AC Conductivity Calculation

In order to compared with our experimental AC conductivity measurement, we also need to calculate the conductivity. Here we applied the Kubo-Greenwood formula [122, 123, 124], which can extract the the real part of AC conductivity from wavefunctions. For a specific \mathbf{k} point in the Brillouin zone, the conductivity as a function of frequency ω can be written as,

$$\sigma_{\mathbf{k}} = \frac{2\pi e^2 \hbar^2}{3m^2 \omega V} \sum_{i=1}^N \sum_{j=1}^N \sum_{\alpha=1}^3 [F(\epsilon_{i,\mathbf{k}}) - F(\epsilon_{j,\mathbf{k}})] \times |\langle \Psi_j | \nabla_{\alpha} | \Psi_i \rangle|^2 \delta(\epsilon_{j,\mathbf{k}} - \epsilon_{i,\mathbf{k}} - \hbar\omega) \quad (5.14)$$

where i and j are the numbers of Kohn-Sham orbitals, which are summed over N ; α represents the spatial directions within a simulation box of volume V ; $F(\epsilon_i)$ is the weighting factor of energy ϵ_i according to Fermi distribution; Ψ_i and Ψ_j are the wavefunctions for the i th and j th orbitals. The \mathbf{k} points are selected using a $4 \times 4 \times 4$ Monkhorst-Pack sampling grid [125] within the Brillouin zone. The overall conductivity is obtained by integration over those \mathbf{k} points [94],

$$\sigma_r = \sum_{\mathbf{k}} \sigma_{\mathbf{k}} W(\mathbf{k}) \quad (5.15)$$

where W is the weight factor for point \mathbf{k} . To get the parameters for σ_r calculation, precise ion positions need to be known for carrying out DFT calculation using ABINIT. The ion motions are calculated from molecular dynamics (MD) calculation with 108 atoms in the simulation box. At each time step, snapshots of ion positions were taken to carry out DFT calculation for the electron system, where parameters for Eq.5.14 and 5.15 are extracted. In such a combined DFT-MD method, electron and ion systems are characterized by their time dependent temperature calculated from TTM.

The imaginary part of AC conductivity σ_i can then be calculated from σ_r ,

$$\sigma_i(\omega) = -\frac{2\omega}{\pi} \mathcal{P} \int_0^{\infty} \frac{\sigma_r(\omega')}{\omega'^2 - \omega^2} d\omega' \quad (5.16)$$

where \mathcal{P} denotes the principle value integration. In such calculation it requires the knowledge of σ_r from zero to infinity. The real part of the AC conductivity in gold (σ_r) at room temperature was calculated by DFT-MD, and the corresponding deduced imaginary part σ_i using Eq.5.16 is shown in

Fig.5.5 [17]. As can be seen that the calculated σ_r has a similar shape as the experimental result, but the calculated data deviated significantly at low photon energy, and also a shift in the rising edge of the $5d$ band. There are two major reasons for such discrepancy. Firstly, we only used 108 atoms in the simulation, which limits the minimum energy steps in the Kohn-Sham orbitals to be 0.1eV. The number of atoms also limits the accuracy of the eigen energies of each orbital, in particular near the DC limit [126, 127]. Secondly, the used of local density approximation (LDA) for exchange and correlation energy functional will also introduce inaccuracy [17]. For gold, it may be better to use hybrid Heyd-Scuseria-Ernzerhof (HSE) functional [128]. However improvement to either of the limitations requires significant more computational resources.

When compared the data at 1.55eV, where our measurements were done. The real part of the calculated conductivity at room temperature agrees well with the experimental data. For σ_i , however, the accumulated error from Kramers-Kronig integration leads to significant disagreement between calculation and experimental results. We expect similar issue exist in the warm dense matter regime.

5.2 Comparison between Experimental Result and Simulation Result

Our measurement of temporal evolution of AC conductivity gives two different benchmarks for the first principles calculations. The initial data shortly after the excitation at 540fs can be used to benchmark the electron heat capacity C_e model, since essentially all laser energies store in the electron system while the change of ion temperature is expected to be small and they remain near room temperature. The evolution of AC conductivity from the initial 540fs to 6.5ps after the laser heating provides the test to the electron ion coupling factor g_{ei} .

For testing C_e models, the experimental data is taken at 540fs after the peak

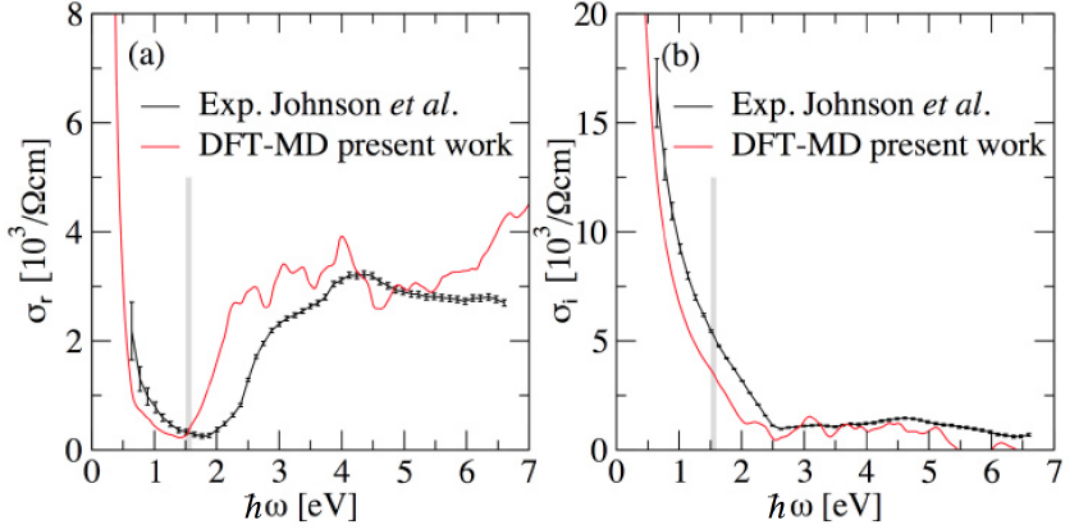


Figure 5.5: (a) σ_r from our ABINIT calculation and (b) the corresponding σ_i from Kramers-Kronig relation, compared to the experimental data measured by Johnson and Christy [48]

of pump pulse due to temporal resolution limit of the chirped pulse measurement. In the theoretical calculation, we assume that all the energy is stored in the electron system, while the ions remains at 300K. As a result, electron temperature only depends on C_e , where, $C_e T_e = \rho_{Au} \Delta E_D$. We used C_e from our ABINIT calculation, and from FEG model. The comparison for both σ_r and σ_i is shown in Fig.5.6.

For σ_r , it is clear that the ABINIT calculated C_e leads to a significantly better agreement with the experimental data. For σ_i , inherent from the large amount of inaccuracy in the calculation at room temperature, for low excitation energy density below 1MJ/kg, the experimental data agrees poorly with calculations. Above 1MJ/kg, the discrepancy reduces significantly, and the experimental data falls between the calculated values with two different C_e . As the energy density continues to increase, the experimental data tends to be closer to that calculated with our C_e , while the calculation with FEG C_e becomes significantly larger. However, due to the larger uncertainty in σ_i , this may be a fortuitous result.

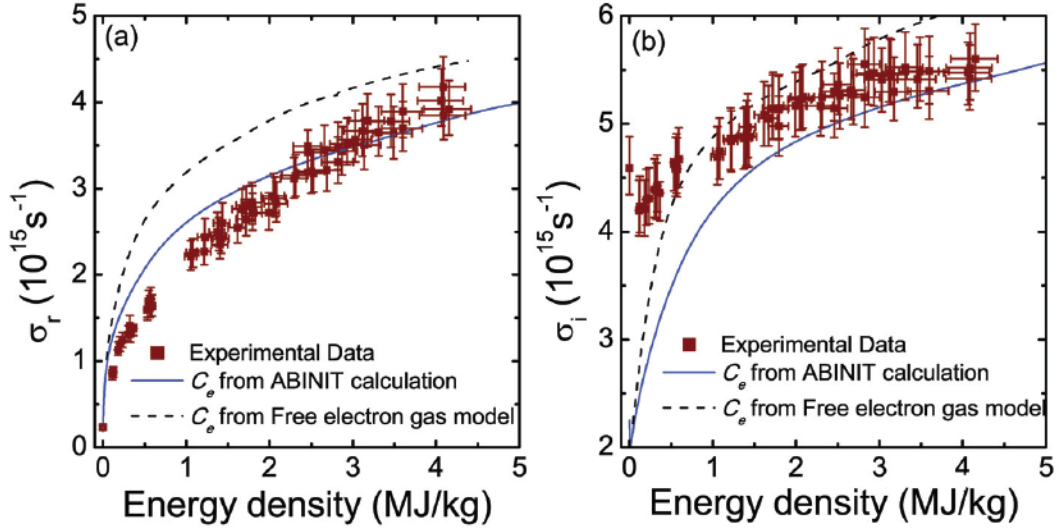


Figure 5.6: Comparison between experimental data and simulation of initial value of (a) real and (b) imaginary parts of AC conductivity at 540fs after pump laser heating.

For testing g_{ei} models, we first solve the TTM equations at different times, and use the corresponding T_e and T_i to calculate σ_r and σ_i . Here we use both g_{ei} from our calculation, and the one measured at low energy density [13]. The comparisons at 4 different energy densities are shown in Fig.5.7.

We can see that except at low ΔE_D around 0.5MJ/kg, the calculated σ_r values with ABINIT calculated g_{ei} increase more rapidly than the experimental data. When a constant $g_{ei}=2.2 \times 10^{16}W/m^3/K$ is used, it leads to a much better agreement with the experimental data. At $\sim 1.5MJ/kg$ and $\sim 0.55MJ/kg$, the small discrepancy of σ_r between experimental and calculated data right after excitation (see Fig. 5.6) appears to propagate as time evolves, but the trends are still in good agreement. There is only a small difference between the two calculated σ_r near 0.55MJ/kg, which is due to the small change of g_{ei} under relatively low T_e condition as shown in Fig.5.3. Not surprisingly the calculated and experimental σ_i values do not show agreement. From the above comparisons, it suggests that the constant value of g_{ei} actually works better than those calculated by ABINIT.

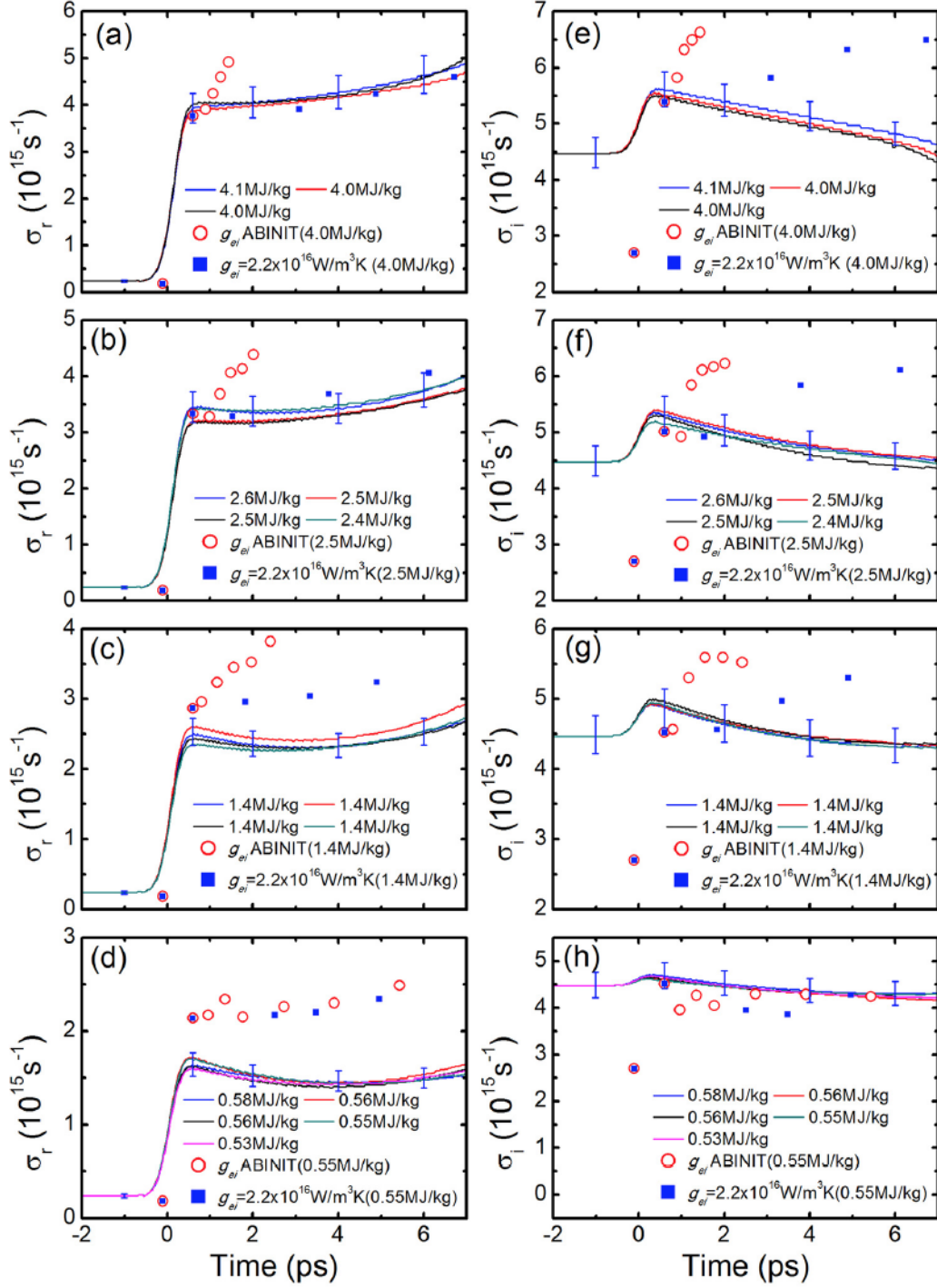


Figure 5.7: Evolution of (a-d) real and (e-h) imaginary parts of AC conductivity for four different energy densities, compared to the theoretical calculations using g_{ei} from ABINIT calculation and J. Hohlfeld *et.al* [13]'s measured value. C_e is from our ABINIT calculation.

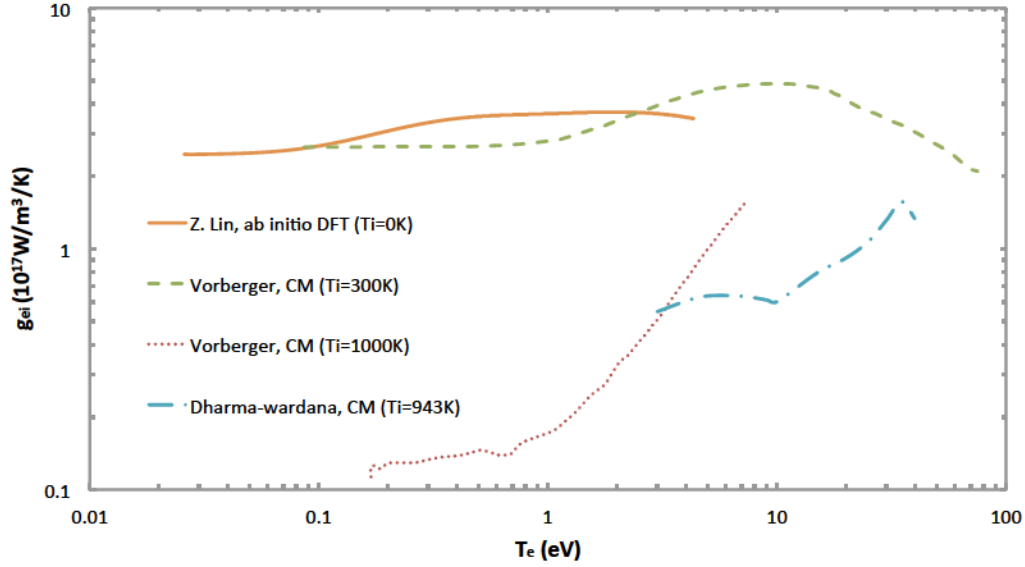


Figure 5.8: Comparison of g_{ei} of aluminium calculated by CM method (Vorberger *et.al* [130] and Dharma-wardana *et.al* [129]), and first principle DFT calculation(Lin *et.al* [14])

One possibility that could lead to having the calculated g_{ei} much weaker dependent of T_e is the lack of T_i dependence in the electron-phonon spectral function $\alpha^2 F(\Omega)$, which can only be calculated at 0K in first principle framework at the moment. To include ion temperature in the calculation of g_{ei} , there has been reports on aluminium that treats the ion collective motion as acoustic wave instead of phonon, which is usually called coupled mode (CM) calculation [129, 130]. The comparison between the g_{ei} of aluminum from CM calculation and first principles calculation is shown in Fig.5.8.

We can see that the g_{ei} value of aluminum using CM calculation with T_i at 300K is similar to those from DFT calculation by Lin *et. al* [14] using VASP, which is another package for *ab-initio* calculations similar to ABINIT. However, at around the melting point of aluminium, the results are around an order of magnitude below the one calculated at 300K. So far, there is no CM calculation for gold. The inclusion of CM effect in the calculation of gold may lead to much weaker T_e dependence in g_{ei} .

5.3 Summary

The AC conductivity in two temperature warm dense gold was calculated theoretically with first principles plane wave code ABINIT by our collaborators from CEA France. The calculated results were compared with our experimental measurement data in Chapter 4. The electron heat capacity C_e and electron-ion energy coupling factor g_{ei} were also calculated from ABINIT and benchmark tested through to the AC conductivity. The calculated real part of AC conductivity σ_r and C_e agree well with the experimental data. However, g_{ei} as a function of electron temperature is over estimated, which is likely resulted from the missing of ion temperature dependency in the calculation. Our comparison also points to the need to improve the calculation of σ_i .

Chapter 6

Interpretations of Warm Dense Gold using Two Temperature Model Calculation

Two temperature model has been widely used to interpret the experimental data of femtosecond laser excited warm dense matter. Two noticeable endeavours were taken to understand the disassembly conditions of femtosecond excited warm dense gold with the help of TTM. The motivation for such studies is that the non-equilibrium condition ($T_e \gg T_i$) after fs laser excitation may lead to the change of melting condition for the lattice. It was observed in certain material, such as silicon [61], germanium [62] and bismuth [131], that melting occurs well below the lattice melting point shortly after fs laser excitation. On the other hand, the super heating, i.e. the melting point well above the usual value, in non-equilibrium material is still in controversy. Gold is a candidate that super heating may occur according to the theoretical calculation of phonon spectrum [64].

The first study of gold by Ao *et.al* measured the hydrodynamic expansion of a thin free standing gold foil by frequency domain interferometry (FDI) [16], the second one by Ernstorfer *et.al* measured the disorder of lattice bond

structure by ultrafast electron diffraction (UED) [23]. In the first measurement, a super heated melting point well above the normal melting temperature was claimed according to their TTM calculation. In the second measurement, an increase in Debye Waller Factor (DWF) with T_e was interpreted from TTM, which was used to support the hypothesis of phonon hardening. However, when they carried out their own TTM calculations, either the electron heat capacity C_e , or the electron-ion coupling factor g_{ei} was significantly different from the optimum value that we found from the previous chapter. Here, the experimental data from these two studies will be re-analysed and re-interpreted with the optimal parameters, i.e. C_e from our DFT calculation, and g_{ei} as a constant value.

6.1 Interpretation of Lattice Disassembly Measurement

The experiment by Ao *et.al* [16] measured the FDI fringe shift of a 30nm warm dense gold thin foil as a function of time. The gold thin foil was excited by a 400nm laser pulse with 150fs FWHM. In their experiment, right after the initial change due to pump laser excitation, the phase shift stayed at almost a constant, which is called quasi-steady state (QSS). This QSS lasted for a few picosecond, depended on the excitation energy density (ΔE_D). During such time, it was considered that the high temperature electrons coupled their energy to the relatively cold ions. The QSS condition would hold until the point that the foil started to disassemble, where a more significant change of phase shift started to be observed. The duration of QSS at different heating energy densities ΔE_D was measured. By employing the TTM, the gained energy ($\Delta \epsilon$) of the ion system required for lattice disassembly was found. Their measured QSS lifetime as a function of excitation energy density is listed in Table 6.1. Using their experimental data from 0.5MJ/kg to 15MJ/kg excitation

$\Delta E_D(\text{MJ/kg})$	0.504±0.13	1.12±0.22	1.79±0.34	4.26±0.90	8.06±1.8	11.2±2.4	14.6±4.5
$T_{QSS}(\text{ps})$	20.1±2	15.5±1.8	12.5±1.5	6.0±0.7	3.2±0.7	2.2±0.6	1.7±0.5

Table 6.1: QSS life time of warm dense gold thin foil before disassembly as a function of excitation energy density ΔE_D [16]

energy density, the best fit value of $\Delta\epsilon$ is found to be $3.3\pm 0.3\times 10^5\text{J/kg}$. This is an indication of strong super heating, because the usual melting point of gold is only 1333K, or $1.34\times 10^5\text{J/kg}$ equivalent $\Delta\epsilon$. Even the latent heat of $6.5\times 10^4\text{J/kg}$ [121] is taken into account, the gain energy to the ion system is only $1.9\times 10^5\text{J/kg}$, which is still well below the melting condition suggested from their TTM calculation.

In Ao *et.al*'s TTM calculation, $g_{ei}=2.2\pm 0.3\times 10^{16}\text{W/m}^3/\text{K}$ was used, which is close to the optimum value that we found. However, their C_e is taken from the free electron gas model [34], which will lead to an over estimation of T_e as we found in Chapter 5. A plot of C_e for a range of T_e from 0 to 8 eV using FEG model, which was used by Ao *et.al*[16], and our ABINIT model, can be found in Fig.5.1. The T_e calculated at thermalization (540fs after laser excitation) for a range of excitation energy densities from 0 to 4MJ/kg using these two C_e models are shown in Fig.5.2. According to Eq.5.1, even with g_{ei} as a constant, a higher value of T_e will result in faster rising rate of T_i .

Here we carry out the TTM calculation using C_e from the result of ABINIT, and $g_{ei}=2.2\times 10^{16}\text{W/m}^3/\text{K}$ to re-examine the experimental data. For the first test, the ion gained energy $\Delta\epsilon$ at the time of measured disassembly as a function of excitation energy density is shown in Fig. 6.1

Our calculated $\Delta\epsilon$ fluctuates around the value at room condition, but it is obviously below the original value calculated by Ao *et.al* of $3.3\pm 0.3\times 10^5\text{J/kg}$. There is also a tendency that at higher excitation energy density, the required $\Delta\epsilon$ for disassembly decreases. This is likely due to the non-uniform heating at higher energy density. In Chapter 3, we observed that a significant thermal gradient is formed in 30nm gold thin foil above 5MJ/kg. Such gradient will re-

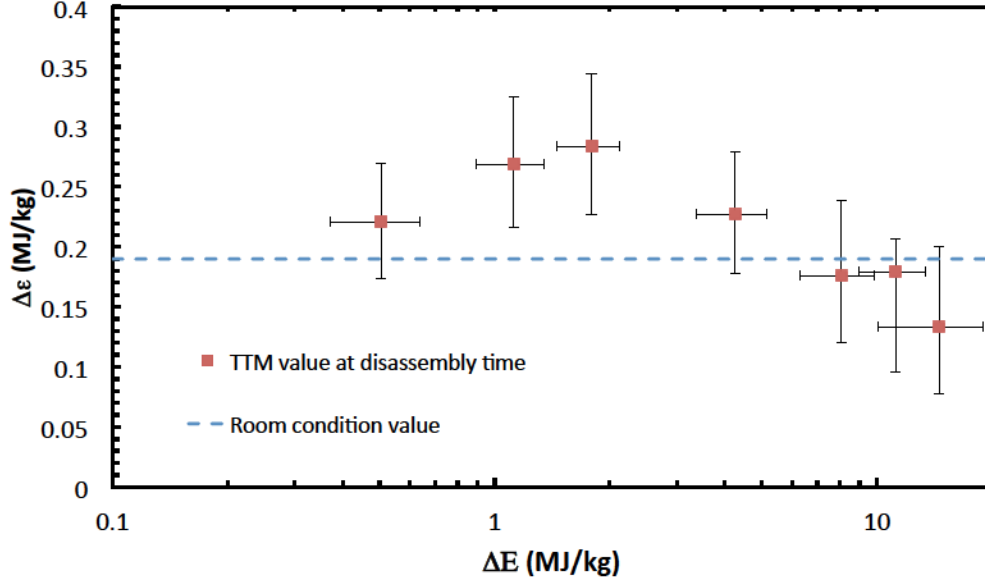


Figure 6.1: TTM calculation of the ion gained energy density $\Delta\epsilon$ at the time of lattice disassembly according to the measurement in [16]

sult in higher energy density on the front surface of the foil than the nominated value, which is based on the assumption uniform excitation. Since their FDI was measured on the front surface, earlier disassembly should be observed due to the higher than nominal energy density. Although Ao *et.al* used a longer pulse (150fs) than ours (45fs), which will have lower energy flux than in our experiment, we still used the same energy density limit as a cut off point here. The data above 5MJ/kg from their measurement is thus not considered at the moment. If we only consider the four data points below 4MJ/kg, the average $\Delta\epsilon$ give a value of $2.4 \times 10^5 \text{ J/kg}$.

In the next step, we try to find a value of $\Delta\epsilon$ that is best fit to Ao *et.al*'s measurement, within 5MJ/kg. The method is as follows,

- (1) Choose a value of $\Delta\epsilon$ between 2 and $3 \times 10^5 \text{ J/kg}$;
- (2) calculate the time (t_{TTM}) that it takes to for the ion energy to reach such $\Delta\epsilon$ using the reported excitation energy density ΔE_D ;
- (3) calculate the relative error between t_{TTM} and the measured time before disassembly (t_{QSS}), e.g. $err = (t_{TTM} - t_{QSS})/t_{QSS}$;

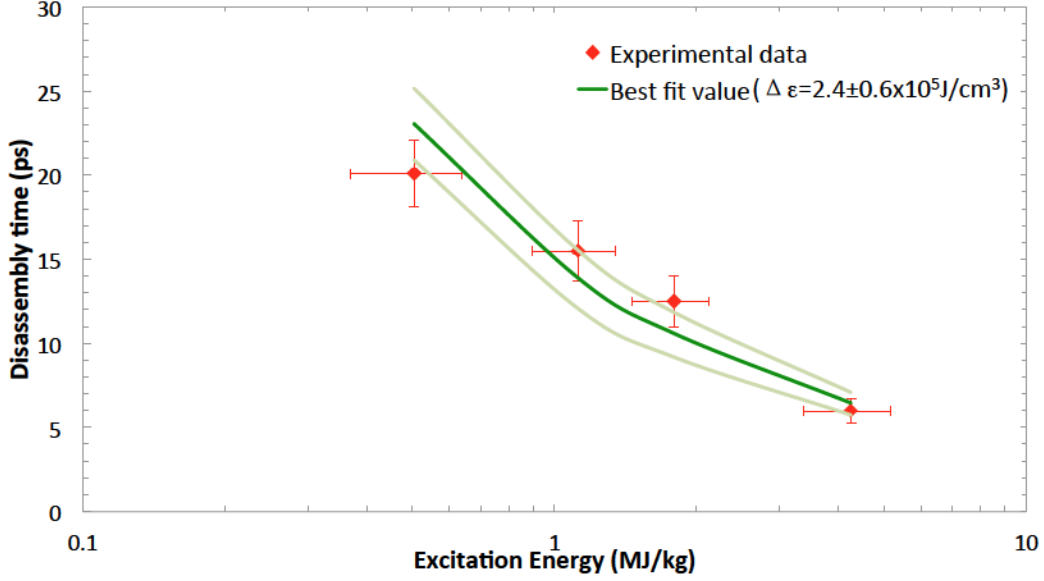


Figure 6.2: Best fit values of QSS with $\Delta\varepsilon=2.4\pm0.6\times10^5\text{J/kg}$ to the the experimental data below $\Delta E_D 5\text{MJ/kg}$ [16]. The light green lines represents the upper and lower boundary of our best fit $\Delta\varepsilon$.

(4) repeat the above steps for each energy density, and calculate the sum of square error;

(5) repeat the above steps for another $\Delta\varepsilon$, and find the corresponding error;

(6) the value of $\Delta\varepsilon$ that corresponds to minimum error is the best fit value.

Using our value of C_e from *ab initio*, and $g_{ei}=2.2\times10^{16}\text{W/m}^3/\text{K}$ for the TTM calculation, the best fit value of $\Delta\varepsilon$ is $2.4\pm0.6\times10^5\text{J/kg}$. Although such value is still higher than the requirement of disassembly of gold in normal heating, e.g. $1.9\times10^5\text{J/kg}$, it is still much lower than the original calculated value of $3.3\pm0.3\times10^5\text{J/kg}$. It suggests that the difference of $\Delta\varepsilon$ between ultrafast laser heating condition and normal heating condition is within experimental error, and more detailed study is needed in the future to investigate the possibility of super heating in non-equilibrium warm dense gold.

6.2 Interpretation of Phonon Hardening Measurement

In the study of femtosecond laser excited warm dense gold by Ernstorfer *et.al* [23], they used 55keV ultrashort (400fs) electron pulses [132] to measure Bragg diffraction from a 20nm gold thin foil excited by a 387nm, 200fs laser pulse. The intensity of the dominating 220 Bragg peak was measured as a function of time, and this peak was compared to the Debye Waller factor (DWF) as a function of T_i and Debye temperature Θ_D . Here, Θ_D was considered as a function of T_e , which increases monotonically to twice its room temperature value when $T_e=8\text{eV}$, according to the calculation of phonon spectrum at high T_e temperature by Recoules *et.al* [64]. As a result, the DWF depends on both T_e and T_i . Their time dependent T_e and T_i were calculated from TTM, with both C_e and g_{ei} from *ab initio* calculation [14]. Their calculated DWF has a similar decay rate as the 220 Bragg peak, so Ernstorfer *et.al* suggested that Θ_D increases as a function of T_e just as in the calculation by Recoules *et.al*. At a further step, according to Lindemann's theory of melting [26], the melting point of material $T_m \propto \Theta_D^2$, Ernstorfer *et.al* and Recoules *et.al* put forth the hypothesis that the melting point of gold will increase as a function of T_e .

Here I will revisit the data analysis in Ernstorfer *et.al*'s measurement using our optimum C_e and g_{ei} . Again, the TTM calculation follows Eq.5.1 with C_e from our ABINIT calculation, and $g_{ei}=2.2\times 10^{16}\text{W/m}^3/\text{K}$. In Ernstorfer *et.al*'s work, both C_e and g_{ei} are taken from Lin *et.al*'s calculation [14]. Here our C_e is significantly similar to Lin *et.al*'s calculation as shown in Fig.5.1, but we assumed a constant g_{ei} which is significant smaller than the that from Lin *et.al*'s calculation for T_e greater than 0.5eV as shown in Fig.5.3. In order to compare our calculation with the experimental data, we also followed the temperature dependent calculation of DWF [23, 34], which is a measure of the signal decay in electron diffraction from lattice disorder,

$$D(s, T_i, \Theta_D(T_e)) = \exp\left(-\frac{4}{3}\pi^2 \langle u^2 \rangle s^2\right) \quad (6.1a)$$

$$\langle u^2 \rangle = \frac{9h^2T_i}{4\pi^2mk_B\Theta_D^2(T_e)}\left[\frac{\Theta_D(T_e)}{4T_i} + \phi\left(\frac{\Theta_D(T_e)}{T_i}\right)\right] \quad (6.1b)$$

$$\phi\left(\frac{\Theta_D(T_e)}{T_i}\right) = \frac{T_i}{\Theta_D(T_e)} \int_0^{\Theta_D(T_e)/T_i} \frac{y}{e^y - 1} dy \quad (6.1c)$$

where s is the scattering vector in Bragg diffraction, which is 0.69\AA^{-1} for 220 peak of solid gold; $\langle u^2 \rangle$ is the mean square displacement of an ion from equilibrium due to thermal vibration; and $\phi\left(\frac{\Theta_D(T_e)}{T_i}\right)$ is the first order Debye function. The temperature dependent $\Theta_D(T_e)$ is obtained from the original report by Recoules *et.al* [64]. As mentioned by Ernstorfer *et.al*, the T_e calculated in Recoules *et.al*'s report was based on C_e from free electron gas model. In order to retrieve $\Theta_D(T_e)$ from their calculation, one has to convert our T_e to the corresponding value in their system, which is based on the conservation of internal energy U ,

$$\int_{T_0}^{T_e} C_e T dT = U = \int_{T_0}^{T_e^{FEG}} C_e^{FEG} T dT \quad (6.2)$$

where T_e^{FEG} and T_e^{FEG} denote the electron temperature and corresponding specific heat in Recoules *et.al*'s system.

Using g_{ei} from Lin *et.al*'s DFT calculation [14], we first reproduced the calculation result by Ernstorfer *et.al* to make sure that the all the details are followed. Then we set $g_{ei}=2.2\times 10^{16}\text{W/m}^3/\text{K}$ and redid the calculation, the results from calculation compared with the experimental data are shown in Fig.6.3. Obviously, our calculated decay of DWF does not fit the experimental decay of 220 peak.

In the original calculation of T_e dependent Debye temperature [64], their phonon spectrum was based on elevated T_e , but T_i could only be fixed at 0K, due to the limitation of the *ab initio* calculation at the moment. This is exactly

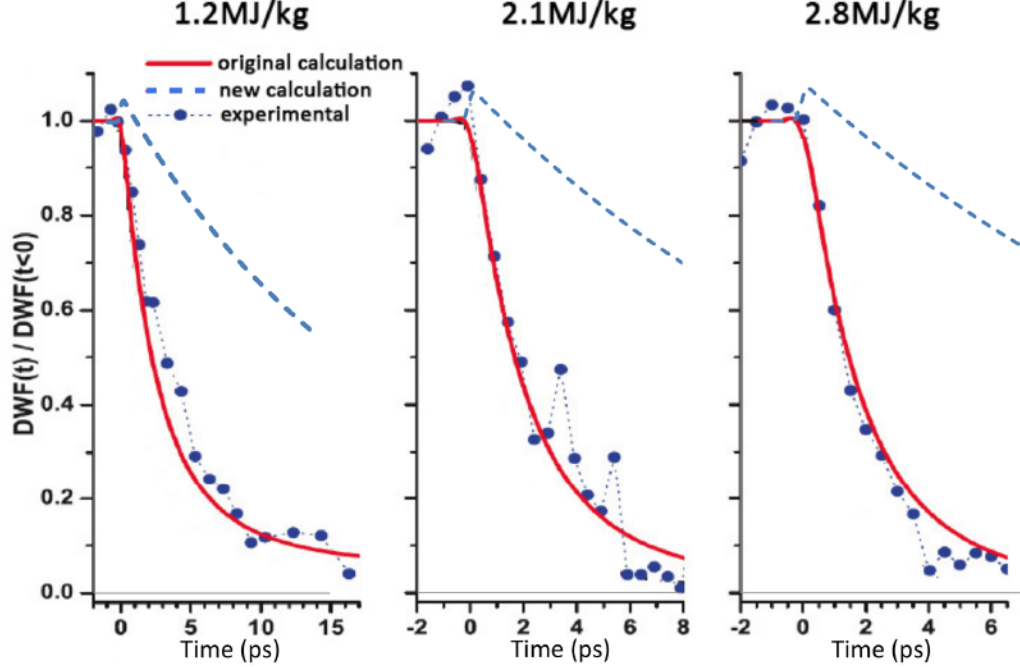


Figure 6.3: Recalculation of DWF with $g_{ei}=2.2 \times 10^{16} \text{W/m}^3/\text{K}$ and T_e depended C_e and Θ_D , compared to the original calculation and experimental data [23].

the limitation in the calculation of g_{ei} . For the next step, we use the same remedy for g_{ei} , e.g., use the room the temperature value $\Theta_D=165\text{K}$ for bulk gold [133] through out all T_e . The result of our calculation is shown in Fig.6.4. It turns out to be closer to the experimental result, but still significantly not in agreement.

Remember that the measurement by Ernstorfer *et.al* was based on the thin foils of 20nm thick. Early studies of optical properties by Johnson and Christy [48] found that ultra thin gold foils do not have complete solid properties until 30nm in thickness. Although thin film deposition technique have been improved over the years, the procedure of thin film fabrication and its properties were not reported by Ernstorfer *et.al*, which leave the uncertainties on the properties of film itself. Recent studies of gold thin film from vapour deposition found that Θ_D is only 99K for 20nm film, which is in close agreement with the observed reduction of Θ_D near gold surface [134]. If we assume that $\Theta_D=99\text{K}$ for the gold thin foils in the electron diffraction experiment, the calculated time dependent

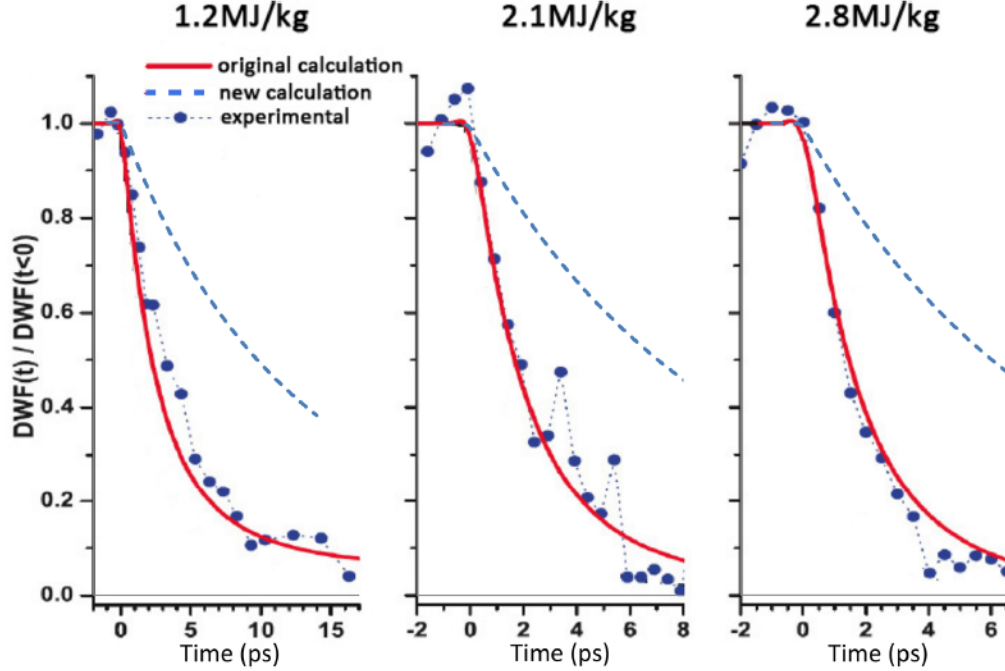


Figure 6.4: Recalculation of DWF with $g_{ei}=2.2\times 10^{16}\text{W/m}^3/\text{K}$ and $\Theta_D=165\text{K}$, compared to the original calculation and experimental data [23].

DWF compared with its original value is shown in Fig.6.5.

This time, good agreement is observed between the experimental data and calculation. Such a calculation gives another interpretation to the experimental data by Ernstorfer *et.al*, indicating a constant g_{ei} , and a constant Θ_D with a value appropriate for 20nm gold film can reproduce the experimental data reasonably well. Since the phonon hardening theory of gold proposed by Reoules *et.al* is based on a Θ_D that will increase with T_e , our interpretation of the results does not support such phenomenon. In Ernstorfer *et.al*'s TTM calculation, their result indicated that the T_i values calculated at the time that DWF decreases to $1/e$ of its original value, increase as the excitation energy density ΔE_D as shown in Table 6.2. For comparison, we did a similar calculation for T_i . It is clear that our calculated T_i for the three ΔE_D has no significant difference, and all are below the melting point of bulk gold.

According to Table 6.2, when DWF, or the 220 peak drops to $1/e$ of its original value, the ion temperature is around 930-1000K. As a side remark, if

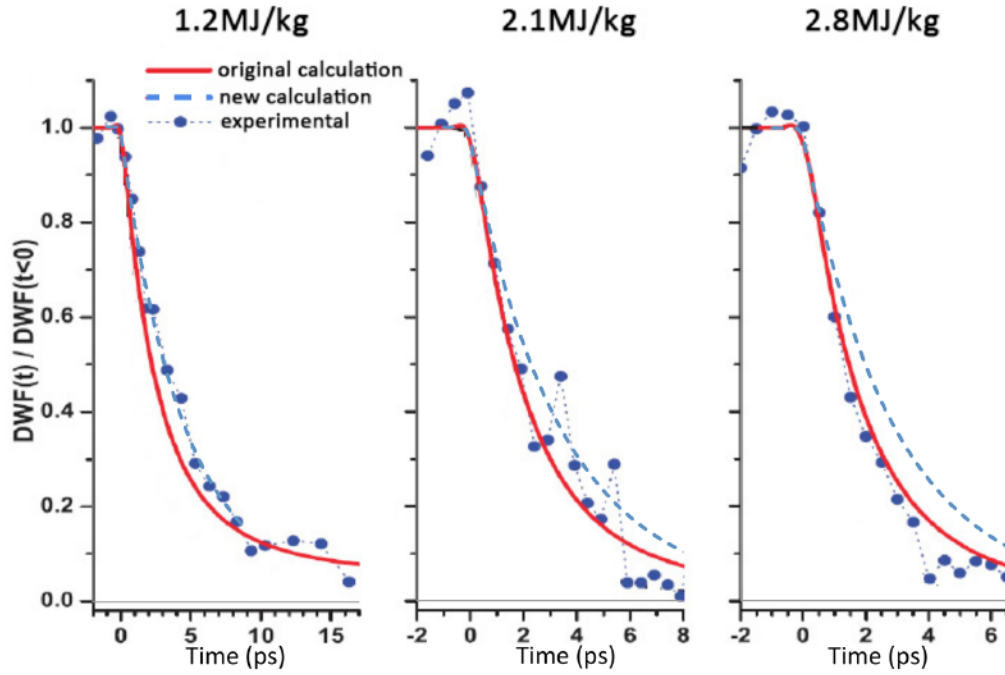


Figure 6.5: Recalculation of DWF with $g_{ei}=2.2\times 10^{16}\text{W/m}^3/\text{K}$ and $\Theta_D=99\text{K}$, compared to the original calculation and experimental data [23].

$\Delta E_D(\text{MJ/kg})$	1.2	2.1	2.85	source
$t^{DWF}(\text{ps})$	3.7	2.7	2.2	[23]
	4.1	3.4	2.5	this work
$T_i^{DWF}(\text{ps})$	3000K	3600K	4100K	[23]
	933K	1007K	928K	this work

Table 6.2: The time that it takes for DWF to reach 1/e of its original value, and the corresponding T_i at that time. Comparison between Ernstorfer *et.al*'s calculation and our calculation [23]

Θ_D of those 20nm thin foils is only about 99K, instead the bulk value 165K, one may expect that the melting point of gold decreases from the normal 1333K to only 480K according to Lindemann's melting criteria [26]. Even taking into consideration the latent heat of 65kJ/kg, or around 500K in equivalent ion temperature, the solid 220 peak should completely disappear near 1000K in equivalent temperature. The reason that the 220 peak only decreases to 1/e of the solid intensity may be explained by the early study in the surface science. The Θ_D is only about 110K for the surface layers of gold [134, 135], it was found that, instead of melting, there was a solid-solid phase transition on the surface layers at around 610K. Such phase transition results in a structure disorder and surface roughening, but the material remains in solid.

As a result, when we use C_e from *ab initio* calculation, and $g_{ei}=2.2\times 10^{16}\text{W/m}^3/\text{K}$, independent of T_e in the TTM calculation, the electron diffraction measurement of warm dense gold can still be interpreted with a constant Debye temperature, in contrast to the original interpretation that was based on T_e depended g_{ei} and Θ_D . Our only assumption here is the reduced Θ_D that may be needed for the 20nm gold thin foil used in the experiment.

In conclusion, when the optimal C_e and g_{ei} are used to interpret the two early studies of non-equilibrium warm dense gold ($T_e \gg T_i$, the condition for lattice disassembly tends to be close to that in equilibrium condition, in contrast to the super heating or phonon hardening that was suggested by the original investigators.

6.3 Summary

Two previous studies of lattice disassembly condition of femtosecond laser excited gold were re-analysed with two temperature model calculation. The optimum electron heat capacity C_e and electron-ion energy coupling factor g_{ei} were used in the calculations. Our results of analysis imply that the lattice melt-

ing point in non-equilibrium warm dense gold is similar to that in equilibrium condition.

Chapter 7

Femtosecond Laser Absorption Measurement in Thick Gold Film

The studies of femtosecond laser excited free standing ultra-thin gold film provided the opportunities to study non-equilibrium warm dense gold in an ideal condition with minimum density and temperature gradient. However, in real application, it is difficult to avoid the mixture of states. One simple example is the reflectivity of femtosecond laser pulse as a function of intensity/ energy fluence on a relatively thick gold film surface. This is similar to the early study of Milchberg *et. al* on aluminum [11], or a recent study by Kirkwood *et. al* on copper [12]. In those works, the authors used theoretical models to calculate the electrical conductivity, or dielectric constant in order to fit their experimental data. Here, I will use the dielectric constant from single state measurement to calculate reflectivity values and compare them with the experimental data.

7.1 Experimental Measurement

The measurement of femtosecond laser reflectivity on thick gold film surface was carried out at University of Alberta, using a Chirped Pulse Amplified (CPA) Ti:Sapphire femtosecond laser system. A brief description of this system is given below. More detail information can be found in the early work by Kirkwood [136].

7.1.1 Laser System

This system consists of two major components. One is the oscillator (Mai Tai, Spectra Physics), which generates trains of seed pulses at 80MHz with a Ti:Sapphire crystal by active modelocking. The average energy per pulse is about 5nJ. The second component is the regenerative CPA system (Hurricane, Spectra Physics). The output pulses from Mai Tai is chirped from about 100fs to sub-nanosecond width by a grating stretcher, which can reduced its intensity and avoid damage of the amplification medium, a Ti:Sapphire crystal. The amplification medium located in the cavity of Hurricane is pumped by a frequency double Nd:YLF laser (Envolution, Spectra Physics) at 527nm. The amplified laser pulses are recompressed by a grating compressor to its minimum duration. The typical spectral width of the laser pulse is about 8nm full width at half maximum (FWHM) centered at 800nm. According to the Fourier transform limit in Eq.3.1 for a Gaussian laser pulse in time, the minimum pulse duration is 120fs FWHM in theory. The actual laser pulse duration is measured by an autocorrelator (AAS, Positive Light). After optimizing the round trip distance of the pulse in the grating compressor, the FWHM pulse duration is 130fs. The maximum pulse energy is about $600\mu\text{J}$, and the beam waist diameter is 5mm.

The regenerative CAP system (regen) can amplify the energy of a fs laser pulse by 10^5 or more, however pre-pulses can also be generated from the regen cavity. There are two major kinds of pre-pulse. (1) The leakage from previous

round trips during the amplification, due to the limited contrast ratio of a pockels cell used to switch the laser pulse at its maximum energy. (2) Amplified spontaneous emission (ASE) from the Ti:sapphire crystal which is pumped to excitation states. In our laser system, the former one is the major source for pre-pulses, since we only have one pockels cell to select the output pulse, and its duration is similar to that of the main pulse. The pre-pulse contrast is measured by an FND-100 photodiode connected to a charge limited circuit [136], which prevents the overload of the photodiode when the main pulse arrives, so that the pre-pulse can be observed. The typical prepulse contrast is about 1500:1. If careful alignment is done in the regen cavity, i.e., maximizing the amplification rate of each round trip, and proper alignment to the pockels cell, it can reach about 3500:1.

7.1.2 Experimental Setup

The experimental setup is shown in Fig.7.1. The target is mounted on a three dimensional motorized stage, which is located inside a vacuum chamber at background pressure of 5×10^{-5} Torr. The laser system was controlled by external trigger. After each shot, the target was moved to a fresh area before the next shot. An aperture (A) of 5mm diameter was used to select the major part of the beam while cleaning out some low quality structure of the beam near its edge area. The laser beam is focused by a plano-convex lens L on to the target. Two sets of experiments were done with different lenses. The first one was a 10cm focal length, 1 inch diameter lens, while the second one was 8cm focal length and 2 inches diameter. The focused beam was normally incident onto the target surface. The reflected beam is collected by the same focal lens. The energy of the input and reflected beam was sampled by two wedges (W1 and W2) on to two FND-100 photodiodes (D1 and D2). The photodiode for incident energy D1 was calibrated by a joule meter (A407, Spectra Physics) placed after lens L, while D2 was cross calibrated with D1 by putting a dielec-

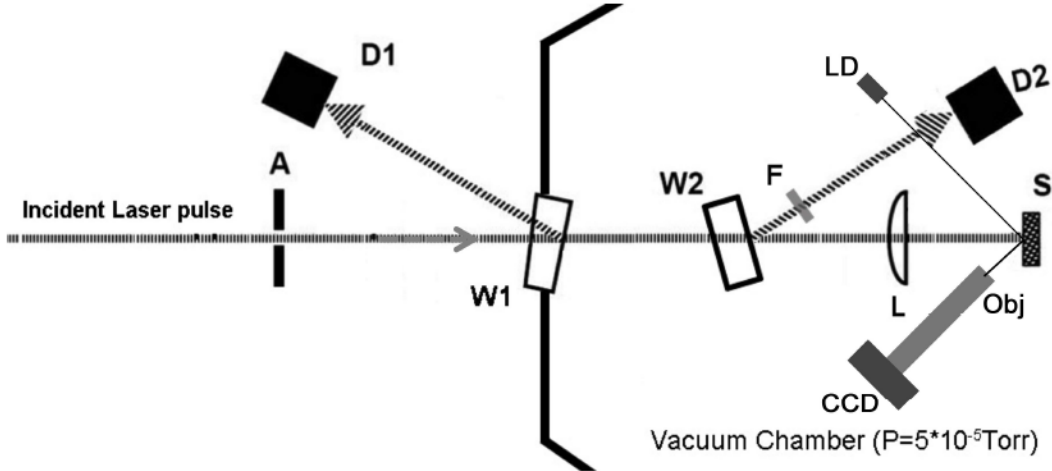


Figure 7.1: Setup of femtosecond laser absorption measurement. The incident laser pulse was at 800nm with a FWHM pulse duration of 130fs. A is an aperture of 5mm diameter, W1 and W2 are wedges to sample the input and reflected energy, while D1 and D2 are photodiodes to monitor the energy at each shot. L is an plano-convex lens to focus the laser beam on the target surface, and also collect the reflected laser energy. F is a long pass filter which has a cut-off edge at 720nm. S is the gold sample which is mounted on a motion stage, Obj and CCD are 3X microscope objective and CCD camera for an on-line imaging system on the target surface, LD is a laser diode which provides light source for the imaging system.

tric mirror near the target location but a little off the focus point of L to avoid damage. An imaging system consisted of a 3X microscope object (Obj) and a CCD camera (CCD) was used to monitor the target surface. The target was illuminated with a laser diode (LD). This system was used to locate the target at focal point of lens L, and look for a fresh area after each shot.

7.1.3 Sample and Spot Size Measurement

The sample the for laser absorption measurement is gold thin film sputtered on a silicon wafer substrate using the magnetron sputtering system (Bob) located in the nanofab of the University of Alberta. The thin film thickness was about 300nm, and a layer Chromium of 30nm thickness was sputtered between the gold film and the substrate as an adhesion layer. The background pressure for the sputtering system was about 10^{-6} Torr, while the Argon background pressure during the deposition is 7mTorr. The thin film has a similar surface

quality as the silicon wafer, whose RMS roughness is better than 1nm.

When a laser pulse interacts with a solid target, the energy of incident pulse E_{inc} can be divided into the following parts,

$$E_{inc} = E_{abs} + E_{ref} + E_{tra} + E_{scat} \quad (7.1)$$

where E_{abs} is the absorbed energy, E_{ref} and E_{tra} are the reflected and transmitted energy, and E_{scat} is the scatter energy. In the measurement, the laser intensity is no more than $10^{15}W/cm^2$, so the scattered part is negligible without a significant pre-pulse [31]. The gold film thickness is an order thicker than the optical skin depth at 800nm, so E_{tra} can also be ignored. The E_{abs} can then be obtained by measuring the energy of the input laser and its specular reflection.

To scale the laser absorption as a function of incident laser fluence (energy per unit area), one also needs to know the size of the laser spot. The size of the laser focal spot was determined from the sizes of ablation craters on target surface as a function of laser fluence, using the Gaussian beam limiting technique [137]. This technique assumes that the laser focal spot has a Gaussian distribution in space, whose electric field amplitude as a function of radius can be written as,

$$E(r) = E_0 \exp\left(-\frac{r^2}{r_0^2}\right) \quad (7.2)$$

where E_0 is the maximum E-field amplitude at the center of the spot, r_0 is the beam waist radius, where the field amplitude is only 1/e of its maximum. Accordingly, the laser intensity, which is proportional to the laser field amplitude, can be written as,

$$I(r) = \frac{|E(r)|^2}{2\eta} = I_0 \exp\left(-2\frac{r^2}{r_0^2}\right) \quad (7.3)$$

where η is the impedance of the medium where the beam propagates, and

I_0 is the maximum laser intensity at the center of the beam. Accordingly, the radial distribution of incident fluence is,

$$\varphi(r) = \varphi_0 \exp\left(-2\frac{r^2}{r_0^2}\right) \quad (7.4)$$

where φ_0 is the maximum incident laser fluence at the center of the focal spot. Assuming that ablation occurs once the local fluence reaches the damage threshold φ_{th} , and there is no significant blast wave which will damage the area where the local fluence is below φ_{th} , then the damage spot diameter D can be related to φ_{th} as,

$$\varphi_{th} = \varphi_0 \exp\left(-2\frac{(D/2)^2}{r_0^2}\right) \quad (7.5)$$

$$D^2 = 2r_0^2 \ln\left(\frac{\varphi_0}{\varphi_{th}}\right) \quad (7.6)$$

where D can be obtained by measuring the diameter of the ablation crater. Both φ_0 and φ_{th} are unknown. Fortunately, for the Gaussian laser pulse in space, the peak fluence can still be related to the incident laser energy E_{inc} ,

$$\varphi_0 = 2\frac{E_{inc}}{\pi r_0^2} \quad (7.7)$$

Using this relation, Eq. 7.6 can be written as ,

$$D^2 = 2r_0^2(\ln(E_{inc}) - \ln(\frac{\varphi_{th}\pi r_0^2}{2})) = 2r_0^2(\ln(E_{inc}) - \ln(E_{th})) \quad (7.8)$$

The incident laser energy can be plotted versus the squared of the crater diameter in linear scale, and linear fit applied to this plot will yield the values of E_{th} and beam waist radius r_0 .

The ablation spot size was measured by a white light profilometer (Newview 5000, Zygo), which measures the size and depth of a crater simultaneously. A 50X microscope objective with a numerical aperture (NA) of 0.5 was used for

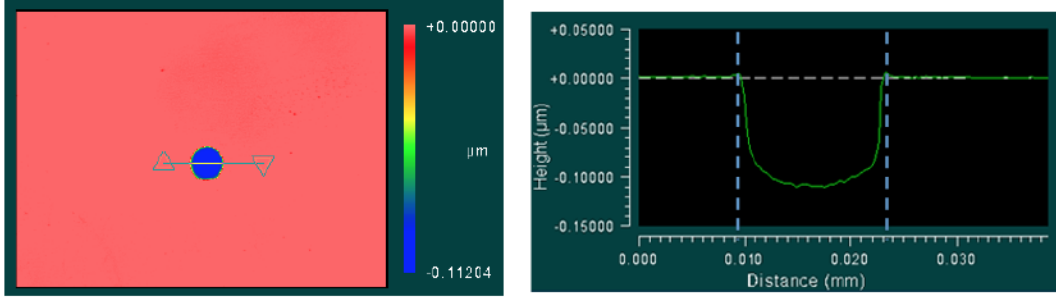


Figure 7.2: An ablation spot of $14.2\mu m$, measured by Zygo white light profilometer

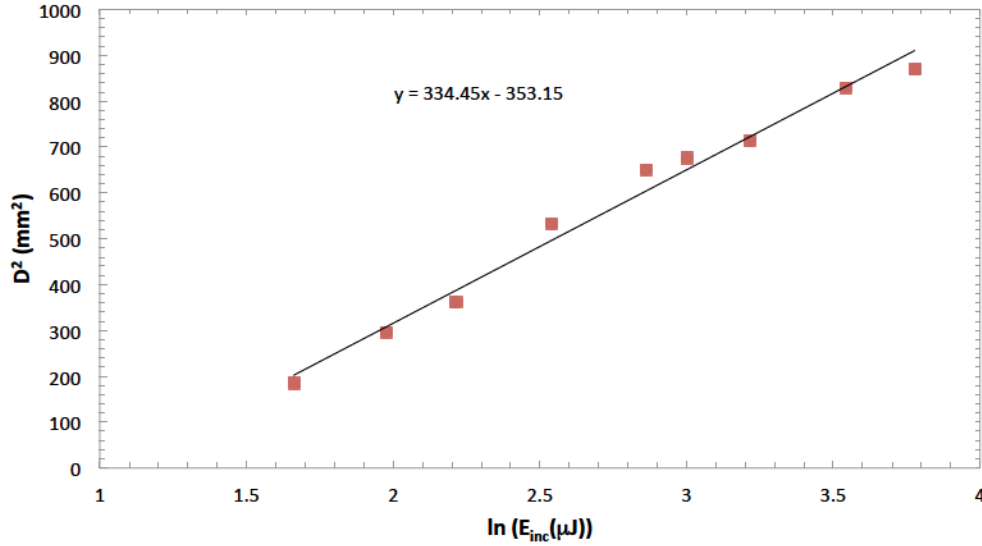


Figure 7.3: An example measurement plot to determine the spot size by the Gaussian beam limiting technique for the FL=10cm lens.

this profilometer. The lateral resolution is about $0.6\mu m$. An example of a crater of $14.2\mu m$ diameter, ablated with $1.1\mu J$ incident energy is shown in Fig. 7.2.

The semi-log plot of the square of crater diameter versus incident energy for the lens of 10cm focal length is shown in Fig. 7.3. According to Eq.7.8,

$$r_0 = \frac{D^2}{2(\ln(E_{inc}) - \ln(E_{th}))} = \sqrt{334.45/2} = 12.9\mu m.$$

The threshold energy is $E_{th} = \exp(353.15/334.45) = 2.87\mu J$. The corresponding threshold ablation fluence is $0.96 J/cm^2$, which agrees well with the previous study of 800nm, 120fs laser pulse ablation of gold thin film [138], which gave a threshold ablation fluence of $0.94 \pm 0.06 J/cm^2$.

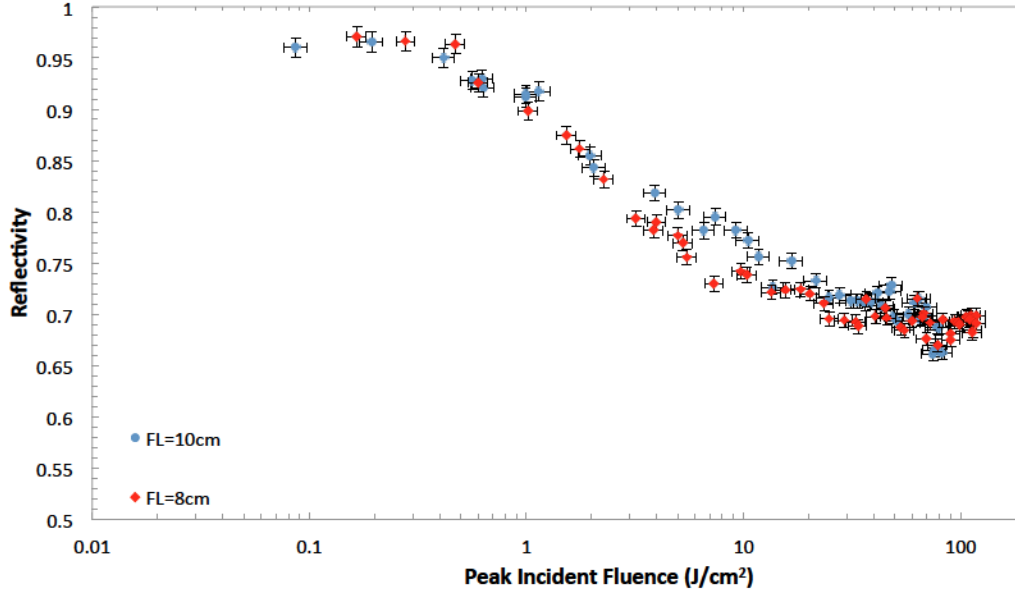


Figure 7.4: Experimental results of the absorption of 800nm, 150fs laser pulses as a function of incident fluence on gold thin film. FL indicates the focal length of the used laser beam focusing optics.

7.1.4 Experimental Result

Two sets of experiments were done using lenses of different focal length (FL). The first one has an FL=10cm, and diameter is 2 inches. The second one was FL=8cm, and diameter is 1 inch. The experimental results are shown in Fig.7.4.

We can see that the reflectivity of the gold thin film starts to drop even below the ablation threshold fluence. The absorption fraction increases significantly until it reaches $\sim 30\%$ at $\sim 10J/cm^2$, and it starts to saturate. Only a small amount of change in reflectivity between $10J/cm^2$ and $100J/cm^2$. This saturation is likely the result of the continuous increase of free electron density at higher fluence. On one hand, it helps to increase the collisional absorption, on the other hand, it increases the plasma frequency and the penetration depth of laser light decreases near the target surface.

7.2 Comparison to Calculations with Single State Dielectric Constant

To describe the femtosecond laser interaction with solids, a two temperature model (TTM) is used, although the electrons may not be completely thermalized during the laser pulse. We will do this calculation only for the low laser fluence regime up to $0.5J/cm^2$, for which the dielectric function was measured in single state. Before the end of the 150fs pulse, most of the absorbed energy remains in the electron system, while the lattice stays cold, so only the equation that describes the electron system is considered here, while the electron-ion coupling is ignored. Equation 2.24 can then be simplified as,

$$Q(z, t) = C_e \frac{\partial T_e}{\partial t} - \frac{\partial}{\partial z} \kappa(T_e) \frac{\partial T_e}{\partial z} \quad (7.9)$$

where $Q(t, z)$ is the local laser absorption, C_e is the electron heat capacity taken from ABINIT calculation from Chapter 5, and κ is the electron thermal conductivity. According to the front and rear reflectivity measurement in Chapter 3, if a temperature gradient exists over a 30nm, it takes more than 7ps to transfer energy from the front surface to the rear. This suggests that the contribution from electron thermal diffusion within a 150fs laser pulse may be ignored from the above equation within the range of our calculation. It should be noted that such approximation is only valid when T_e is not larger than E_F . At high T_e regime, the thermal conductivity increases as T_e significantly according to Eq. 2.28 and plays a significant role even in femtosecond time scale. On the other hand, the ballistic electron energy transportation is the major mechanism that carries energy from the target surface to the inside of it during the laser pulse. A simple way to take into account the energy redistribution inside the film by ballistic electron energy transportation is to replace the local laser absorption term $Q(z, t)$ with the energy distribution term $Q_e(z, t)$. The relation between $Q(z, t)$ and $Q_e(z, t)$ needs to follow the energy conservation,

$$\int_0^\infty Q_e(z, t) dz = \int_0^\infty Q(z, t) dz \quad (7.10)$$

where 0 denotes the target surface. The ballistic electron range l_{ba} is approximately 100nm [13], which is much larger than the skin depth of laser absorption. Accordingly the final energy deposition should be primarily dictated by ballistic transportation. Assuming that such energy distribution has exponential distribution below the target surface, we have

$$Q_e(z, t) = Q_e(0, t) \exp(-z/l_{ba}) \quad (7.11)$$

As a result, Eq.7.9 may be simplified as,

$$Q_e(z, t) = C_e \frac{\partial T_e}{\partial t} \quad (7.12)$$

For the incident laser pulse, it should have a Gaussian distribution in time. Its time dependent intensity distribution may be written as,

$$I(t) = I_0 \exp(-4 \ln(2) (\frac{t - t_0}{\tau_{1/2}})^2) \quad (7.13)$$

where I_0 is the peak laser intensity, and t_0 is the time of the peak intensity. $\tau_{1/2}$ is the FWHM pulse width, which is 150fs in this study. According to Gaussian integral, the relation between the peak fluence (φ_0) and the peak intensity (I_0) for a Gaussian pulse is,

$$I_0 = 2 \sqrt{\frac{\ln(2)}{\pi}} \frac{\varphi_0}{\tau_{1/2}} \approx 0.94 \frac{\varphi_0}{\tau_{1/2}} \quad (7.14)$$

The laser field amplitude inside the target follows the wave equations,

$$\frac{\partial^2 E(t, z)}{\partial z^2} + \frac{\omega^2}{c^2} \varepsilon(t, z) E(t, z) = 0 \quad (7.15)$$

where z is the direction of laser propagation. The temperature dependent

dielectric constant $\varepsilon(t, z)$ is extracted from our single state measurement. Here we assume that the dielectric constant from thermalized electron system is similar to that during the pump laser pulse.

The above partial differential equation can be solved with two boundary conditions: (1) at the vacuum target interface ($z=0$), $-i\frac{c}{\omega}\frac{\partial E(t, 0)}{\partial z} + E(t, 0) = 2E_0(t)$; and (2) $E(t, z \rightarrow \infty) = 0$. $E_0(t, 0)$ is the incident laser field amplitude. In vacuum, according to Eq. 7.3 the relation between intensity $I(t)$ and $E_0(t, 0)$ is,

$$I(t) = \frac{cE_0(t, 0)^2}{8\pi} \quad (7.16)$$

The time and depth integrated absorption is thus given by,

$$\langle A \rangle = \frac{\int_0^{4\tau_{1/2}} \int_0^\infty Q(t, z) dt dz}{\int_0^{4\tau_{1/2}} I(t) dt} \quad (7.17)$$

where the local laser absorption $Q(t, z) = \frac{1}{2}\omega\frac{\text{Im}(\varepsilon(t, z))}{4\pi}|E(t, z)|^2$ follows the form of ohmic heating. The time for peak of laser pulse (t_0) is located at $\tau_{1/2}$. The corresponding reflectivity is $\langle R \rangle = 1 - \langle A \rangle$.

Since the laser focal spot has Gaussian distribution in radial direction, the overall absorption needs to take into account the Gaussian integral,

$$A_{total} = \frac{\int_0^\infty A(r) \exp(-2(\frac{r}{r_0})^2) 2\pi r dr}{\pi r_0^2 / 2} \quad (7.18)$$

where $A(r)$ is the calculated local absorption from r to the center of the spot, r_0 is the beam waist radius, and the denominator is the normalized total incident energy according to Eq.7.7.

The comparison of our calculation with the experimental data in this regime is shown in Fig.7.5. Since our single state measurement is only upto $Te = 3eV$, which limits our calculation to a peak fluence of $0.5\text{J}/\text{cm}^2$. As we can see the reflectivity values calculated based on single state data are in general slightly

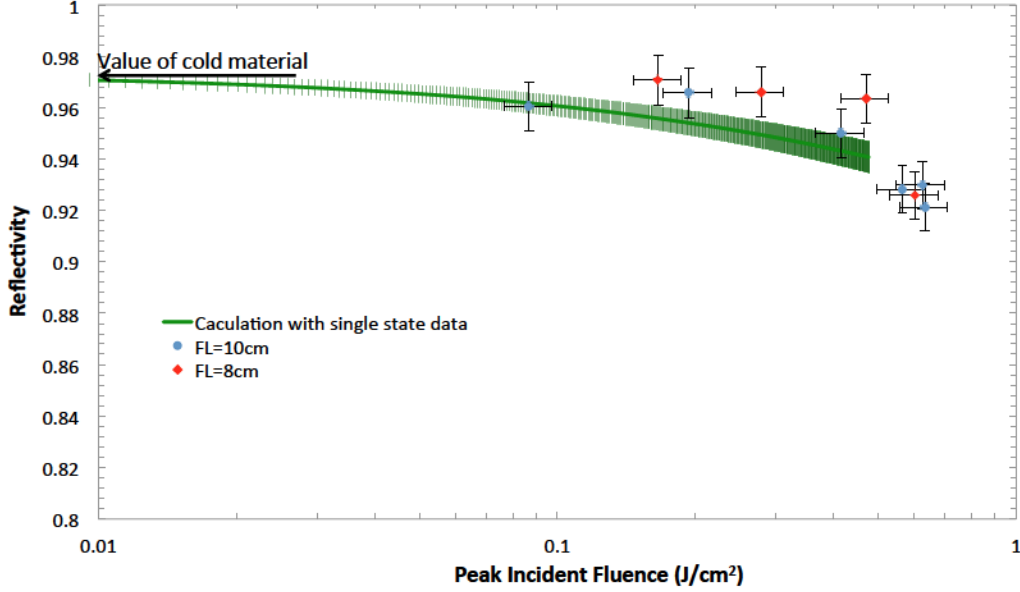


Figure 7.5: The calculated laser reflectivity as a function of peak energy fluence using dielectric functions measured at single state compares to experimental data. FL indicates the focal length of the used laser beam focusing optics.

lower than the experimental values for peak laser fluence below $0.5 J/cm^2$. If we follow the trend of the reflectivity values calculated based on the single state data, it seems to have a better agreement with the experimental data at fluence higher than $0.5 J/cm^2$. In our calculation we have assumed that the dielectric function of warm dense gold during the 150fs excitation laser pulse is the same as that in thermalized states. Although systematic study on dielectric function when electrons are not in well define thermal distribution is still missing, transient reflectivity measurement by Sun *et. al* [8] suggests that the change in reflectivity is less when electrons are not thermalized, while the thermalization time decreases as the laser fluence increases. This perhaps points to why the change of reflectivity from experimental data is less than the calculation result at low laser fluence, where the electrons are further away from thermalization during the laser pulse, but apparently agreeing better with experimental data at slightly higher fluences.

7.3 Summary

Our previous measurement of dielectric function for single state warm dense gold gives reasonable agreement with the non-uniformly excited state measurement of femtosecond reflectivity as a function of energy fluence in the low fluence regime. The discrepancy between the calculation and experimental result points to the need for further study of the properties of warm dense matter with non-thermalized electron systems. Also, it is clear that the models and measured dielectric functions in single state must be extended to higher incident fluence to describe the full range of interaction intensities typically used in femtosecond laser ablation applications.

Chapter 8

Tuning of Silicon Microring Resonators

In this chapter, an application in material processing using femtosecond laser pulse is demonstrated, I have used them to tune the resonant frequency of silicon microring resonators (SMR), which are one of the building blocks for photonic integrated circuits (PIC). The SMRs are provided by Prof. Vien Van's group at the University of Alberta, and this work was done in collaboration with Daniel Bachman, another Ph.D student in Dr. Van's group.

8.1 Silicon Microring Resonators

In the development of information technology, higher bandwidth for data transfer is increasingly essential. In telecommunications, fibre-optics has been demonstrated to be superior than traditional copper wire based systems due to its low loss, lower cost and larger bandwidth [139]. However, most information processing still relies on microelectronics and the data transfer within a multi-core processor or between microprocessors still largely depends on copper interconnects. Due to electrical resistivity, over 50% of the power in a microprocessor based system is lost in such interconnects [140]. One way to reduce the losses

and also to increase bandwidth is to use micro optical interconnects, which transfers photons in planar waveguides made by dielectric material, such as silicon, instead of electrical current in metal wires. The photons travel inside a waveguide due to total internal reflection as in an optical fibre. Such planar waveguides may be integrated with existing electronic systems, especially those silicon on insulator (SOI) based complementary metal-oxide semiconductor (CMOS) systems [141, 142].

To better utilize the bandwidth provided by optical telecommunication, a technique called wavelength-division-multiplexing (WDM, different from WDM short for warm dense matter) [139] is widely used. It can also be adopted for use in optical interconnects. This technique transmits multiple channels of information carried by different wavelengths through a single fibre/waveguide. If the non-linear effects are well controlled, the crosstalk between those channels should be minimized. To decode the information, it requires the separation of wavelengths at the destination interconnects. Silicon microring resonators (SMR) are compact devices which can be used for such propose.

An SMR is a closed loop silicon waveguide usually in circular or race track shape [143, 144]. It is usually placed close to a section of planar waveguides and works as an optical frequency/wavelength selector. An example is shown in Fig. 8.1, which is an SEM picture of a $1.5\mu m$ radius SMR [145]. The distance between the waveguides and the SMR is small enough at the coupling junction, so that the evanescent wave from total internal reflection in the planar waveguide can couple to the resonator before significant attenuation. An SMR has its own resonant condition. If a coupled optical signal is tuned to a resonant frequency of the SMR, it will have the same phase when it travels around the loop back to the coupling junction. As a result, constructive interference happens and more signal of the same frequency will continue to couple to the SMR effectively. The non-resonant components cannot build up in the SMR, and a large part of those frequencies will continue to travel along the planar

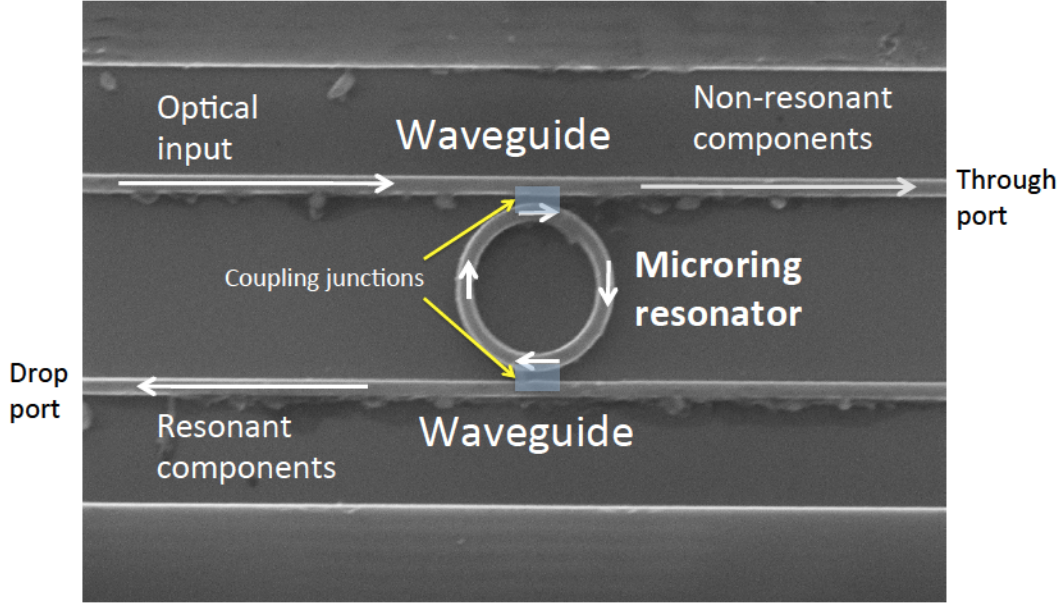


Figure 8.1: An SEM picture of a silicon microring resonator

waveguide to the through port. In order to receive the signal selected by an SMR, one needs to have another planar waveguide so that the built-up signal in the SMR can evanescently coupled into it. In the end, the signal travels to the drop port where they will continue to be processed.

In order to use an SMR properly so that the desired signal can be selected, one needs to control its resonant condition, which has the general form,

$$2\pi R = \frac{m\lambda}{n_{eff}} \quad (8.1)$$

where R is the radius of a circular SMR, λ is the free space wavelength of an optical signal, m is an positive integer or usually called the mode number, and n_{eff} is the effective refractive index of the ring. The effective refractive index n_{eff} depends on the geometry of the waveguide, and the refractive index of the material. In a simple circular waveguide, one has $n_{eff} = n \sin \theta_t$, with the refractive index of material n , and θ_t the internal refraction angle for the t_{th} traverse mode. In reality, an SMR is a bent rectangular waveguide, and the calculation of n_{eff} is complicated. The value is then determined by a numerical

mode solver [144] when an SMR is designed, so that the optical signal carried by wavelength component $\lambda = \frac{2\pi R n_{eff}}{m}$ can be selected.

In reality, when an SMR is fabricated, n_{eff} can easily deviate from its original design due to the limit of accuracy to which a device can be fabricated, which will lead to a different than desired resonant frequency. A typical width or height of the waveguide of an SMR is less than 500nm [145]. If an error of 1nm or about 0.2% results from the fabrication, a same order of error is expected in n_{eff} and the corresponding λ in resonance. Although this amount of error looks small, it can lead to a deviation of about 3nm in resonant wavelength, or ~ 300 GHz in frequency, for a typical λ around 1550nm for optical communication. Such amount of error is not acceptable. So far, achieving sub-nanometer accuracy in silicon thin film fabrication is still a challenge [146, 147], and post fabrication tuning becomes necessary.

A few techniques for post fabrication tuning of SMRs have been developed. One way is to change the refractive index of silicon by changing its temperature [148, 149]. In that case it is needed to build micro-heaters on the device, which complicates the fabrication procedure, and requires continuous feed back control during operation. Moreover, during operation, extra energy is consumed continuously. Some other ways can tune the SMR permanently, which includes the modification of cladding layer on top of the SMR by UV [150] or visible [151] light photons, or oxidizing part of the silicon to silicon dioxide (SiO_2) [152]. The former one requires special photon sensitive cladding layer that may not be compatible with the device, and the later one needs precise control of local oxidation, which requires a complicated setup such as an atomic force microscope platform.

Here, I will present an alternative way to tune the SMRs permanently with femtosecond laser pulses, which is fast and does not require a complicated setup.

8.2 Changing the Effective Refractive Index of Silicon Microring Resonators by Femtosecond Laser Pulses

As mentioned above, the effective refractive index of an SMR is determined by its geometric configuration, and the refractive index of the silicon. It has been reported that a femtosecond laser pulse has the capability to remove small portions of silicon by ablation, or change its refractive index by photon induced amorphization [153, 154], which depends on the laser energy fluence and intensity. At low laser fluence, the excited silicon reaches just over the melting condition and cools down rapidly, so it does not have enough time to form the crystal structure and becomes amorphous silicon (a-Si). The precise refractive index of an a-Si varies depending on the details of how it is formed [155, 156], but in general, it is larger than that of crystalline silicon (c-Si). As a result, if part of the SMR waveguide transforms from c-Si to a-Si, it will result in the increase in n_{eff} and increase in resonant wavelength (red shift). On the other hand, when the laser energy is high enough that the heated Si is ablated, the height of the SMR will reduce. This will result in a reduction of n_{eff} and reduction in resonant wavelength (blue shift). Based on these two processes, the capability of post fabrication tuning of SMRs was demonstrated.

The experiments were carried out with the Hurricane femtosecond laser system at the University of Alberta as described in Chapter 7. The 800nm output of the laser system was frequency doubled by a BBO crystal to 400nm. The penetration depth of 400nm photons is two orders of magnitude smaller than that of the 800nm ones in silicon [54], so that the tuning can be better controlled. The experimental setup for tuning the SMRs is shown in Fig.8.2. Instead of a Gaussian focal spot, a top-hat spot was used to excite the SMR. This is implemented by demagnified imaging a small pin hole (less than a mil-

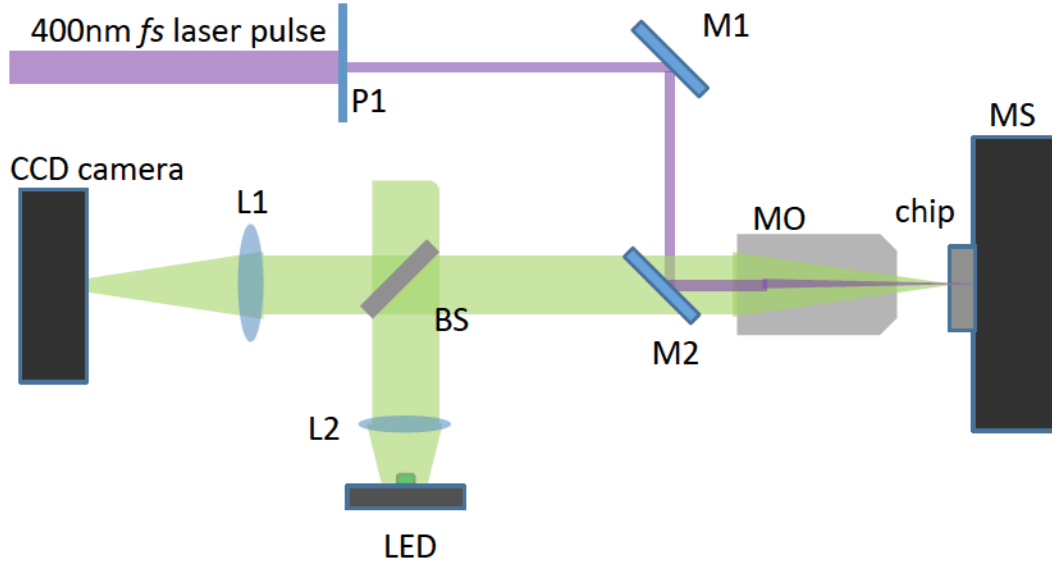


Figure 8.2: Experimental setup that is used to tune the SMRs using 400nm, 150fs laser pulses. The center part of the laser passes through a small pin hole(P1) that is less than 1mm diameter and images onto the surface of SMR using a 10X microscope objective (MO) with 0.28 numerical aperture. The microchip with SMRs is mounted on a 3 dimensional motion stage(MS). The surface of the chip is imaged by a CCD camera with the illumination of a green light LED. On the figure, M1 and M2 are 45° dielectric mirrors for the 400nm beam, L1 and L2 are lenses, and BS is a beam splitter. L1 images the surface of the ring on to the CCD and L2 collimates the LED lights.

limeter) located in the the center part of the non-focused laser beam. The intensity distribution in the top-hat spot was close to uniform with no more than 20% variation, which can minimize the mixture of amporization and ablation on the same laser shot. Before and after each laser shot, the resonant wavelength of the SMR was measured by another setup shown in Fig. 8.3.

8.2.1 Tuning a Silicon Microring Resonators with Multiple Laser Shots on a Same Area

In the first study, we used an SMR of $1.5\mu\text{m}$ radius [145]. The top hat laser spot on target has a diameter of $20\mu\text{m}$, which covers the whole SMR and the waveguides that couples light in and out of the ring. The detail of this study have been published in *Optics Letters* [157] and the article is provided as

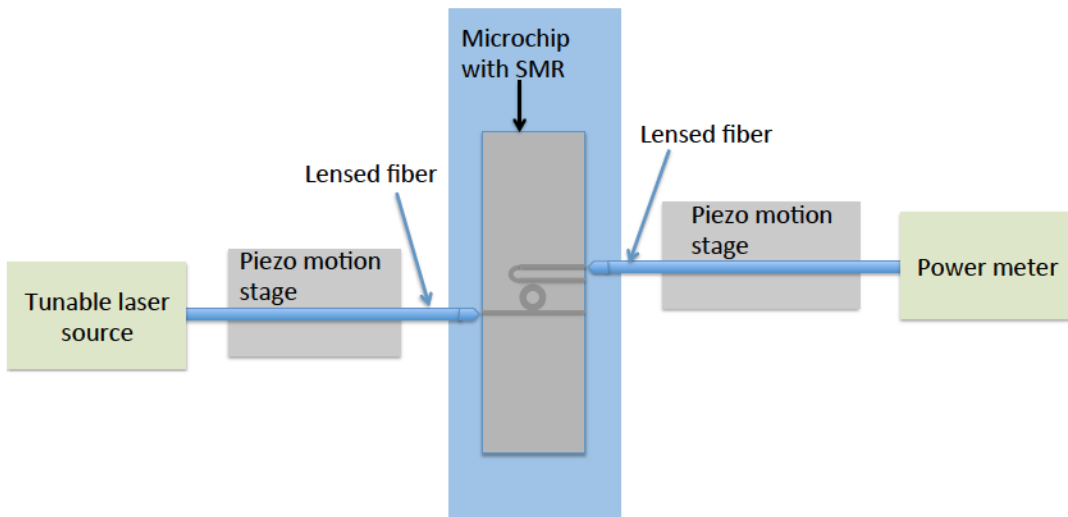


Figure 8.3: Experimental setup that was used to measure the resonant wavelength of the SMRs. The microchip with SMR is mounted on a stage with two lensed fibers on left and right. The input photons from a tunable laser source go through the fiber on the left and couple in to the waveguide of the chip. The photons that have the resonant wavelength will go to the drop port and couple into the fiber on the right, and the corresponding power is measure by a power meter. The two fibers are mounted on piezo motion stages, so that they can be aligned with the waveguides on the edges of the microchip precisely.

Appendix A.

This study provides the first demonstration of the capability of tuning an SMR with femtosecond laser pulses. It shows that there are two regimes of tuning an SMR by a femtosecond laser pulse, namely, amorphization and ablation. We found that the threshold energy fluence to amorphize the ring is about $60\pm 14\text{mJ/cm}^2$, which will result in a red shift of resonant wavelength. At above $200\pm 47\text{mJ/cm}^2$, the SMR surface will be ablated, and the resonant wavelength will reduce. However, the experiment was based on only one SMR, so that the SMR was processed many times. As a result, the threshold for each tuning regime as well as the amount of shift after each shot are subjected to the accumulated effect of the previous shots. The relation between laser fluence and the change of n_{eff} , which is the key to controlling the resonant wavelength, had large uncertainties in this study but the uncertainties are greatly reduced in a followed up study which will be described next.

8.2.2 Controllable Tuning of a Silicon Microring Resonator

In order to understand how the laser fluence relates to the n_{eff} of an SMR, a fresh area of a ring needs to be processed each time instead of accumulating multiple shots on the same area. For such study, a microchip with 7 separated SMRs of essentially the same size were fabricated. The rings have $15\mu\text{m}$ radius, and in this study the laser spot radius was reduced to $8.8\mu\text{m}$, so that two laser shots could modify the left and right sections of an SMR separately. It also avoided the modification of the coupling junctions of the SMRs and their coupling waveguides, which can help to determined the change of n_{eff} precisely. This work is published in *Optics Express* and the article is provided in Appendix B.

In this work, we have found that when the incident fluence was in the range

of 60-200mJ/cm² , the amount of wavelength shift after each shot was essentially linearly related to the incident fluence with a slope of 20±2 nm/(J·cm⁻²), which provides a large range of controllable tuning of SMR. In order to generalize this fluence dependent tuning factor, the change of effective refractive index within the modified spot is extracted from the amount of wavelength shift given by the expression,

$$\Delta n_{eff} = \frac{\Delta \lambda}{\lambda} \frac{2\pi R}{l} n_{eff} \quad (8.2)$$

where the n_{eff} is the original effective index, which is about 2.3 according to the mode solver [158]; $R=15\mu\text{m}$ is the radius of the ring, λ is the original resonant wavelength near 1550nm before the tuning; l is the length of the laser modified section. The ratio of $2\pi R$ over l can be obtained by solving triangular equations. For this case, a $8.8\mu\text{m}$ radius laser spot with the center on a $15\mu\text{m}$ radius SMR is shown in Fig.8.4. Because $l=2\alpha R$, we have $\frac{2\pi R}{l} = \frac{\pi}{\alpha}$. Obviously, $\alpha = \arccos(\frac{a^2 + c^2 - b^2}{2ac}) = 0.60$. According to Eq.8.2, the relation between n_{eff} and laser fluence can be obtained, with a corresponding slope of $0.16 \pm 0.02 / (\text{J} \cdot \text{cm}^{-2})$.

In the ablation regime, where resonant wavelength shifted to the shorter side, no clear relation between energy fluence and amount of shift was observed.

In this study (See Appendix B), we have also used such controllable tuning capability to align the resonant peaks of a system with two SMRs. The two rings are $8\mu\text{m}$ and $12\mu\text{m}$ in radius. The $12\mu\text{m}$ ring has a peak at 1535nm, while the $8\mu\text{m}$ one has a peak which is 1.1nm shorter in wavelength. To tune the $8\mu\text{m}$ ring by 1.1nm, it requires a $\Delta n_{eff} = \frac{1.1}{1535} \times 2.3 = 0.0016$. According to the relation between effective index shift and laser fluence, a possible solution is to use the threshold fluence at 60mJ/cm², and modified only 1/6 of the total length of the ring. Ideally, this requires the center of the $R=8.8\mu\text{m}$ laser spot locate at $15\mu\text{m}$ away from the center of the $8\mu\text{m}$ ring. In our experiment, when

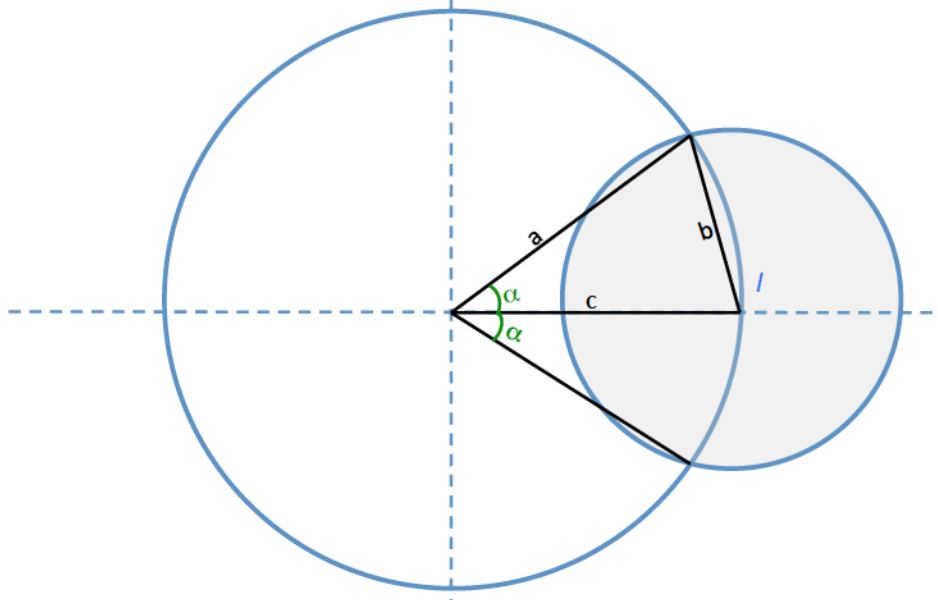


Figure 8.4: A laser spot of $8.8\mu\text{m}$ radius shot on the right section of a $15\mu\text{m}$ radius microring. In the figure, a and c equal to $15\mu\text{m}$, b equals to $8.8\mu\text{m}$, and l is the length of the excited section.

we tuned the resonant wavelength it changed by 1.4nm instead of 1.1nm . This is likely due to the slight misalignment of the center of the laser spot which in the experiment was only $14\mu\text{m}$ away from the SMR center, nevertheless, the resonant frequency of the two rings still was overlapped with each other sufficiently for many applications.

8.3 Limitations and Future Improvements

According to our studies, we have shown that femtosecond laser pulses are a promising candidate to tune the SMRs after fabrication. The potential limitation of this technique is the increase of loss. In our studies, the increased loss per round trip is in the range between 0.1 and 0.5dB in the amorphization regime, and between 0.2 and 0.8dB in the ablation regime. The relation between laser fluence and the increase of loss has not been characterized in detail yet. In general, we observed significantly more loss if the tuning was done using the ablation process compared to those using the amorphization process. The

loss in the amorphization regime is likely due to larger absorption loss in a-Si than that in c-Si. Although only a small amount of c-Si is amorphized on the surface of an SMR after laser modification, the absorption coefficient in a-Si can be 4 orders of magnitude higher than c-Si at 1550nm [54].

To reduce the loss from laser induced a-Si, one possibility is to use thermal annealing. It has been observed that after thermal annealing at 400°C for 1 hour, the optical absorption coefficient in the range between 1.1 and 1.8eV was reduced by over an order of magnitude [159]. Although no measurement was done at 0.8eV (1550nm), a similar trend may be expected. At higher annealing temperature. e.g. around 600°C or above, re-crystallization of a-Si occurs, which will flip the resonant shift from femtosecond laser tuning [159, 160]. Care also needs to be taken even in annealing without re-crystallization, because a reduction of the refractive index was observed in annealed ion implantation produced a-Si before crystallization occurs [161].

Since we observed that better controllability and lower loss occur in the amorphization regime compared to the ablation regime, it is better to focus the future study on the amorphization regime. However, in the amorphization regime, the resonant wavelength can only be tuned to the longer direction. Fortunately, in an SMR there are multiple resonant peaks that are in accordance with the resonant condition in Eq. 8.1. The separation of these peaks in wavelength are called free spectrum range(FSR). The FSR of a peak of interest at λ_0 can be approximated as [158],

$$\lambda_{FSR} \approx \frac{\lambda_0^2}{2\pi R n_g} \quad (8.3)$$

where n_g is the group effective refractive index, which relates to n_{eff} as $n_g = n_{eff} - \frac{dn_{eff}}{d\lambda}$. In silicon, $\frac{dn_{eff}}{d\lambda}$ is negative since its refractive index decreases with λ . As a result, n_g should be larger than n_{eff} .

Coming back to the situation that an SMR needs to be tuned to shorter wavelength, an example is illustrated in Fig.8.5. If the desired wavelength is at

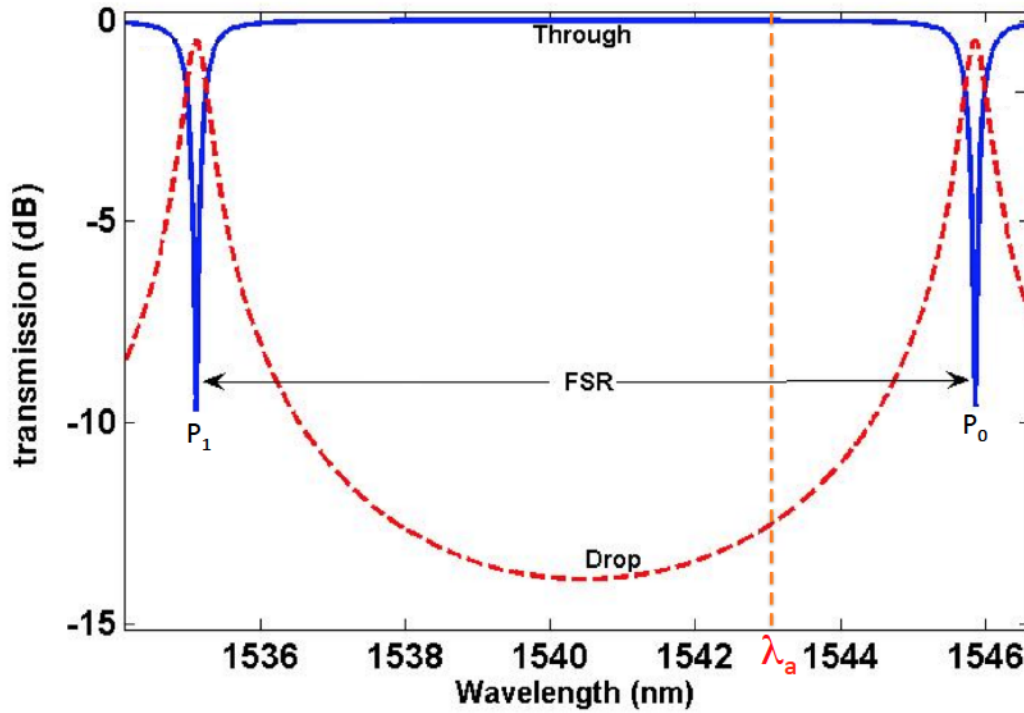


Figure 8.5: A scheme to tune the resonant wavelength to desire value (λ_a) by amorphization only.

λ_a , it is tempting to reduce n_{eff} for P_0 that it will become λ_a . However, it is also possible that by increasing n_{eff} using laser induced amorphization, so that P_1 moves to λ_a . Although it needs a larger amount of wavelength shift to tune P_1 than P_0 , this is still possible as long as λ_{FSR} is not larger than the maximum range of red shift due to femtosecond laser induced amorphization. Using the result from Appendix B for 400nm, 150fs laser pulse, the linear relation between n_{eff} change and laser fluence is $0.16 \pm 0.02 / (\text{J} \cdot \text{cm}^{-2})$. It means that at 0.2 J/cm^2 just below the ablation threshold, one can tune n_{eff} by 0.032, or a maximum red shift of 21nm at 1550nm. For an SMR whose λ_{FSR} is larger than the maximum red shift, one may switch to the fundamental wavelength of the femtosecond laser system at 800nm, because it has larger penetration depth than that of 400nm [162], and a larger amount of red shift due to amorphization is expected.

In the case that fine tuning is required, i.e. only a very small amount of

red shift is needed, a very low laser fluence slightly above the threshold of amorphization can be used with a smaller laser spot at the same time. In our previous studies, the top-hat laser spots imaged on target came from the image of the center area of the original beam that passed through a pin hole. To obtain even smaller spot size, one can focus the laser beam to a Gaussian shape without using any pin hole aperture. For a focusing lens with numerical aperture of 0.28, which is the same as the one we used, a 400nm incident beam can be focused down to only $1\mu\text{m}$ beam waist diameter. When a Gaussian focal spot is used, in principle, one can amorphize a circular area whose radius is well below the beam waist radius, if the fluence at the peak of the beam is just over the threshold. However, the effect of using a gaussian laser spot instead of a top hat laser spot needs to be studied

Last but not least, if the amount of red shift after a shot is more than necessary, which can be a result of energy fluence fluctuation from shot to shot, or limitation of alignment accuracy, one can always re-crystallize the the a-Si by employing multiple shots of femtosecond laser pulses at about half of the energy fluence of amorphization threshold [163]. This can be done simply by exposing the SMR under the laser pulses with high repetition rate (1kHz) for about a second.

To accelerate the process of laser tuning, efforts are needed to have a setup that can measure the resonant wavelength(e.g. Fig.8.3) of the SMRs and tune them(e.g. Fig. 8.2) simultaneously without moving the SMR device. Currently, a large part of the time in the experiments were the alignments of the device in each setup, it would be much more efficient if we can measure the resonant shift in-situ right after each laser shot without moving from one setup to the other.

8.4 Summary

A new application using femtosecond laser pulses to tune the silicon microring resonators was explored. The tunings to either longer or shorter wavelengths by laser induced amorphization or laser ablation were demonstrated. Further study and improvement to this technique is also proposed.

Chapter 9

Impact and Future Work

9.1 Impacts of the Thesis Research

My thesis research was focused on the study of femtosecond laser pulse excited gold in non-equilibrium warm dense matter state under uniformly heated condition. This provides an ideal situation to study the femtosecond laser excitation of metal. In addition, the femtosecond laser pulse tuning of silicon microring resonators has been demonstrated and studied as a new application using femtosecond lasers. The major contributions from my Ph.D study include,

(1) Verified the uniform excitation of free standing gold thin foil by femtosecond laser pulse using front and rear side probe pulses measurements. Observed the upper limit of uniform excitation, which may be a result of saturation of energy that the laser excited ballistic electrons can carry. This does not only provide guidance to single state measurements with free standing thin foil, but also points to the need to study non-equilibrium electron energy transport.

(2) Using the single shot, frequency chirped pulse probe technique, the AC conductivity at 800nm from femtosecond laser excited warm dense gold was deduced from the measurement of reflectivity and transmissivity. Such measurements avoided the shot to shot fluctuations and unveiled the details of AC conductivity evolution in non-equilibrium warm dense gold.

(3) The AC conductivity data of warm dense gold were used to benchmark the electron heat capacity C_e and electron-ion energy coupling factor g_{ei} obtained from first principles calculations. It is found that C_e from first principles calculation gives better agreement than that from free electron gas model, while g_{ei} is significantly overestimated, which may be a result of the lack of including the T_i dependent phonon spectrum in the g_{ei} calculation. The calculated AC conductivity was also compared with the experimental data, which points to the need of improvement in obtaining the imaginary part σ_i .

(4) Using the optimum values of C_e and g_{ei} , the previous reported studies that suggested super heating [16] and phonon hardening [23] of non-equilibrium gold were re-analysed and re-interpreted. Our interpretation does not support super heating nor phonon hardening hypotheses. This should draw attention to the phase transition condition in non-equilibrium warm dense matter.

(5) Using the AC conductivity of gold from uniformly excited single state measurement, the reflectivity of a pump pulse as a function of laser fluence was calculated for a thicker target with thermal gradient and compared with experimental data. Partial agreement was found. It also indicates the need to the study of material property without a well defined electron temperature distribution, an even less studied regime in non-equilibrium warm dense matter.

(6) Using femtosecond laser pulses, post-fabrication tuning of microring resonators was demonstrated, and controllable tuning was investigated towards actual implementation. This gives a post processing solution to address the limited precision in the fabrication of silicon micro photonic devices.

9.2 Future Research Directions

Further studies from my thesis research can lead to more detailed understanding of femtosecond laser matter interaction and material in non-equilibrium warm dense state. Two suggestions for future work based on the studies reported

here are listed below,

9.2.1 Properties of Warm Dense Matter with Non-thermalized Electrons

Studies of warm dense matter are usually in a two temperature framework, i.e. non-equal T_e and T_i . However, at even shorter time scale, well defined temperature does not exist in electron system. This regime is especially important to the understanding of laser absorption, the very first step in femtosecond laser matter interaction, as well as ballistic electron energy transport. The challenge in such study is the requirement of significantly shorter laser pulse duration than the electron thermalization time, which is usually in tens or hundreds of femtoseconds. With the availability of commercial femtosecond laser system at 20-30fs pulse duration [164], or using non-linear pulse shaping techniques such as self-phase modulation [165], less than 10fs pulse duration is available. This provides the possibility to measure non-thermalized electron properties in warm dense matter in the near future.

9.2.2 DC Conductivity of Warm Dense Matter

Using optical probe pulses, AC conductivity at the photon frequency can be measured. However, more throughout understanding of particle and energy transport comes from the DC electrical conductivity. Measurement of DC conductivity in femtosecond laser excited warm dense matter has not be performed electrically, because the excited material expands on a picosecond time scale, which is much faster than the response time for most electronic devices. Although DC conductivity may be extracted from AC conductivity measured by femtosecond laser pulses, according to Drude model relation [34],

$$\sigma_0 = \sigma_r [1 + (\frac{\omega}{\nu})^2] \quad (9.1)$$

where σ_0 is the DC conductivity, σ_r is the real part of the measured AC conductivity, ω is the angular frequency of the laser pulse and ν is the electron collision frequency, which can be also extracted from the AC conductivity,

$$\nu = \frac{\sigma_r \omega}{\sigma_i} \quad (9.2)$$

where σ_i is the imaginary part of the the measured AC conductivity. However, the laser pulse frequency is similar to the electron collision frequency, so that the optical probe pulse may interfere the collision process and reduce the accuracy in extracting ν . If one can use a probe pulse with much lower frequency than ν , more reliable DC conductivity may be able to extract. According to Eq.9.1, when ω is much less than ν , the DC conductivity σ_0 can be closely approximated from σ_r . Terahertz (THz) radiation pulses with sub-picosecond duration[166] are a good candidate for such measurement. The measurements of quasi-DC conductivity using THz EM wave has been performed in gold thin films at room condition [167], and femtosecond laser excited warm dense aluminum[168]. However, the warm dense aluminum in the reported study was not uniformly excited and thus was in mixed states with uncertain gradients of density and temperature. THz conductivity measurements, under quasi-DC conditions, of uniformly excited single state warm dense solids similar to those reported in this thesis should result in better DC conductivity measurements by removing the uncertainties due to temperature and density gradient. The quasi-DC conductivity extracted from THz measurement can be compared with those extracted from optical frequency measurements. Such studies could lead to better understanding of the relations between AC conductivity and DC conductivity for non-equilibrium warm dense matter.

Bibliography

- [1] W. Sibbett, A.A. Lagatsky, and C.T. A. Brown. The development and application of femtosecond laser systems. *Opt. Exp.*, 20:6989, 2012.
- [2] S.E. Kirkwood, M.T. Taschuk, Y.Y. Tsui, and R. Fedosejevs. Nanomilling surfaces using near-threshold femtosecond laser pulses. *J. Phys.: Conference Series*, 59:591, 2007.
- [3] S.S. Bulanov, A. Brantov, V.Y. Bychenkov, V. Chvykov, G. Kalinchenko, T. Matsuoka, P. Rousseau, S. Reed, V. Yanovsky, K. Krushelnick, D.W. Litzenberg, and A. Maksimchuk. Accelerating protons to therapeutic energies with ultraintense, ultraclean, and ultrashort laser pulses. *Med. Phys.*, 35:1770, 2006.
- [4] M.Z. Mo, A. Ali, S. Fourmaux, P. Lassonde, and R. Fedosejevs J.C. Kieffer. Quasimonoeenergetic electron beams from laser wakefield acceleration in pure nitrogen. *Appl. Phys. Lett.*, 100:074101, 2012.
- [5] A. Vailionis, E.G. Gamaly, V. Mizeikis, W. Yang, A.V. Rode, and S. Juodkazis. Evidence of superdense aluminium synthesized by ultrafast microexplosion. *Nature Communications*, 2:445, 2011.
- [6] M. Tabak, D. Hinkel, S. Atzeni, E.M. Campbell, and K. Tanaka. Fast Ignition: Overview and Background. *Fusion Science and Technology*, 49:254, 2006.

- [7] R. Le Harzic, N. Huot, E. Audouard, C. Jonin, P. Laporte, S. Valette, A. Fraczkiewicz, and R. Fortunier. Comparison of heat-affected zones due to nanosecond and femtosecond laser pulses using transmission electronic microscopy. *Appl. Phys. Lett.*, 80:3886, 2002.
- [8] C.K. Sun, F. Vallee, L.H. Acioli, E.P. Ippen, and J.G. Fujimoto. Femtosecond tunable measurement of electron thermalization in gold. *Phys. Rev. B*, 50:15337, 1994.
- [9] W.S. Fann, R. Storz, H.W.K. Tom, and J. Bokor. Electron Thermalization in Gold. *Phys. Rev. B*, 46:13592, 1992.
- [10] B.Y. Mueller and B. Rethfeld. Relaxation dynamics in laser-excited metals under nonequilibrium conditions. *Phys. Rev. B*, 87:035139, 2013.
- [11] H.M. Milchberg, R.R. Freeman, S.C. Davey, and R.M. More. Resistivity of a Simple Metal from Room Temperature to 10^6 K. *Phys. Rev. Lett.*, 61:2364, 1988.
- [12] S. E. Kirkwood, Y.Y. Tsui, R. Fedosejevs, A.V. Brantov, and V. Yu. Bychenkov 2. Experimental and theoretical study of absorption of femtosecond laser pulses in interaction with solid copper targets. *Phys. Rev. B*, 79:144120, 2009.
- [13] J. Hohlfeld, S.-S. Wellershoff, J. Gdde, U. Conrad, V. Jahnke, and E. Matthias. Electron and lattice dynamics following optical excitation of metals. *Chem. Phys.*, 251:237, 2000.
- [14] Z. Lin and L.V. Zhigilei. Electron-phonon coupling and electron heat capacity of metals under conditions of strong electron-phonon nonequilibrium. *Phys. Rev. B*, 77:075133, 2008.
- [15] A. Ng, T. Ao, F. Perrot, M.W.C. Dharma-wardana, and M.E. Foord.

- Idealized slab plasma approach for the study of warm dense matter. *Laser Part. Beams*, 23:527, 2005.
- [16] T. Ao, Y. Ping, K. Widmann, D.F. Price, E. Lee, H. Tam, P.T. Springer, and A. Ng. Optical Properties in Nonequilibrium Phase Transitions. *Phys. Rev. Lett.*, 96:055001, 2006.
- [17] B. Holst, V. Recoules, S. Mazevet, M. Torrent, A. Ng, Z. Chen, S. E. Kirkwood, V. Sametoglu, M. Reid, and Y. Y. Tsui. An ab initio model on optical properties of non-equilibrium Warm Dense Matter. *Phys. Rev. B*, 90:035121, 2014.
- [18] A. Ng, P. Celliers, A. Forsman, R.M. More, Y.T. Lee, F. Perrot, M.W.C. Dharma-wardana, and G.A. Rinker. Reflectivity of Intense Femtosecond Laser Pulse from a Simple Metal. *Phys. Rev. Lett.*, 72:3351, 1994.
- [19] A. Forsman, A. Ng, and G. Chiu. Interaction of femtosecond laser pulses with ultrathin foils. *Phys. Rev. E*, 58:R1248, 1998.
- [20] K. Widmann, T. Ao, M.E. Foord, D.F. Price, A.D. Ellis, P.T. Springer, and A. Ng. Single-State Measurement of Electrical Conductivity of Warm Dense Gold. *Phys. Rev. Lett.*, 92:125002, 2004.
- [21] Y. Ping, D. Hanson, I. Koslow, T. Ogitsu, D. Prendergast, E. Schwegler, G. Collins, and A. Ng. Broadband Dielectric Function of Nonequilibrium Warm Dense Gold. *Phys. Rev. Lett.*, 96:255003, 2006.
- [22] T. Ao. *Optical Properties of Ultrafast Laser Heated Solid*. PhD thesis, University of British Columbia, 2004.
- [23] R. Ernstorfer, M. Harb, C.T. Hebeisen, G. Sciaini, T. Dartigalongue, and R.J. Dwayne Miller. The Formation of Warm Dense Matter: Experimental Evidence for Electronic Bond Hardening in Gold. *Science*, 323:1033, 2009.

- [24] W.S. Fann, R. Storz, H.W.K. Tom, and J. Bokor. Direct measurement of Nonequilibrium electron-energy distribution. *Phys. Rev. Lett.*, 68:2834, 1992.
- [25] C.K. Sun, F. Vallee, L.H. Acioli, E.P. Ippen, and J.G. Fujimoto. Femtosecond investigation of electron thermalization in gold. *Phys. Rev. B*, 48:12365, 1993.
- [26] F.A. Lindemann. The calculation of molecular vibration frequencies. *Physik. Z.*, 11:609, 1910.
- [27] J.N. Shapiro. Lindemann Law and Lattice Dynamics. *Phys. Rev. B*, 1:3982, 1970.
- [28] S. Mazevet, J. Cle rouin, V. Recoules, P.M. Anglade, and G. Zerah. Ab-Initio Simulations of the Optical Properties of Warm Dense Gold. *Phys. Rev. Lett.*, 95:085002, 2005.
- [29] R. Fedosejevs, R. Ottmann, R. Sigel, G. Kühnle, S. Szatmari, and F.P. Schäfer. Absorption of Femtosecond Laser Pulses in High-Density Plasma. *Phys. Rev. Lett.*, 64:1250, 1990.
- [30] R. Fedosejevs, R. Ottmann, R. Sigel, G. Kühnle, S. Szatmari, and F.P. Schäfer. Absorption of Subpicosecond Ultraviolet Laser Pulses in High Density Plasmas. *Appl. Phys. B*, 50:79, 1990.
- [31] D.F. Price, R.M. More, R.S. Walling, G. Guethlein, R.L. Shepherd, R.E. Stewart, and W.E. White. Absorption of Ultrashot Laser Pulse by Solid Targets Heated Rapidly to Temperature 1-1000eV. *Phys. Rev. Lett.*, 75:252, 1995.
- [32] Y. Ping, R. Shepherd, B.F. Lasinski, M. Tabak, H. Chen, H.K. Chung, K.B. Fournier, S.B. Hansen, A. Kemp, D.A. Liedahl, K. Widmann, S.C. Wilks, W. Rozmus, and M. Sherlock. Absorption of short laser pulses on

- solid targets in the ultrarelativistic regime. *Phys. Rev. Lett.*, 100:085004, 2008.
- [33] D. Fisher, M. Fraenkel, Z. Henis, E. Moshe, and S. Eliezer. Interband and intraband (drude) contributions to femtosecond laser absorption in aluminum. *Phys. Rev. E*, 65:016409, 2001.
- [34] N.W. Ashcroft and N.D. Mermin. *Solid State Physics*. Harcourt Brace Jovanovich Publishers, 1976.
- [35] P. Drude. Zur Elektronentheorie der metalle. *Annalen der Physik*, 306: 566, 1900.
- [36] F.F. Chen. *Introduction to Plasma and Controlled Fusion, Vol. I: Plasma Physics*. Plenum Press, 2nd edition, 1984.
- [37] H.-K. Chung, W.L. Morgan, and R.W. Lee. FLYCHK: an extension to the K-shell spectroscopy kinetics model FLY. *J. Quant. Spectrosc. Radiat. Transf.*, 81:107, 2003.
- [38] A.A. Abrikosov. *Fundamentals of the theory of metals*. North Holland, 1988.
- [39] L. Spitzer. *Physics of fully ionized gases*. Interscience Publishers, 2nd edition, 1962.
- [40] A. V. Brantov, V. Yu. Bychenkov, and W. Rozmus. Electron Transport and Permittivity in a Plasma with an Arbitrary Ionic Charge. *JETP*, 106:983, 2008.
- [41] W. Rozmus, V. T. Tikhonchuk, and R. Cauble. A model of ultrashort laser pulse absorption in solid targets. *Phys. Plasmas*, 3:360, 1996.

- [42] A. V. Brantov and V. Yu. Bychenkov. Taking into Account Electron-Electron Collisions in Classical Absorption of Short Laser Pulses. *Plasma Phys. Rep.*, 35:274, 2009.
- [43] J.P. Freidberg, R.W. Mitchell, R. L. Morse, and L. I. Rudstinski. Resonant Absorption of Laser Light by Plasma Targets. *Phys. Rev. Lett.*, 28:795, 1972.
- [44] D. W. Forslund, J.M. Kindel, Kenneth Lee, E.L. Lindman, and R.L. Morse. Theory and simulation of resonant absorption in a hot plasma. *Phys. Rev. A*, 11:679, 1975.
- [45] J.C. Kieffer, P. Audebert, M. Chaker, J.P. Matte, H. Ppin, T.W. Johnston, P. Maine, D. Meyerhofer, J. Delettrez, D. Strickland, P. Bado, and G. Mourou. Short-Pulse Laser Absorption in Very Steep Plasma Density Gradients. *Phys. Rev. Lett.*, 62:760, 1989.
- [46] F. Brunel. Not-So-Resonant, Resonant Absorption. *Phys. Rev. Lett.*, 59:52, 1987.
- [47] W. Rozmus and V. T. Tikhonchuk. Skin effect and interaction of short laser pulses with dense plasmas. *Phys. Rev. A*, 42:7402, 1990.
- [48] P.B. Johnson and R.W. Christy. Optical Constants of the Noble Metals. *Phys. Rev. B*, 6:4370, 1972.
- [49] L.V. Keldysh. Ionization in the Field of a Strong Electromagnetic Wave . *Sov. Phys. JETP*, 20:1307, 1965.
- [50] P Gibbon and E Fo rster. Short-pulse laserplasma interactions. *Plasma Phys. Control. Fusion*, 38:769, 1996.
- [51] S.C. Wilks. Simulations of ultraintense laserplasma interactions. *Phys. Flu.*, 5:2603, 1993.

- [52] D. Pine and P. Nozieres, editors. *The Theory of Quantum Liquids*. Benjamin, New York, 1966.
- [53] S. I. Anisimov, B. L. Kapeliovich, and T. L. Perelman. Electron emission from metal surfaces exposed to ultrafast laser pulses. *Sov. Phys. JETP*, 39:375, 1974.
- [54] Edward D. Palik, editor. *Handbook of Optical Constants of Solids, Volume 2*. Academic Press, 1991.
- [55] R.L. Morse and C.W. Nielson. Occurrence of highenergy electrons and surface expansion in laserheated target plasmas. *Phys. Flu.*, 16:909, 1973.
- [56] Y.T. Lee and R.M. More. An electron conductivity model for dense plasmas. *Phys. Fluids.*, 27:1273, 1984.
- [57] S.I. Anisimov and B. Rethfeld. On the theory of ultrashort laser pulse interaction with a metal. *Proc. SPIE*, 3093:192, 1997.
- [58] V. Schmidt, W. Husinsky, and G. Betz. Ultrashort laser ablation of metals: pumpprobe experiments, the role of ballistic electrons and the two-temperature model. *Appl. Surf. Sci.*, 197-198:145, 2002.
- [59] Z. Chen, B. Holst, S.E. Kirkwood, V. Sametoglu, M. Reid, Y.Y. Tsui, V. Recoules, and A. Ng. Evolution of ac Conductivity in Nonequilibrium Warm Dense Gold. *Phys. Rev. Lett.*, 110:135001, 2013.
- [60] V. Recoules and J.-P. Crocombette. Ab initio determination of electrical and thermal conductivity of liquid aluminum. *Phys. Rev. B*, 72:104202, 2005.
- [61] S.K. Sundaram and E. Mazur. Inducing and probing non-thermal transitions in semiconductors using femtosecond laser pulses. *Nat. Mat.*, 1: 217, 2002.

- [62] D.M. Fritz, D. A. Reis, B. Adams, R. A. Akre, J. Arthur, C. Blome, P. H. Bucksbaum, A. L. Cavalieri, S. Engemann, S. Fahy, R. W. Falcone, and *et.al.* Ultrafast Bond Softening in Bismuth: Mapping a Solids Interatomic Potential with X-rays. *Science*, 315:633, 2007.
- [63] N.M. Bulgakova, R. Stoian, A. Rosenfeld, I.V. Hertel, and W. Marine E.E.B. Campbell. A general continuum approach to describe fast electronic transport in pulsed laser irradiated materials: The problem of Coulomb explosion. *Appl. Phys. A*, 81:345, 2005.
- [64] V. Recoules, J. Clerouin, G. Zerah, P.M. Anglade, and S. Mazevet. Effect of Intense Laser Irradiation on the Lattice Stability of Semiconductors and Metals. *Phys. Rev. Lett.*, 96:055503, 2006.
- [65] A. Ng, D. Parfeniuk, and L. DaSilva. Hugoniot Measurements for Laser-Generated Shock Waves in Aluminum. *Phys. Rev. Lett.*, 54:2064, 1985.
- [66] F. Perrot and M.W.C. Dharma-wardana. Electrical Conductivity of a Dense Plasma. *Phys. Rev. A*, 72:3351, 1987.
- [67] S.L. Daraszewicz, Y. Giret, N. Naruse, Y. Murooka, J. Yang, D.M. Duffy, A.L. Shluger, and K. Tanimura. Structural dynamics of laser-irradiated gold nanofilms. *Phys. Rev. B*, 88:184101, 2013.
- [68] K. Widmann, G. Guethlein, M.E. Foord, R.C. Cauble, F.G. Patterson, D.F. Price, F.J. Rogers, P.T. Springer, R.E. Stewart, A. Ng, T. Ao, and A. Forsman. Interferometric investigation of femtosecond laser-heated expanded states. *Phys. Plasmas*, 8:3869, 2001.
- [69] E.D. Palik. *Handbook of Optical Constants of Solids*, volume 1. Academic Press, Orlando, 1985.
- [70] A.C. Thompson and D. Vaughan, editors. *X-RAY DATA BOOKLET*. Lawrence Berkeley National Laboratory, Berkeley, 2nd edition, 2001.

- [71] M.J. Berger, J.S. Coursey, M.A. Zucker, and J. Chang. Stopping-power and range tables for electrons, protons, and helium ions, March 2014. URL <http://www.nist.gov/pml/data/star/>.
- [72] R.W. Schoenlein, W.Z. Lin, J.G. Fujimoto, and G. L. Eesley. Femtosecond Studies of Nonequilibrium Electronic Processes in Metals. *Phys. Rev. Lett.*, 58:1680, 1987.
- [73] S.D. Brorson, J. G. Fujimoto, , and E. P. Ippen. Femtosecond electron heat-transport dynamics in thin gold films. *Phys. Rev. Lett.*, 59:1962, 1987.
- [74] T. Juhasz, H.E. Elsayed-Ali, G.O. Smith, C. Suarez, and W.E. Bron. Direct measurements of the transport of nonequilibrium electrons in gold films with different crystal structures. *Phys. Rev. B*, 48:15488, 1993.
- [75] J. Hohlfeld, J.G. Müller, S.-S.Wellershoff, and E. Matthias. Time-resolved thermorefectivity of thin gold films and its dependence on film thickness. *Appl. Phys. B*, 64:387, 1997.
- [76] C. Suarez, W. E. Bron, and T. Juhasz. Dynamics and Transport of Electronic Carriers in Thin Gold Films. *Phys. Rev. Lett.*, 24:4536, 1995.
- [77] X. Liu, R. Stock, and W. Rudolph. Ballistic electron transport in Au films. *Phys. Rev. B*, 72:195431, 2005.
- [78] N. Gozlan, U. Tisch, and H. Haick. Tailoring the Work Function of Gold Surface by Controlling Coverage and Disorder of Polar Molecular Monolayers. *J. Phys. Chem. C*, 112:12988, 2008.
- [79] P. Zhu, Z. Zhang, L. Chen, J. Zheng, R. Li, W. Wang, J. Li, X. Wang, J. Cao, D. Qian, Z. Sheng, and J. Zhang. Four-dimensional imaging of the initial stage of fast evolving plasmas. *Appl. Phys. Lett.*, 97:211501, 2010.

- [80] T.T. Ho, M. Gupta, F.R. Chowdhury, Z Chen, and YY Tsui. Fabrication and characterization of freestanding ultrathin diamond-like carbon targets for high-intensity laser applications. *Appl. Phys. B*, 113:429, 2013.
- [81] M. Born and E. Wolf. *Principles of Optics*. Cambridge University Press, 7th edition, 1999.
- [82] D. Strickland and G. Mourou. Compression of amplified chirped optical pulses. *Opt. Commun.*, 56:219, 1985.
- [83] J.N. Sweetser, D.N. Fittinghoff, and R. Trebino. Transient-grating frequency-resolved optical gating. *Opt. Lett.*, 22:519, 1997.
- [84] Q. Zhang E.J. Brown and M. Dantus. Femtosecond transient-grating techniques: Population and coherence dynamics involving ground and excited states. *J. Chem. Phys.*, 110:5772, 1999.
- [85] R. Trebino, K.W. DeLong, D.N. Fittinghoff, J.N. Sweetser, M.A. Krumbugel, B.A. Richman, and D.J. Kane. Measuring ultrashort laser pulses in the time-frequency domain using frequency-resolved optical gating. *Rev. Sci. Instrum.*, 68:3277, 1997.
- [86] D.J. Kane and R. Trebino. Single-shot measurement of the intensity and phase of an arbitrary ultrashort pulse by using frequency-resolved optical gating. *Opt. Lett.*, 18:823, 1993.
- [87] K. W. DeLong, Rick Trebino, and D.J. Kane. Comparison of ultrashort-pulse frequency-resolved-optical-gating traces for three common beam geometries. *J. Opt. Soc. Am. B*, 5:1595, 1994.
- [88] J.-P. Geindre, P. Audebert, S. Rebibo, and J.-C. Gauthier. Single-shot spectral interferometry with chirped pulses. *Opt. Lett.*, 26:1612, 2001.
- [89] K.Y. Kim, I. Alexeev, and H.M. Milchberg. Single-shot supercontinuum spectral interferometry. *Appl. Phys. Lett.*, 81:4124, 2002.

- [90] E. Tokunaga, A. Terasaki, and T.Kobayashi. Femtosecond phase spectroscopy by use of frequency-domain interference. *J. Opt. Soc. Am. B*, 12:753, 1995.
- [91] A. Ng, D. Parfeniuk, P. Celliers, L. DaSilva, R.M. More, and Y.T.Lee. Electrical Conductivity of a Dense Plasma. *Phys. Rev. Lett*, 57:1595, 1986.
- [92] A.W. DeSilva and H.-J. Kunze. Experimental study of the electrical conductivity of strongly coupled copper plasmas. *Phys. Rev. E*, 49:4448, 1994.
- [93] A.W. DeSilva and H.-J. Kunze. Electrical conductivity of dense copper and aluminum plasmas. *Phys. Rev. E*, 57:5945, 1998.
- [94] M.P. Desjarlais, J.D. Kress, and L.A. Collins. Electrical conductivity for warm, dense aluminum plasmas and liquids. *Phys. Rev. E*, 66:025401(R), 2002.
- [95] Z. Chen, V. Sametoglu, T. Ao, Y.Y. Tsui, and A. Ng. Flux-Limited Nonequilibrium Electron Energy Transport in Warm Dense Gold. *Phys. Rev. Lett.*, 108:165001, 2012.
- [96] M-L. Theye. Investigation of the Optical Properties of Au by Means of Thin Semitransparent Films. *Phys. Rev. B*, 8:3060, 1970.
- [97] F. Seitz. *The Modern Theory of Solids*. McGraw-Hill, New York, 1940.
- [98] M.S. Safronova J. Mitroy and C.W. Clark. Theory and applications of atomic and ionic polarizabilities. *J. Phys. B: At. Mol. Opt. Phys.*, 43: 202001, 2010.
- [99] T.M. Miller. Atomic and molecular polarizabilities. In *CRC Handbook of Chemistry and Physics*. CRC Press, Boca Baton, FL, 94th edition, 2013.

- [100] R. Canfield, G. Hass, and W.R. Hunter. The Optical Properties of Evaporated Gold in The Vacuum Ultraviolet from 300 Å to 2000 Å. *J. Phys.*, 25:124, 1964.
- [101] H.-J. Hagemann, W. Gudat, and C. Kunz. Optical constants from the far infrared to the x-ray region: Mg, Al, Cu, Ag, Au, Bi, C, and Al₂O₃. *J. Opt. Soc. Am.*, 65:742, 1975.
- [102] P.O. Nilson. Electronic structure of disordered alloys: optical and photoemission measurements on Ag-Au and Cu-Au alloys. *Phys. Kondens. Materie*, 11:1, 1970.
- [103] M.V. Zombeck, G.K. Austin, and D.T. Torgerson. *Smithsonian Astrophysical Observatory Report SAO-AXAF-90-003, Appendix B, Table B1*. Cambridge, Massachusetts,, 1980.
- [104] R.C. Malone, R.L. McCrory, and R.L. Morse. Indication of Strongly Flux-limited Electron Transportation in Laser Target Experiment. *Phys. Rev. Lett.*, 34:721, 1975.
- [105] A.R. Bell, R.G. Evans, and D.J. Nicholas. Electron Energy Transport in Steep Temperature Gradients in Laser-Produced Plasmas. *Phys. Rev. Lett.*, 46:243, 1981.
- [106] J.P. Matte and J. Virmont. Electron Heat Transport down Steep Temperature Gradients. *Phys. Rev. Lett.*, 49:1935, 1982.
- [107] X. Gonze and C. Lee. Dynamical matrices, Born effective charges, dielectric permittivity tensors, and interatomic force constants from density-functional perturbation theory. *Phys. Rev. B*, 55:10355, 1997.
- [108] G. Cordoba and C. R. Brook. The Heat Capacity of Gold from 300 to 1200 K: Experimental data and analysis of contributions. *Phys. Stat. Sol. (a)*, 6:581, 1971.

- [109] A.-T. Petit and P.-L. Dulong. Recherches sur quelques points importants de la Theorie de la Chaleur. *Annales de Chimie et de Physique*, 10:395, 1819.
- [110] X. Gonze, B. Amadon, P.-M. Anglade, J.-M. Beuken, F. Bottin, P. Boulanger, F. Bruneval, D. Caliste, R. Caracas, M. Cote, and et. al. ABINIT: First-principles approach to material and nanosystem properties. *Comput. Phys. Commun.*, 180:2582, 2009.
- [111] F. Bottin, S. Leroux, A. Knyazev, and Gilles Zerah. Large-scale ab initio calculations based on three levels of parallelization. *Comput. Mat. Sci.*, 42:329, 2008.
- [112] P. Hohenberg and W. Kohn. Inhomogeneous Electron Gas. *Phys. Rev.*, 136:B864, 1964.
- [113] W. Kohn and L. Sham. Self-Consistent Equations Including Exchange and Correlation Effects. *Phys. Rev.*, 140:A1133, 1965.
- [114] P. E. Blochl. Projector augmented-wave method. *Phys. Rev. B*, 50:17935, 1994.
- [115] M. Torrent, F. Jollet, F. Bottin, G. Zerah, and X. Gonze. Implementation of the projector augmented-wave method in the ABINIT code: Application to the study of iron under pressure. *Comput. Mat. Sci.*, 42:337, 2008.
- [116] S. I. Anisimov, B. L. Kapeliovich, and T. L. Perelman. Thermal response of metals to ultrashort pulse laser excitation. *Phys. Rev. Lett.*, 61:2886, 1988.
- [117] S.D. Brorson, A. Kazeroonian, S. Moodera, D. W. Face, T.K. Cheng, E.P. Ippen, M.S. Dresselhaus, and G. Dresselhaus. Femtosecond Room-

- Temperature Measurement of the Electron-Phonon Coupling Constant λ in Metallic Superconductors. *Phys. Rev. Lett.*, 64:2172, 1990.
- [118] P.B. Allen. Theory of Thermal Relaxation of Electrons in Metals. *Phys. Rev. Lett.*, 59:1460, 1987.
- [119] X.Y. Wang, D.M. Riffe, Y.-S. Lee, and M. C. Downer. Time-resolved electron-temperature measurement in a highly excited gold target using femtosecond thermionic emission. *Phys. Rev. B*, 50:8016, 1994.
- [120] W.L. McMillian. Transition Temperature of Strong-Coupled Superconductors. *Phys. Rev.*, 167:331, 1968.
- [121] G.F. Naterer and J.A. Camberos. *Entropy Based Design and Analysis of Fluids Engineering Systems, Appendix, Table A2*. CRC Press, 2008.
- [122] R. Kubo. Statistical-Mechanical Theory of Irreversible Processes. I. General Theory and Simple Applications to Magnetic and Conduction Problems. *J. Phys. Soc. Jpn.*, 12:570, 1957.
- [123] D.A. Greenwood. The Boltzmann Equation in the Theory of Electrical Conduction in Metals. *Proc. Phys. Soc.*, 71:585, 1958.
- [124] W.A. Harrison. *Solid state theory*. Dover Publications, unabridged and corr. republication. edition.
- [125] H.J. Monkhorst and J.D. Pack. Special points for Brillouin-zone integrations. *Phys. Rev. B*, 13:5188, 1976.
- [126] F. Lambert, V. Recoules, Alain Decoster, J. Clerouin, and M. Desjarlais. On the transport coefficients of hydrogen in the inertial confinement fusion regime. *Phys. Plasmas*, 18:056306, 2011.

- [127] M. Pozzo, M.P. Desjarlais, and Dario Alfe. Electrical and thermal conductivity of liquid sodium from first-principles calculations. *Phys. Rev. B*, 84:054203, 2011.
- [128] T. Rangel, D. Kecik, P.E. Trevisanutto, G.-M. Rignanese, H. Van Swygenhoven, and V. Olevano. Band structure of gold from many-body perturbation theory. *Phys. Rev. B*, 86:125125, 2012.
- [129] M. W. C. Dharma-wardana and F. Perrot. Energy relaxation and the quasiequation of state of a dense two-temperature nonequilibrium plasma. *Phys. Rev. E*, 58:3705, 1998. and erratum.
- [130] J. Vorberger and D. O. Gericke. Theory of electron-ion energy transfer applied to laser ablation. *AIP Conf. Proc.*, 1464:572, 2012.
- [131] C.W. Siders, A. Cavalleri, K. Sokolowski-Tinten, Cs. Toth, T. Guo, M. Kammler, M. Horn von Hoegen, K.R. Wilson, D. von der Linde, and C.P.J. Barty. Detection of Nonthermal Melting by Ultrafast X-ray Diffraction. *Science*, 286:1340, 1999.
- [132] B.J. Siwick, J.R. Dwyer, R.E. Jordan, and R.J. Dwayne Miller. An Atomic-Level View of Melting Using Femtosecond Electron Diffraction. *Science*, 302:1382, 2002.
- [133] C. Kittel. *Introduction to Solid State Physics*. John Wiley and Sons, sixth edition, 1986.
- [134] E. van de Riet, H. Derks, and W. Heiland. Observation of Pre-phase Transitional Phenomena on an Au(110) Surface. *Surf. Sci.*, 53:234, 1990.
- [135] J.C. Campuzano, G. Jennings, and R.F. Willis. The Critical Exponents of The Au(110) (I 2)-(I 1) Phase Transition. *Surf. Sci.*, 62:484, 1985.

- [136] S.E. Kirkwood. *Characterization of metal and semiconductor nanomilling at near threshold intensities using femtosecond laser pulses*. PhD thesis, University of Alberta, 2007.
- [137] J.M. Liu. Simple technique for measurements of pulsed Gaussian-beam spot sizes. *Opt. Lett.*, 7:196, 1981.
- [138] K. Furusawa, K. Takahashi, H. Kumagai, K. Midorikawa, and M. Obara. Ablation characteristics of Au, Ag, and Cu metals using a femtosecond Ti:sapphire laser. *Appl. Phys. A*, 69:S359, 1999.
- [139] H.Jr. Dutton. *Understanding optical communications*. Prentice Hall, 1998.
- [140] D.A.B. Miller. Device Requirements for Optical Interconnects to Silicon Chips . *Proc. IEEE*, 97:1185, 2009.
- [141] D.A.B. Miller. Optical interconnects to electronic chips. *Appl. Opt.*, 49:F59, 2010.
- [142] J.S. Orcutt, B. Moss, C. Sun, J. Leu, M. Georgas, J. Shainline, E. Zraggen, H. Li, Jie Sun, and *et.al.* Open foundry platform for high-performance electronic-photonic integration. *Opt. Exp.*, 20:12222, 2012.
- [143] V.R. Almeida and R.R. Panepucci. *VLSI Micro-and Nanophotonics: Science, Technology, and Applications*, chapter 4. Silicon Micro-Ring Resonator Structures: Characteristics and Applications. CRC Press, Boca Raton, Florida, 2011.
- [144] I. Chremmos, O. Schwelb, and N. Uzunoglu, editors. *Photonic Microresonator Research and Applications*. Springer, 2010.
- [145] A.M. Prabhu, A.Tsay, Z. Han, and V. Van. Ultracompact SOI Microring AddDrop Filter With Wide Bandwidth and Wide FSR. *IEEE Photon. Technol. Lett.*, 21:651, 2009.

- [146] W.A. Zortman, D. C. Trotter, and M. R. Watts. Silicon photonics manufacturing. *Opt. Express*, 18:23598, 2010.
- [147] A.V. Krishnamoorthy, X. Zheng, G. Li, J. Yao, T. Pinguet, A. Mekis, H. Thacker, I. Shubin, Y. Luo, K. Raj, and J. E. Cunningham. Exploiting cmos manufacturing to reduce tuning requirements for resonant optical devices. *IEEE Photon. J.*, 3:567, 2011.
- [148] P. Dong, W. Qian, H. Liang, R. Shafiha, N.N. Feng, D. Feng, X. Zheng, A. V. Krishnamoorthy, and M. Asghari. Low power and compact reconfigurable multiplexing devices based on silicon microring resonators. *Opt. Express*, 18:9852, 2010.
- [149] H.Y. Ng, M. R. Wang, D. Li, X. Wang, J. Martinez, R. R. Panepucci, and K. Pathak. 44 wavelength- reconfigurable photonic switch based on thermally tuned silicon microring resonators. *Opt. Eng.*, 47:044601, 2008.
- [150] L. Zhou, K. Okamoto, and S. J. B. Yoo. Athermalizing and trimming of slotted silicon microring resonators with uv-sensitive pmma upper-cladding. *IEEE Photon. Technol. Lett.*, 21:1175, 2009.
- [151] A. Canciamilla, F. Morichetti, S. Grillanda, M. Sorel P. Velha, V. Singh, A. Agarwal, L. C. Kimerling, and A. Melloni. Athermalizing and trimming of slotted silicon microring resonators with uv-sensitive pmma upper-cladding. *Opt. Express*, 24:15807, 2012.
- [152] Y. Shen, I. B. Divliansky, D. N. Basov, and S. Mookherjea. Electric-field-driven nano-oxidation trimming of silicon microrings and interferometers. *Opt. Lett.*, 36:2668, 2011.
- [153] J. Bonse, S. Baudach, J. Krüger, W. Kautek, and M. Lenzner. Femtosecond laser ablation of silicon–modification thresholds and morphology. *Appl. Phys. A*, 74:19, 2002.

- [154] J. Bonse, K.-W. Brzezinka, and A.J. Meixner. Modifying single-crystalline silicon by femtosecond laser pulses: an analysis by micro Raman spectroscopy, scanning laser microscopy and atomic force microscopy. *Appl. Surf. Sci.*, 221:215, 2004.
- [155] W.J. Liu, S. Chen, H.Y. Cheng, J.D. Lin, and S.L. Fu. Fabrication of amorphous silicon films for arrayed waveguide grating application. *Surf. Coat. Tech.*, 201:6581, 2007.
- [156] M.J.A. de Dood, A. Polman, T. Zijlstra, and E.W.J.M. van der Drift. Amorphous silicon waveguides for microphotronics. *J. Appl. Phys.*, 92:649, 2002.
- [157] D. Bachman, Z. Chen, A.M. Prabhu, R. Fedosejevs, Y.Y. Tsui, and V. Van. Femtosecond laser tuning of silicon microring resonators. *Opt. Lett.*, 36:4695, 2011.
- [158] A.P. Masilamani. *Advanced Silicon Microring Resonator Devices for Optical Signal Processing*. PhD thesis, University of Alberta, 2012.
- [159] S. Koc, M. Zvtov, and J. Zemek. Physical properties of amorphous silicon: The role of annealing. *J. Phys. B*, 25:83, 1975.
- [160] E. Korin, R. Reif, and B. Mikic. Crystallization of amorphous silicon films using a multistep thermal annealing process. *Thin Solid Films*, 167:101, 1988.
- [161] J.E. Fredrickson, C.N. Waddell, W.G. Spitzer, and G. K. Hubler. Effects of thermal annealing on the refractive index of amorphous silicon produced by ion implantation. *Appl. Phys. Lett.*, 40:172, 1982.
- [162] Y. Izawa, S. Tokita, M. Fujita, M. Nakai, T. Norimatsu, and Y. Izawa. Ultrathin amorphization of single-crystal silicon by ultraviolet femtosecond laser pulse irradiation. *J. Appl. Phys.*, 105:064909, 2009.

- [163] Y. Izawa, S. Tokita, M. Fujita, T. Norimatsu, and Y. Izawa. Ultra fast melting process in femtosecond laser crystallization of thin a-Si layer. *Appl. Sur. Sci.*, 255:9764, 2009.
- [164] W. Liu, J.-F. Gravel, F. Theberge, A. Becker, and S.L. Chin. Background reservoir: its crucial role for long-distance propagation of femtosecond laser pulses in air. *Appl. Phys. B*, 80:587, 2005.
- [165] S. Bohman, A. Suda, M. Kaku, M. Nurhuda, T. Kanai, S. Yamaguchi, and K. Midorikawa. Generation of 5 fs, 0.5 TW pulses focusable to relativistic intensities at 1 kHz. *Opt. Exp.*, 16:10684, 2008.
- [166] T.L. Cocker, V. Jelic, M. Gupta, S.J. Molesky, J.A.J. Burgess, G.D.L. Reyes¹, L.V. Titova, Y.Y. Tsui, M.R. Freeman, and F.A. Hegmann. An ultrafast terahertz scanning tunnelling microscope. *Nat. Photonics*, 7: 620, 2013.
- [167] M. Walther, D.G. Cooke, C. Sherstan, M. Hajar, M.R. Freeman, and F.A. Hegmann. Terahertz conductivity of thin gold films at the metal-insulator percolation transition. *Phys. Rev. B*, 76:125408, 2007.
- [168] K.Y. Kim, B. Yellampalle, J.H. Glowia, A.J. Taylor, and G. Rodriguez. Measurements of Terahertz Electrical Conductivity of Intense Laser-Heated Dense Aluminum Plasmas. *Phys. Rev. Lett.*, 100:135002, 2008.

Appendix A

Tuning a Silicon Microring Resonators with Multiple Laser Shots on Same Area

Femtosecond laser tuning of silicon microring resonators

Daniel Bachman,* Zhijiang Chen, Ashok M. Prabhu, Robert Fedosejevs, Ying Y. Tsui, and Vien Van

Department of Electrical and Computer Engineering, University of Alberta, Edmonton, Alberta T6G 2V4, Canada

*Corresponding author: bachman@ualberta.ca

Received September 30, 2011; revised November 1, 2011; accepted November 1, 2011;
posted November 2, 2011 (Doc. ID 155685); published December 1, 2011

Femtosecond laser modification is demonstrated as a possible method for postfabrication tuning of silicon microring resonators. Single 400nm femtosecond laser pulses were used to modify the effective index of crystalline silicon microring waveguides by either amorphization or surface nanomilling depending on the laser fluence. Both blue- and redshifts in the microring resonance could be achieved without imparting significant degradation to the device quality factor. © 2011 Optical Society of America

OCIS codes: 230.5750, 230.3120.

Silicon integrated photonics has emerged over the past decade as an attractive platform for integrated optic devices due to its compatibility and potential for integration with complementary metal oxide semiconductor electronics. Progress in silicon photonic fabrication technology has substantially improved our ability to control device dimensions down to the nanometer scale level [1]. Nevertheless, due to the extreme sensitivity of silicon photonic devices to small variations in the waveguide dimensions and material refractive indices, fabricated devices typically exhibit responses that deviate from designed performance. This is an especially great challenge for optical devices based on microring resonators, whose resonances are required to be accurately aligned for proper device operation. Typically a postfabrication trimming technique is employed to correct for the deviations in the microring resonances due to fabrication imperfections.

The most common approach for postfabrication tuning of silicon microring resonators is to change the refractive index of silicon via the thermo-optic effect. This is usually accomplished by placing microheaters above the microrings and using resistive heating to actively change the temperature of the waveguides [2]. The disadvantages of this method are the extra processing steps required to fabricate the heaters and the constant power that needs to be applied to the heaters. For this reason it is more desirable to have a simple method that can permanently change the microring resonances. Several different permanent tuning approaches have been proposed, including index trimming of microring claddings made of materials sensitive to UV or visible light [3,4], electron beam induced compaction and strain of an SiO₂ microring cladding [5], and nanoscale oxidation of the silicon microring waveguide [6]. While some of these methods can be used to finely tune the microring resonances, they also suffer from several limitations such as limited tuning range and the restriction of tuning the resonance in only one direction.

In this Letter we demonstrate the feasibility of postfabrication tuning of a silicon microring resonator by femtosecond laser modification of the surface morphology of the silicon waveguide. When a silicon surface is illuminated with a femtosecond laser pulse, its surface can be modified differently depending on the laser fluence [7]. Specifically, at high laser fluences nanomilling takes place, in which a thin layer of silicon is ablated from

the surface. At lower laser fluences, no material is removed but a thin layer of crystalline silicon (c-Si) at the surface is converted into amorphous silicon (a-Si) in a process called amorphization. Here we exploit both of these mechanisms to tune the resonance of a silicon microring resonator in both directions, i.e., toward longer and shorter wavelengths. Ablation from the surface decreases the height of the waveguide, causing a decrease in the microring effective index, which induces a blue-shift in the resonance. Alternatively, modification to the crystal structure of silicon from c-Si to a-Si will cause an increase in the effective index of the waveguide, thereby inducing a redshift in the microring resonance.

A Ti:sapphire (Spectra-Physics Hurricane) laser was used for our study to generate single ~130fs pulses (FWHM, assuming a Gaussian pulse shape) at 800 nm. This fundamental pulse was then frequency doubled by a BiBO nonlinear crystal to provide 400 nm pulses. To ensure that only the 400 nm laser pulses were used to modify our sample, a 2 mm thick Schott BG39 filter was used to attenuate the 800 nm component. The skin depth of 400 nm pulses in silicon is ~164 nm. The experimental setup used for this experiment is shown in Fig. 1. In order to obtain uniform modification of the ring resonator, a “top-hat” beam image instead of a Gaussian focal spot was formed on the sample surface. This top-hat beam

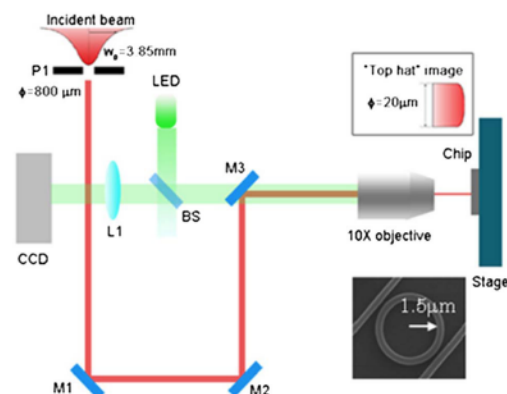


Fig. 1. (Color online) Experimental setup of femtosecond laser tuning of a silicon microring resonator. The device is shown in the SEM image. (M1, M2, and M3, 400 nm high-reflectivity dielectric mirrors; L1, achromatic lens; BS, beam splitter.)

was obtained by demagnified imaging of the center part of a Gaussian beam selected with a hard pinhole aperture (P1), where the intensity distribution is close to uniform. Our sample is mounted on a computer-controlled 3D motion stage. For real-time positioning of the sample, a green light LED is used to illuminate the target surface, and the device is monitored by a CCD camera.

The microring resonator used in the experiment was an add/drop filter with a radius of $1.5\ \mu\text{m}$. The microring waveguide was air clad with cross-sectional dimensions of $340\ \text{nm} \times 300\ \text{nm}$ [8]. The device was fabricated using electron beam lithography on an SOI chip with a $1\ \mu\text{m}$ thick buried oxide layer. An SEM picture of the device is shown in Fig. 1. The device had a free spectral range of $52\ \text{nm}$ and supported only the TM mode [8].

We started the experiment with laser shots set at a low fluence of about $0.07\ \text{J}/\text{cm}^2$, which was slightly above the point of visual changes caused by the pulse to a blank silicon substrate. The laser energy was then gradually increased throughout the experiment to a fluence of about $0.22\ \text{J}/\text{cm}^2$. However, due to a small uncertainty in the laser energy from shot to shot, the shot fluence did not always increase monotonically (as seen in Fig. 2). After every laser shot, the drop port response of the microring resonator was measured using a $1500\text{--}1600\ \text{nm}$ tuneable laser with the polarization set to TM. Figure 2 shows a plot of the shot-to-shot relative resonance shift versus the laser fluence for the two resonances initially at $1516.10\ \text{nm}$ and $1567.56\ \text{nm}$. Both positive (red) and negative (blue) shifts are observed. The inset in Fig. 2 shows the drop port spectral responses at the $1567\ \text{nm}$ resonance before (shot 0) and after (shot 17) the experiment. The plot shows that over the course of the experiment, the peak position of the microring resonance originally at $1567.56\ \text{nm}$ experienced a net blueshift of $4.5\ \text{nm}$, originally redshifting $14.5\ \text{nm}$ before being blueshifted back $19\ \text{nm}$. This is among the largest shifts achieved for silicon microring resonators using a permanent tuning method [3–6].

Two distinct modes of operation are discernible from Fig. 2, one for laser fluences below about $0.20\ \text{J}/\text{cm}^2$ and one above this threshold. In the mode of operation below $0.20\ \text{J}/\text{cm}^2$, only redshifts in the resonances were observed. These shifts correspond to a change on the order

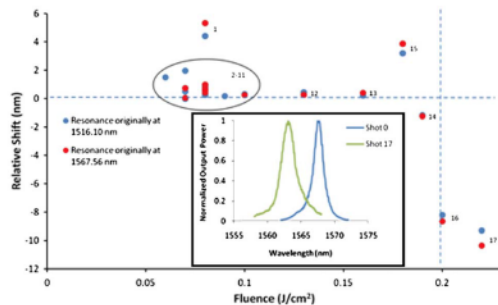


Fig. 2. (Color online) Relation between the incident femtosecond laser fluence and the relative resonance shift observed from shot to shot. Data points are labeled with their sequential shot number on the microring used. Inset, microring resonance at $1567\ \text{nm}$ before and after the experiment.

of 1×10^{-3} in the index of refraction of the silicon waveguide core. The most likely physical mechanism for this change is a conversion of a thin layer of crystalline silicon ($n \approx 3.478$ at $1550\ \text{nm}$ [9]) at the top waveguide surface to amorphous silicon ($n \approx 3.48$ at $1550\ \text{nm}$ [9]). From a single laser shot experiment on a blank Si substrate [10], it was reported that this amorphous layer is about $50\ \text{nm}$ thick using $800\ \text{nm}$ laser pulses. The conversion from c-Si to a-Si results in an increase in the effective index of the waveguide, which would cause the redshift in the resonance observed. In the mode of operation above the $0.20\ \text{J}/\text{cm}^2$ threshold, only blueshifts in the resonances were observed. The most likely physical mechanism responsible for the blueshifts is laser ablation of the surface of the waveguide. The ablation would cause a decrease in the height of the waveguide, resulting in a decrease in the effective index of the waveguide, thereby causing a blueshift in the resonance. The blueshifts of approximately $8\text{--}10\ \text{nm}$ are consistent with simulation results for approximately a $2\text{--}3\ \text{nm}$ decrease in the waveguide height in the microring waveguide.

Figure 2 shows that much larger redshifts were obtained for shots 1 and 15 compared to the other shots in the low fluence region, implying that there was a much higher amount of c-Si converted to a-Si for these two particular shots. Indeed for the first shot, there would be the highest amount of crystalline silicon available at the waveguide surface for conversion to a-Si, so it is reasonable that the initial shot would cause a larger redshift in the microring resonance than subsequent shots with an even higher fluence. For shot 15, we note that it followed shot 14, which had likely removed a layer of material on the microring surface due to ablation, because a blueshift was obtained. It was reported in [9] that when the laser fluence is above the ablation threshold, the molten silicon on the surface has enough time to cool and form polycrystalline silicon instead of amorphous silicon. Thus, following shot 14, the microring surface had recrystallized so that more c-Si was available to be converted to a-Si during shot 15. This could explain the large redshift in the resonance observed for this shot.

To confirm the physical origins for the red- and blue-shift regimes of operation, atomic force microscopy (AFM) scans of the microring were taken before shot 13 and after shot 17. Figure 3 displays the results of two of these scans. Figure 3(a) shows the microring after laser shots with a fluence of no more than $0.15\ \text{J}/\text{cm}^2$. The image shows no variations or patterns on the silicon surface as a result of the laser shots. However, the AFM scan in Fig. 3(b) obtained at the end of the experiment shows

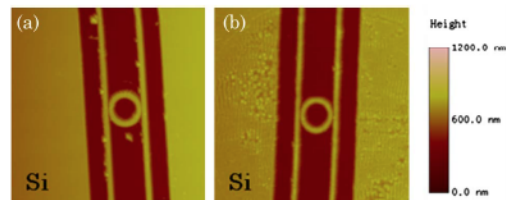


Fig. 3. (Color online) AFM images of the microring after multiple shots with (a) incident fluence no more than $0.15\ \text{J}/\text{cm}^2$ and (b) after the end of the experiment.

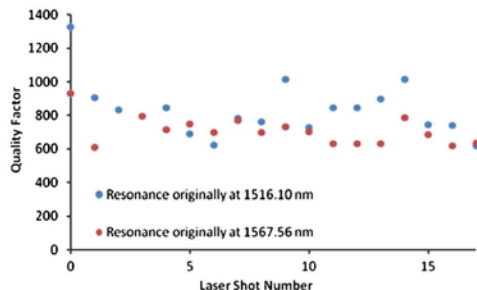


Fig. 4. (Color online) Extrinsic quality factor of the $1.5\text{ }\mu\text{m}$ microring measured after each laser shot.

that periodic ripples have materialized on the silicon surface to the left and right of the microring device. These surface ripples have a period that is on the order of the wavelength of the laser and are indicative that ablation has occurred [7]. Thus, the AFM scans support our hypothesis for the physical origins of the red- and blueshifts observed. Because a fluence of about 0.20 J/cm^2 separates the amorphization regime from the ablation regime, it allows us to define this fluence to be the ablation threshold of our silicon device. This value is comparable with the ablation threshold reported in the literature for multishot ablation experiments on flat silicon wafers using 800 nm pulses [7].

We also monitored the quality factor of the microring resonator after each shot to ensure that the device response was not significantly degraded during the tuning. Figure 4 shows a plot of the extrinsic quality factor of the microring measured at both resonances after each shot. The plot shows that there was some drop in the quality factor of the resonator after the first shot, after which very little degradation occurred, even as the microring was ablated after shot 16. The decrease in the quality factor after the initial shot can be attributed to the increased absorption in the a-Si layer compared to c-Si as well as increased roughness caused by the amorphization of an initially smooth c-Si surface. Subsequent shots did not seem to incur additional roughness, as seen from the relatively constant quality factor after shot 1. The quality factor of the microring resonator used in this study was relatively low owing to its small size, so further study would be required to examine how femtosecond laser surface modification would affect the loss of a high- Q resonator.

In terms of stability, the resonance wavelengths of the ablated microring were observed to change by $10\text{--}20\text{ pm}$ over a period of several weeks. However, this change is also observed for a typical Si microring resonator without ablation and is normally attributed to the formation of a thin native oxide layer on the silicon waveguide core.

In summary, we demonstrated the feasibility of using femtosecond laser modification of silicon waveguides for

postfabrication tuning of silicon microring resonators. Both blue- and redshifts of the microring resonances could be achieved with single laser shots without causing significant degradation to the device response. The technique has several advantages over previous techniques for silicon microring tuning in that it does not require extra fabrication steps and is operationally much faster than other demonstrated techniques. The setup is relatively simple, and the technique provides a much larger tuning range. We believe the method may also be used to tune silicon microring resonators with a cladding such as SiO_2 , provided that the cladding is transparent to 400 nm femtosecond laser pulses. In this case tuning would be achieved by amorphization of the Si waveguide. While relatively coarse tuning of the microring resonance was demonstrated with single laser shots, fine tuning may also be possible by shooting only a small section of the microring to lessen the impact of each shot. We also note that the method can also be applied to fine tune the performance of other silicon photonic devices, such as gratings and Mach-Zehnder interferometers. Finally, because the resonance of a microring resonator is very sensitive to small modifications to the waveguide surface, the device could serve as a sensor for accurately determining the ablation threshold and can be used for studying the dynamics of femtosecond ablation by *in situ* monitoring of the resonance shifts.

This work is supported by the Natural Sciences and Engineering Research Council of Canada (NSERC) and the Canadian Institute for Photonic Innovations.

References

1. S. Selvaraja, W. Bogaerts, P. Dumon, D. Van Thourhout, and R. Baets, *IEEE J. Sel. Top. Quantum Electron.* **16**, 316 (2010).
2. M. H. Khan, H. Shen, Y. Xuan, L. Zhao, S. Xiao, D. E. Leaird, A. M. Weiner, and M. Qi, *Nat. Photon.* **4**, 117 (2010).
3. L. Zhou, K. Okamoto, and S. J. B. Yoo, *IEEE Photon. Technol. Lett.* **21**, 1175 (2009).
4. A. Melloni, A. Canciamilla, C. Ferrari, S. Grillanda, F. Morichetti, P. Velha, M. Sorel, J. Hu, J. D. Musgraves, B. Zdyrko, I. Lazinov, K. Richardson, V. Singh, A. Agarwal, and L. Kimerling, in *Integrated Photonics Research, Silicon and Nanophotonics*, OSA Technical Digest (CD) (Optical Society of America, 2011), paper IMB1.
5. J. Schrauwen, D. V. Thourhout, and R. Baets, *Opt. Express* **16**, 3738 (2008).
6. Y. Shen, I. B. Divliansky, D. N. Basov, and S. Mookherjea, *Opt. Lett.* **36**, 2668 (2011).
7. J. Bonse, S. Baudach, J. Krüger, W. Kautek, and M. Lenzner, *Appl. Phys. A* **74**, 19 (2002).
8. A. M. Prabhu, A. Tsay, Z. Han, and V. Van, *IEEE Photon. J.* **2**, 436 (2010).
9. E. D. Palik, *Handbook of Optical Constants* (Academic, 1998).
10. J. Bonse, K.-W. Brzeinka, and A. J. Meixner, *Appl. Surf. Sci.* **221**, 215 (2004).

Appendix B

Controllable Tuning of a Silicon Mirroring Resonator

Permanent fine tuning of silicon microring devices by femtosecond laser surface amorphization and ablation

Daniel Bachman,^{*} Zhijiang Chen, Robert Fedosejevs, Ying Y. Tsui,
and Vien Van

Department of Electrical and Computer Engineering, University of Alberta, Edmonton, Alberta, T6G 2V4, Canada
**bachman@ualberta.ca*

Abstract: We demonstrate the fine tuning capability of femtosecond laser surface modification as a permanent trimming mechanism for silicon photonic components. Silicon microring resonators with a 15 μm radius were irradiated with single 400nm wavelength laser pulses at varying fluences. Below the laser ablation threshold, surface amorphization of the crystalline silicon waveguides yielded a tuning rate of $20 \pm 2 \text{ nm/J}\cdot\text{cm}^{-2}$ with a minimum resonance wavelength shift of 0.10nm. Above that threshold, ablation yielded a minimum resonance shift of -1.7nm . There was some increase in waveguide loss for both trimming mechanisms. We also demonstrated the application of the method by using it to permanently correct the resonance mismatch of a second-order microring filter.

©2013 Optical Society of America

OCIS codes: (130.7408) Wavelength filtering devices; (220.4241) Nanostructure fabrication; (230.5750) Resonators; (250.5300) Photonic integrated circuits.

References and links

1. W. Bogaerts, P. De Heyn, T. Van Vaerenbergh, K. De Vos, S. K. Selvaraja, T. Claes, P. Dumon, P. Bienstman, D. Van Thourhout, and R. Baets, "Silicon microring resonators," *Laser Photon. Rev.* 6(1), 47–73 (2012).
2. Y. Vlasov, W. M. J. Green, and F. Xia, "High-throughput silicon nanophotonic wavelength-insensitive switch for on-chip optical networks," *Nat. Photonics* 2(4), 242–246 (2008).
3. Q. Xu, S. Manipatruni, B. Schmidt, J. Shakya, and M. Lipson, "12.5 Gbit/s carrier-injection-based silicon microring silicon modulators," *Opt. Express* 15(2), 430–436 (2007).
4. S. Yamatogi, Y. Amemiya, T. Ikeda, A. Kuroda, and S. Yokoyama, "Si ring optical resonators for integrated on-chip biosensing," *Jpn. J. Appl. Phys.* 48(4), 04C188 (2009).
5. S. C. Buswell, V. A. Wright, J. M. Buriak, V. Van, and S. Evoy, "Specific detection of proteins using photonic crystal waveguides," *Opt. Express* 16(20), 15949–15957 (2008).
6. W. A. Zortman, D. C. Trotter, and M. R. Watts, "Silicon photonics manufacturing," *Opt. Express* 18(23), 23598–23607 (2010).
7. A. V. Krishnamoorthy, X. Zheng, G. Li, J. Yao, T. Pinguet, A. Mekis, H. Thacker, I. Shubin, Y. Luo, K. Raj, and J. E. Cunningham, "Exploiting CMOS manufacturing to reduce tuning requirements for resonant optical devices," *IEEE Photon. J.* 3(3), 567–579 (2011).
8. P. Dong, W. Qian, H. Liang, R. Shafiqi, N. N. Feng, D. Feng, X. Zheng, A. V. Krishnamoorthy, and M. Asghari, "Low power and compact reconfigurable multiplexing devices based on silicon microring resonators," *Opt. Express* 18(10), 9852–9858 (2010).
9. H. Y. Ng, M. R. Wang, D. Li, X. Wang, J. Martinez, R. R. Panepucci, and K. Pathak, "4×4 wavelength-reconfigurable photonic switch based on thermally tuned silicon microring resonators," *Opt. Eng.* 47, 044601 (2008).
10. L. Zhou, K. Okamoto, and S. J. B. Yoo, "Athermalizing and trimming of slotted silicon microring resonators with UV-sensitive PMMA upper-cladding," *IEEE Photon. Technol. Lett.* 21(17), 1175–1177 (2009).
11. A. Canciamilla, F. Morichetti, S. Grillanda, P. Velha, M. Sorel, V. Singh, A. Agarwal, L. C. Kimerling, and A. Melloni, "Photo-induced trimming of chalcogenide-assisted silicon waveguides," *Opt. Express* 20(14), 15807–15817 (2012).
12. J. Schrauwen, D. Van Thourhout, and R. Baets, "Trimming of silicon ring resonator by electron beam induced compaction and strain," *Opt. Express* 16(6), 3738–3743 (2008).
13. S. Prorok, A. Y. Petrov, M. Eich, J. Luo, and A. K. Y. Jen, "Trimming of high-Q-factor silicon ring resonators by electron beam bleaching," *Opt. Lett.* 37(15), 3114–3116 (2012).

14. C. J. Chen, J. Zheng, T. Gu, J. F. McMillan, M. Yu, G. Q. Lo, D. L. Kwong, and C. W. Wong, "Selective tuning of high-Q silicon photonic crystal nanocavities via laser-assisted local oxidation," *Opt. Express* **19**(13), 12480–12489 (2011).
15. Y. Shen, I. B. Divliansky, D. N. Basov, and S. Mookherjea, "Electric-field-driven nano-oxidation trimming of silicon microrings and interferometers," *Opt. Lett.* **36**(14), 2668–2670 (2011).
16. S. T. Chu, W. Pan, S. Sato, T. Kaneko, B. E. Little, and Y. Kokubun, "Wavelength trimming of a microring resonator filter by means of a UV sensitive polymer overlay," *IEEE Photon. Technol. Lett.* **11**(6), 688–690 (1999).
17. D. K. Sparacin, C. Y. Hong, L. C. Kimerling, J. Michel, J. P. Lock, and K. K. Gleason, "Trimming of microring resonators by photooxidation of a plasma-polymerized organosilane cladding material," *Opt. Lett.* **30**(17), 2251–2253 (2005).
18. U. Levy, K. Campbell, A. Groisman, S. Mookherjea, and Y. Fainman, "On-chip microfluidic tuning of an optical microring resonator," *Appl. Phys. Lett.* **88**(11), 111107 (2006).
19. D. Bachman, Z. Chen, A. M. Prabhu, R. Fedosejevs, Y. Y. Tsui, and V. Van, "Femtosecond laser tuning of silicon microring resonators," *Opt. Lett.* **36**(23), 4695–4697 (2011).
20. J. Bonse, "All-optical characterization of single femtosecond laser-pulse-induced amorphization in silicon," *Appl. Phys., A Mater. Sci. Process.* **84**(1-2), 63–66 (2006).
21. Y. Izawa, Y. Izawa, Y. Setsuhara, M. Hashida, M. Fujita, R. Sasaki, H. Nagai, and M. Yoshida, "Ultrathin amorphous Si layer formation by femtosecond laser pulse irradiation," *Appl. Phys. Lett.* **90**(4), 044107 (2007).
22. Y. Izawa, Y. Setuhara, M. Hashida, M. Fujita, and Y. Izawa, "Abaltion and amorphization of crystalline Si by femtosecond and picosecond laser irradiation," *Jpn. J. Appl. Phys.* **45**(7), 5791–5794 (2006).
23. Y. Izawa, S. Tokita, M. Fujita, M. Nakai, T. Norimatsu, and Y. Izawa, "Ultrathin amorphization of single-crystal silicon by ultraviolet femtosecond laser pulse irradiation," *J. Appl. Phys.* **105**(6), 064909 (2009).
24. W. J. Liu, S. Chen, H. Y. Cheng, J. D. Lin, and S. L. Fu, "Fabrication of amorphous silicon films for arrayed waveguide grating application," *Surf. Coat. Tech.* **201**(15), 6581–6584 (2007).
25. M. J. A. de Dood, A. Polman, T. Zijlstra, and E. W. J. M. van der Drift, "Amorphous silicon waveguides for microphotonic," *J. Appl. Phys.* **92**(2), 649–653 (2002).
26. B. E. Little, J. P. Laine, and S. T. Chu, "Surface-roughness-induced contradirectional coupling in ring and disk resonators," *Opt. Lett.* **22**(1), 4–6 (1997).
27. F. Morichetti, A. Canciamilla, M. Martinelli, A. Samarelli, R. M. De La Rue, M. Sorel, and A. Melloni, "Coherent backscattering in optical microring resonators," *Appl. Phys. Lett.* **96**(8), 081112 (2010).
28. G. C. Ballesteros, J. Matres, J. Martí, and C. J. Oton, "Characterizing and modeling backscattering in silicon microring resonators," *Opt. Express* **19**(25), 24980–24985 (2011).
29. M. S. Dahlem, C. W. Holzwarth, A. Khilo, F. X. Kärtner, H. I. Smith, and E. P. Ippen, "Reconfigurable multi-channel second-order silicon microring-resonator filterbanks for on-chip WDM systems," *Opt. Express* **19**(1), 306–316 (2011).

1. Introduction

Silicon-on-insulator (SOI) is an attractive platform for achieving very large scale integration of photonic integrated circuits (PICs) [1]. This is due to silicon's high index of refraction, relatively low loss at telecommunication wavelengths, and compatibility with the CMOS fabrication processes. Various photonic devices based on SOI technology have been demonstrated for applications in filtering [2], modulation [3], and sensing [4,5].

The high refractive index of silicon enables strong optical mode confinement to be achieved in the SOI waveguides. This permits device structures with small bending radii to be fabricated which allows extreme miniaturization. However, the small sizes of the waveguides combined with strong modal confinement make them very sensitive to variations in the refractive index and waveguide dimensions caused by fabrication imperfections. For example, a deviation of only 1nm in a typical silicon waveguide's height or width will affect a change of ~ 0.002 in the waveguide's effective index. This deviation from designed values can significantly alter the response of phase-sensitive photonic components. For an SOI microring resonator, an index change of 0.002 will lead to over 100 GHz shift in the resonance, which is unacceptable for most PIC applications.

Although SOI fabrication technology has advanced significantly, it is still not possible to control etched dimension variations and silicon film thickness uniformity to better than a 1nm accuracy across an entire wafer [6,7]. It is therefore necessary for most applications to employ a post-fabrication trimming technique to correct for fabrication-induced variations in silicon PICs and restore their proper device functionalities. The most common approach is to modify the effective index of a silicon waveguide by means of the thermo-optic effect. This is

accomplished by placing resistive micro-heaters above silicon waveguides and controlling the power flow through each heater to selectively change the waveguides' temperatures [8,9]. While this technique is very effective, it has the disadvantages of causing thermal cross-talk and requiring a continuous power supply to the heaters in addition to the extra processing steps required to fabricate them. The development of a permanent technique for tuning silicon PICs is actively being pursued to circumvent these issues.

Many permanent techniques for trimming silicon photonic devices have been demonstrated. Silicon microring resonators have been tuned by UV [10] or visible light [11] trimming of the cladding layer. Electron beam compaction of the oxide layer [12] or electron beam bleaching of a polymer cladding layer [13] have also been shown to be effective for tuning silicon microrings. Local oxidation of silicon has been used to trim photonic crystals using a laser-assisted process [14] and microring resonators using an atomic force microscope tip [15]. There have also been trimming methods demonstrated in other material platforms that could be applied to silicon devices [16–18]. Most of these techniques, however, have disadvantages in that they are slow, require complex setups, or can provide only a limited tuning range.

We have recently demonstrated a new permanent technique for trimming silicon devices based on surface modification of silicon waveguides by an out-of-plane femtosecond laser pulse [19]. Depending on the fluence, the laser shot can modify the silicon waveguide by converting some of the crystalline silicon near the waveguide surface to amorphous silicon or by nanomilling the top of the waveguide by ablation. This technique was shown to enable permanent bi-directional tuning of a microring resonator over a wide range. The method is also fast and the setup is relatively simple and readily adaptable to wafer-scale application.

In this work we demonstrate the ability of the technique to fine tune high quality (Q) factor microring resonators. The sharp resonances of the high Q microring notch filters allowed us to accurately monitor small changes in the effective index of the silicon waveguides along with any induced loss. We observed an approximately linear tuning rate in the amorphization regime with a minimum resonance wavelength shift of 0.10nm. We also demonstrated the application of the method to permanently correct the resonance mismatch of a second-order microring filter.

2. Fabrication and measurement of silicon microring resonators

Seven all-pass silicon microring resonators were fabricated on an SOI chip consisting of a 340nm crystalline Si (c-Si) on a 1 μ m-thick SiO₂ buffer. Each microring had a 15 μ m radius and was coupled to a single bus waveguide via a coupling gap of 410nm. Both the bus and microring waveguides had a nominal width of 310nm. The devices were patterned using a Raith 150-TWO electron beam lithography system with ZEP520A resist, followed by dry etching. The devices were left air cladded. An SEM image of one of the fabricated microring resonators is shown in Fig. 1(a). The chip was cleaved to expose the bus waveguide facets for measurement, leaving a total waveguide length of about 3mm. Light in the 1500-1600nm wavelength range from a continuous-wave tunable laser was adjusted to the TM polarization and butt coupled on chip using a lensed fiber aligned to the waveguide facets. The transmitted light was then collected by another lensed fiber for detection. Figure 1(b) shows a typical spectral response of the fabricated microring resonators.

To extract the device parameters, we performed curve fitting of the measured data with the theoretical response of an all-pass microring resonator. We also accounted for the effects of reflections from the waveguide facets by modeling the device as microring resonator embedded inside a Fabry-Perot cavity. The transfer function of the system is given by

$$H_{Chip} = \frac{(1-r)H_{MR}e^{-j\phi_1}}{1-rH_{MR}^2e^{-2j\phi_1}}, \quad (1)$$

where r is the reflectance of a single waveguide end facet, ϕ_l is the phase change over the length of the bus waveguide, and H_{MR} is the transfer function of the all-pass microring given by

$$H_{MR} = \frac{\tau - a_r e^{-j\phi_r}}{1 - \tau a_r e^{-j\phi_r}}. \quad (2)$$

In the above equation τ is the transmission coefficient of the bus-to-ring coupling junction, ϕ_r is the microring roundtrip phase and a_r is the roundtrip field attenuation factor. The inset of Fig. 1(b) shows a typical curve fit of one of the microring resonances. Normally the round-trip attenuation coefficient, a_r , and the transmission coefficient, τ , of an all-pass microring cannot be independently determined from its spectral response. However, since our microring is embedded in a Fabry-Perot cavity we are able to indirectly obtain phase information from the response of the ring and therefore separately determine the roundtrip attenuation and transmission coefficient when fitting the response with Eq. (1). The average values for the transmission coefficient, τ , and roundtrip field attenuation factor, a_r , were 0.972 and 0.986, respectively, giving an average loaded quality factor of 25,000 and intrinsic quality factor of 75,000 for the microrings.

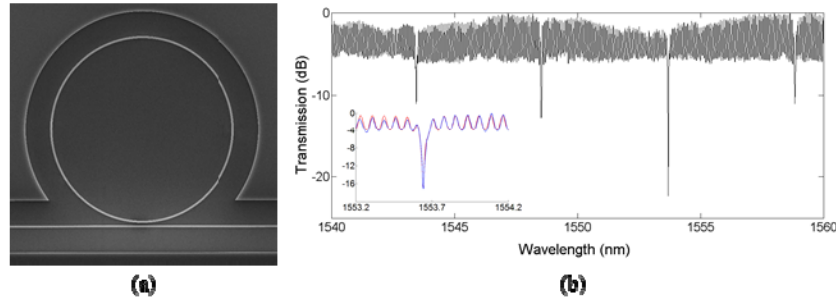


Fig. 1. (a) Scanning electron microscope image of a 15 μm radius all-pass microring resonator. (b) Initial TM spectral scan of one of the microrings used in the study. Inset: blue is the measured transmission of one resonance and red is the curve fit.

3. Femtosecond laser tuning setup and results

Single femtosecond laser pulses at 400nm were used in this study to modify the silicon waveguides of the microrings. The 400nm pulses were frequency doubled in a BBO nonlinear crystal from ~ 130 fs FWHM pulses at 800nm produced by a Ti:sapphire laser. A 1mm thick BG39 filter was then placed in the beam path to remove the remaining 800nm light. As in our previous study [19], we chose to use a “top hat” beam profile to ensure a constant fluence across the waveguides. A “top hat” beam of 8.8 μm radius was obtained by demagnified imaging of the center part of a Gaussian beam (8 mm beam waist diameter) selected with a pinhole aperture (500 μm diameter) over which the intensity distribution was nearly uniform. The experimental setup is shown in Fig. 2(a), and the spatial profile of the “top hat” beam is in Fig. 2(b). While a reasonably flat profile was achieved, some residual intensity modulation on the order of 10 to 20% was observed at the edge of the spot due to diffraction. This intensity modulation increased if the device was placed in front of the best image plane or after it as seen in Fig. 2(c). The radius of the beam was about half that of the microrings, which allowed each microring to be shot twice on fresh sections of its waveguide.

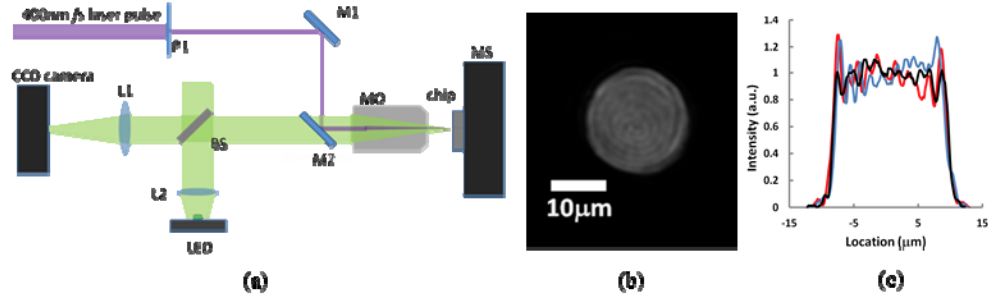


Fig. 2. (a) Setup of the fs laser tuning experiment. The center of a Gaussian pulse of 8mm beam waist diameter passed through a pin hole of 500µm diameter (P1), and was imaged onto the device. M1 and M2 are 400nm dielectric mirrors, L1 and L2 are plano-convex lenses, MO is a 10X microscope objective of 0.28 numerical aperture, MS is a 3D motion stage, BS is a beam splitter. (b) Femtosecond laser “top hat” beam profile when the device was at the best image plane. (c) The horizontal line-out across the center of the beam when the device was at the best image plane (black line), and 2 µm in front (blue) or after (red) it.

Six microrings were used for the femtosecond laser tuning experiments while one was left unmodified as a control. After the initial characterization of the devices, each microring was shot with the laser once at varying fluences. The microrings were measured and characterized again, and then shot once more at different fluences on an unmodified section of the ring waveguide. Figure 3(a) shows a plot of the resonance wavelength shift as a function of the average laser fluence. The horizontal error bars are due to uncertainty in the energy calibration and the exact size of our laser spot. The vertical error bars are mainly due to our approximately $\pm 2\mu\text{m}$ accuracy of aiming the center of the laser spot onto the waveguide, resulting in some uncertainty in the length of ring waveguide affected by the shot. Figure 3(b) shows the change in the effective index of the section of waveguide amorphized by the laser shot. The effective index change was computed from the resonance wavelength shift by

$$\Delta n_{\text{eff}} = \frac{\Delta\lambda}{\lambda_o} \cdot \frac{2\pi R}{l} \cdot n_{\text{eff},o} \quad (3)$$

where λ_o is the original resonance wavelength of the microring, $\Delta\lambda$ is the resonance wavelength shift, R is the microring radius, l is the length of the modified section of ring waveguide, and $n_{\text{eff},o}$ is the original effective index of the waveguide. For our SOI waveguides the effective index of the TM mode was determined to be 2.3 using a Finite Difference mode solver.

Figure 3(a) shows that by changing the fluence of the laser shot it is possible to control the direction and extent of the wavelength shift. The positive shifts in the resonance wavelength at fluences below 0.2 J/cm^2 are due to amorphization of a small amount of the crystalline silicon at the waveguide surface. This layer of amorphous silicon has a higher index of refraction than the original crystalline silicon, leading to an increase in the effective index of the waveguide. The negative shifts in the resonance wavelength at fluences above 0.2 J/cm^2 are due to ablation of a small amount of material off the top of the waveguide. This causes a decrease in the waveguide height which results in a decrease in the effective index of the waveguide. The $\sim 0.2 \text{ J/cm}^2$ threshold for laser ablation of silicon at the 400nm wavelength is consistent with our previous work [19]. In the ablation regime, the minimum negative shift in the resonance wavelength was -1.7nm , corresponding to a change in the waveguide effective index of -0.013 . It was observed in our previous experiments that ablation only a few hundredths of a J/cm^2 above the ablation threshold could be damaging to the waveguide resulting in significantly increased loss so laser shots at higher fluences were not attempted.

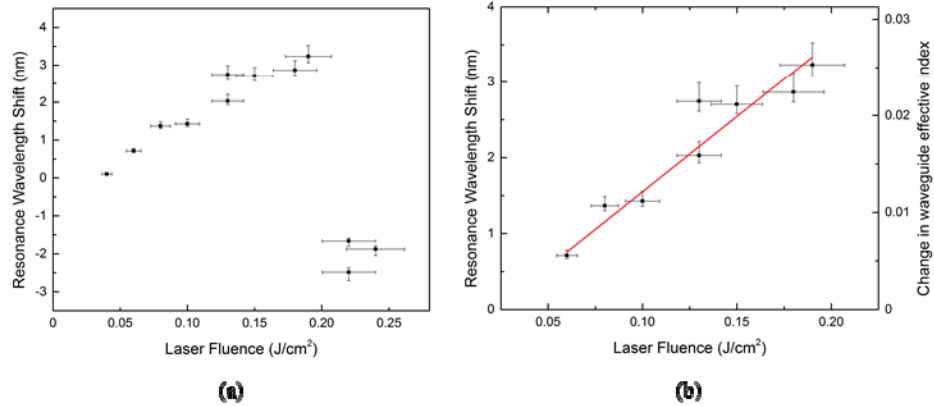


Fig. 3. (a) Resonance wavelength shift of the microring resonators as a function of laser fluence. (b) Linear fit of the positive resonance shifts and change in the waveguide effective index as function of the laser fluence. The data point at 0.04 J/cm² is removed for reasons discussed in the text.

In our previous work [19], we determined the amorphization threshold to be 0.06 J/cm² whereas here we observed amorphization at an average fluence of 0.04 J/cm². This discrepancy is due to small fluctuations in the beam profile which caused the local intensity to be well above 0.04 J/cm² leading to amorphization in some small regions near the edge of the beam spot. As seen in Fig. 2(c), the intensity fluctuations were even more pronounced if the device was not placed in the proper image plane. This effect was also observed visually through a change in colour for only small regions within the spot size, as seen through an optical microscope.

In the amorphization regime (laser fluence below 0.20 J/cm² and above 0.06 J/cm²) there appears to be a linear correlation between the resonance wavelength shift and the laser fluence. The data point at 0.04 J/cm² was not included in Fig. 3(b) because only a small portion of the laser spot caused amorphization and the length of waveguide changed is therefore unknown. Assuming a linear relationship in Fig. 3(b) we obtain a tuning rate of 20 ± 2 nm/J·cm⁻² (or $\Delta n_{\text{eff}} = 0.16 \pm 0.02$ per J/cm² for the length of waveguide shot) above the amorphization threshold of 0.06 J/cm².

There are three possible explanations for the linear correlation between the wavelength shift and laser fluence in the amorphization regime. The first hypothesis is that as the fluence increases, the depth of the amorphized silicon layer also increases. It is reasonable to assume that a higher laser fluence will cause a larger volume of crystalline silicon near the surface to melt, resulting in a thicker layer of amorphous silicon (the waveguide width being fixed). This hypothesis is supported by J. Bonse [20], who optically characterized the depth of amorphous silicon from an 800nm, femtosecond Gaussian laser pulse. Assuming that the refractive index of amorphous silicon does not depend on the laser fluence, it was concluded that this depth was likely dependent on the laser fluence used. The second possibility is that the volume of the amorphous silicon stays constant with changing laser fluences, but the index of refraction of the amorphous silicon is modified instead. This hypothesis is supported by the work of Izawa et. al [21,22], where it was shown using transmission electron microscopy (TEM) that the depth of the amorphous silicon produced using 400, 800, and 1550nm laser pulses did not vary with the number of shots or laser fluence below the ablation threshold (ref [21], reports the depth of amorphous silicon to be 17nm when irradiating crystalline silicon with a single 400nm femtosecond laser pulse). However, in a later publication, Izawa et al [23] also showed that for 266nm laser pulses the depth of amorphous silicon produced does vary over a Gaussian spot size. Although it is noted in many publications that the index of amorphous silicon is highly dependent on the manner in which

it is produced [24,25], to our knowledge and also noted in ref [20], there has been no study of the change in the refractive index of amorphous silicon produced by femtosecond laser shots of various fluences. Thus further studies are needed to confirm the second hypothesis. The third option is a combination of increased amorphization depth along with increased index of refraction at higher laser fluences, which is the most probable explanation given the evidence in the literature.

For this experiment, when the entire spot size was above the amorphization threshold, we achieved a minimum positive resonance wavelength shift of 0.71nm using a fluence of 0.06 J/cm². This corresponds to a minimum change of 5.6×10^{-3} in the waveguide effective index. However, the data point at 0.04 J/cm² shows the current tuning resolution of the technique. Due to the shorter affected length of waveguide, a shift in the resonance of 0.10nm was observed for this shot, which is roughly $1.5 \times$ the bandwidth of these microrings. This shift cannot be converted to a change in the effective index because the length of waveguide affected is uncertain, but it illustrates that the shift is dependent on length of the waveguide affected. The resolution of the technique will be dependent on the ratio of the length of waveguide affected to the circumference of the microring, which is evident from Eq. (3). Therefore, the technique's resolution can be made very fine by using either a large microring and/or a very small spot size. The tuning rate obtained in Fig. 3(b) can be modified in the same manner as the tuning resolution. The spot size of the laser pulse, along with the accuracy of the alignment stage, is the limiting factor for fine tuning with this technique.

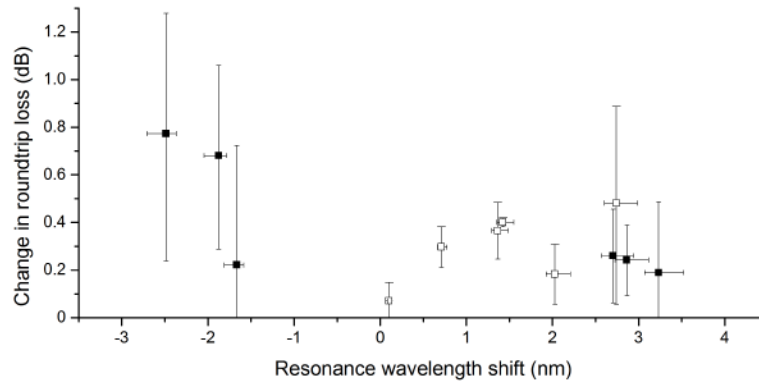


Fig. 4. Change in roundtrip loss of the microrings following shots plotted as a function of the resonance wavelength shift. Negative shifts represent ablation and positive shifts represent amorphization of the waveguide. The open and closed data points represent the first and second shots on the microrings respectively.

Measurements of the roundtrip loss in the microring resonators also allowed us to investigate the effect of the laser shots on the waveguide loss. The initial roundtrip loss of the microring resonators averaged over four resonance peaks between 1540 and 1560nm was found to be 0.25 ± 0.05 dB. The large variation in the roundtrip loss is most likely due to coherent backscattering from the sidewall roughness of the microring waveguides [26,27], an effect which has been reported for silicon microrings very similar to ours [28]. In Fig. 4 the change in the average roundtrip loss is plotted versus resonance wavelength shift induced by each shot. The error bars represent the standard deviation of the initial roundtrip loss measured for four resonance peaks between 1540 and 1560nm that is then added in quadrature with the same value for the final roundtrip loss. In the amorphization regime (positive resonance shifts), it is observed that the roundtrip loss increased with every laser shot, which is expected since amorphous silicon has larger absorption than crystalline silicon [25]. However, there appears to be no definite correlation between the loss and the laser fluence and the error bars are fairly large and vary significantly in magnitude. The large error bars cross below zero for some data points, but no single measurement indicated a decrease in

loss. The lack of a definite trend combined with the large fluctuations in the loss data suggests a dominant contribution from amplification of the coherent backscattering effect that was already present in the silicon waveguides before the laser shots. When a laser shot amorphizes some of the silicon, it may roughen the top surface of the waveguide and/or produce volumetric index inhomogeneities due to mixtures of amorphous and crystalline Si. This roughness could increase the backscattering and cause large fluctuations in the measured roundtrip loss at different resonances as observed. The effect could also be amplified for the TM polarization since it is more sensitive to roughness on the top surface of the waveguide than on the sidewalls. This hypothesis is supported by the much larger increase in loss and the larger fluctuations in its measurement for shots above the ablation threshold (negative shifts in the resonance wavelength in Fig. 4) together with evidence from AFM scans of unpatterned silicon surfaces after ablation showed an increased surface roughness [19].

In order to quantify the loss induced by femtosecond laser surface modification, microrings where coherent backscattering is insignificant should be investigated or a separate measurement of the backscattering is required in another study. The backscattering may also be reduced by using a smoother beam profile than the one shown in Fig. 2(b) or one with a more gradual change in fluence profile, such as a Gaussian laser spot. A further reduction in backscattering may also be possible by annealing the sample at high temperature [25].

4. Application of the laser tuning method to a second-order microring filter

One potential application of the technique is in correcting fabrication-induced resonance misalignment in high-order silicon microring filters. These devices consist of multiple coupled microring resonators whose resonances have to be accurately controlled for the proper operation of the device [29].

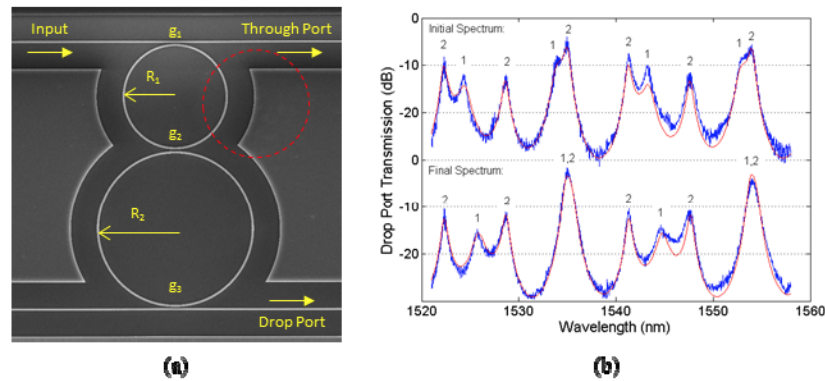


Fig. 5. (a) SEM of the second-order microring filter. All of the device parameters are labeled in yellow and the location of the single femtosecond laser shot is outlined in red. (b) Spectral response before and after tuning by a femtosecond laser shot. The blue curves are the measured spectra and the red curves are the best fits, with the peaks corresponding to ring 1 and 2 labeled.

To demonstrate the ability of the femtosecond laser tuning technique to permanently correct the resonance mismatch in this type of device, we designed and fabricated a second-order microring filter consisting of two non-identical microring resonators with unmatched resonances. An SEM image of the device is shown in Fig. 5(a). The two microrings have radii $R_1 = 8\mu\text{m}$ and $R_2 = 12\mu\text{m}$, giving individual free spectral range (FSR) of 9.5nm and 6.33nm, respectively. When two resonances of the microrings are aligned, the FSR of the device will increase to 19nm due to the Vernier effect with suppressed resonance peaks in between. The field coupling coefficients between the bus waveguides and the microrings (κ_1 , κ_3) and between the two microrings (κ_2) were designed to give a flat-top filter response. For a 100GHz-bandwidth filter the coupling values were determined to be $\kappa_1 = \kappa_3 = 0.60$, $\kappa_2 = 0.18$,

and the corresponding coupling gaps were $g_1 = 170$ nm, $g_2 = 300$ nm, $g_3 = 200$ nm. (The coupling gap between ring 1 and the input bus waveguide is smaller than between ring 2 and the output bus waveguide because ring 1 has a smaller radius and hence shorter interaction length with the bus).

The top trace in Fig. 5(b) shows the as-fabricated spectral response of the device with the resonance peaks of each microring labelled. The 1535nm transmission peak is split due to a ~ 1.1 nm detuning between the resonances of the two microrings. To align the two resonances, we increased the resonance wavelength of microring 1 by applying a single laser shot at 0.06 J/cm² to a section of the ring as indicated in Fig. 5(a). The device spectral response after the laser shot is shown by the bottom trace in Fig. 5(b). The two microring resonances at the 1535nm wavelength are seen to merge to form a second-order filter response with a bandwidth of 112GHz and an insertion loss of ~ 3 dB. Careful modeling of the spectral response (shown by the red curve and obtained by least squares fitting) revealed that microring 1's resonance wavelength was now greater than microring 2's resonance wavelength by ~ 0.3 nm, indicating that the resonances of microring 1 were moved by a total of 1.4nm by the laser shot. Note that at the same fluence of 0.06 J/cm², the resonance shift in the $8\mu\text{m}$ -radius ring is larger than the value recorded for the $15\mu\text{m}$ microring in Fig. 3. This is because a larger fraction of the microring roundtrip length was modified by the laser shot in the smaller ring. We also observed that the adjacent resonance peaks were much more suppressed below the main filter transmission peaks than in the original as-fabricated spectrum. The roundtrip loss for microring 1 before and after the femtosecond laser shot changed only slightly according to our modelling, increasing from 0.77dB to 0.86dB, while all other fitting parameters remained the same except for the resonance wavelength of microring 1. Our model showed that this increase in the loss of ring 1 accounts for only a 0.15dB change in the insertion loss of the device.

5. Conclusion

We have shown that femtosecond laser surface modification of silicon waveguides is a promising technique for tuning silicon microring resonators and other phase sensitive devices. In the amorphization regime, we observed an approximately linear relationship between the effective index change in the silicon waveguide and the fluence of the laser shot. The physical mechanism for this relationship is either an increase in the depth of amorphous silicon and/or an increase in the index of refraction of the amorphous silicon produced by the laser shots [20–25]. The propagation loss in the silicon waveguides, induced by either the conversion of some crystalline silicon to amorphous silicon or ablation of material, increased for all shots as expected, but no definite correlation to the laser fluence was observed due to effects from coherent backscattering in the microrings [26,27]. It may be possible to reduce the coherent backscattering effects by using a smoother beam profile or by annealing the device at a high temperature in future studies.

The minimum resonance wavelength shifts achieved in the experiment were 0.10nm and -1.7 nm for amorphization and ablation respectively. These shifts can be made lower by moving the beam center off the waveguide or using a smaller spot size so that a smaller section of the ring is irradiated. We also demonstrated an application of the technique in tuning a second order microring filter. The resonance mismatch of two silicon microrings was corrected by a single femtosecond laser shot, proving that this technique can be a fast and reliable method of trimming high-order filters and other advanced PICs on a silicon platform.

Acknowledgments

This research was supported by the Natural Sciences and Engineering Research Council of Canada (NSERC) and Alberta Innovates. The authors would also like to thank Ashok M. Prabhu for assisting in the fabrication of the devices.